Compressive Sampling as an Enabling Solution for Energy-Efficient and Rapid Wideband RF Spectrum Sensing in Emerging Cognitive Radio Systems

Rabia Tugce Yazicigil

Submitted in partial fulfillment of the
requirements for the degree of
Doctor of Philosophy
in the Graduate School of Arts and Sciences

COLUMBIA UNIVERSITY

2016

Abstract

Compressive Sampling as an Enabling Solution for Energy-Efficient and Rapid Wideband RF Spectrum Sensing in Emerging Cognitive Radio Systems

Rabia Tugce Yazicigil

Wireless systems have become an essential part of every sector of the national and global economy. In addition to existing commercial systems including GPS, mobile cellular, and WiFi communications, emerging systems like video over wireless, the Internet of Things, and machine-to-machine communications are expected to increase mobile wireless data traffic by several orders of magnitude over the coming decades, while natural resources like energy and radio spectrum remain scarce. The projected growth of the number of connected nodes into the trillions in the near term and increasing user demand for instantaneous, over-the-air access to large volumes of content will require a 1000-fold increase in network wireless data capacity by 2020. Spectrum is the lifeblood of these future wireless networks and the 'data storm' driven by emerging technologies will lead to a pressing 'artificial' spectrum scarcity.

Cognitive radio is a paradigm proposed to overcome the existing challenge of underutilized spectrum. Emerging cognitive radio systems employing multi-tiered, shared-spectrum access are

expected to deliver superior spectrum efficiency over existing scheduled-access systems; they have several device categories (3 or more tiers) with different access privileges. We focus on lower tiered 'smart' devices that evaluate the spectrum dynamically and opportunistically use the underutilized spectrum. These 'smart' devices require spectrum sensing for incumbent detection and interferer avoidance. Incumbent detection will rely on database lookup or narrowband high-sensitivity sensing. Integrated interferer detectors, on the other hand, need to be fast, wideband, and energy efficient, while requiring only moderate sensitivity.

These future 'smart' devices operating in small cell environments will need to rapidly (in 10s of μs) detect a few (e.g. 3 to 6) strong interferers within roughly a 1GHz span and accordingly reconfigure their hardware resources or request adjustments to their wireless connection consisting of primary and secondary links in licensed and unlicensed spectrum.

Compressive sampling (CS), an evolutionary sensing/sampling paradigm that changes the perception of sampling, has been extensively used for image reconstruction. It has been shown that a single pixel camera that exploits CS has the ability to obtain an image with a single detection element, while measuring the image fewer times than the number of pixels with the prior assumption of sparsity. We exploited CS in the presented works to take a 'snapshot' of the spectrum with low energy consumption and high frequency resolutions.

Compressive sampling is applied to break the fixed trade-off between scan time, resolution bandwidth, hardware complexity, and energy consumption. This contrasts with traditional spectrum scanning solutions, which have constant energy consumption in all architectures to first order and a fixed trade-off between scan time and resolution bandwidth. Compressive sampling enables

energy-efficient, rapid, and wideband spectrum sensing with high frequency resolutions at the expense of degraded instantaneous dynamic range due to the noise folding.

We have developed a quadrature analog-to-information converter (QAIC), a novel CS rapid spectrum sensing technique for band-pass signals. Our first wideband, energy-efficient, and rapid interferer detector end-to-end system with a QAIC senses a wideband 1GHz span with a 20MHz resolution bandwidth and successfully detects up to 3 interferers in 4.4μs. The QAIC offers 50x faster scan time compared to traditional sweeping spectrum scanners and 6.3x the compressed aggregate sampling rate of traditional concurrent Nyquist-rate approaches. The QAIC is estimated to be two orders of magnitude more energy efficient than traditional spectrum scanners/sensors and one order of magnitude more energy efficient than existing low-pass CS spectrum sensors.

We implemented a CS time-segmented quadrature analog-to-information converter (TS-QAIC) that extends the physical hardware through time segmentation (e.g. 8 physical I/Q branches to 16 I/Q through time segmentation) and employs adaptive thresholding to react to the signal conditions without additional silicon cost and complexity. The TS-QAIC rapidly detects up to 6 interferers in the PCAST spectrum between 2.7 and 3.7GHz with a 10.4μs sensing time for a 20MHz RBW with only 8 physical I/Q branches while consuming 81.2mW from a 1.2V supply.

The presented rapid sensing approaches enable system scaling in multiple dimensions such as ADC bits, the number of samples, and the number of branches to meet user performance goals (e.g. the number of detectable interferers, energy consumption, sensitivity and scan time).

We envision that compressive sampling opens promising avenues towards energy-efficient and

rapid sensing architectures for future cognitive radio systems utilizing multi-tiered, shared spectrum access.

Contents

List of Figures

List of Tables

Acknowledgments

Firstly, I would like to thank my thesis advisor Professor Peter R. Kinget for his continual guidance, support and patience. He has advised me to aim high and work hard for my goals. As I think about the range of things on his plate, I find it so inspiring to see how he always finds the time for meetings with his students. It is also so very inspiring to see his excitement for new ideas, and research in such a wide range of topics. I hope that I also learned some of his excellent advising, presentation and writing skills for my future career. It has been a great fortune of mine to have gotten this opportunity to be his student.

I would like to thank my thesis co-advisor Professor John Wright for his guidance and support throughout this interdisciplinary research project. He has taught me how to approach the problems in my plate from different angles.

I thank the other members of my thesis committee – Professor Harish Krishnaswamy, Professor Azita Emami, and Dr. Abhishek Bandyopadhyay for their valuable time, comments and suggestions.

It has been a privilege to work with Tanbir Haque and I would like to thank him for his collaboration on our research project and the many useful discussions for many years. I would like to thank Michael Whalen, Jeffrey Yuan, Manoj Kumar, Chris Kunkel, Jiawen Zhang, Han-Wen Kuo, and Qing Qu for their contributions to this research project and it was a great experience to work with you all on this interdisciplinary research project.

I would like to thank, in no particular order, the past CISL members: Jayanth Kuppambatti, Baradwaj Vigraham, Chun-Wei Hsu and Karthik Tripurari since they were the best mentors I could

have asked for during the first few years at Columbia University. I would also like to thank, in no particular order, the current CISL members: Jianxun Zhu, Yang Xu, Shravan Siddart Nagam, Sarthak Kalani, Daniel De Godoy Peixoto, Yu Chen, Sharvil Patil, and Ning Guo for many useful discussions and being excellent colleagues. My internship at Intel was a great learning experience and I would like to thank Richard Lin for great discussions.

The work presented in this thesis was supported by grants from the National Science Foundation (NSF) and by STMicroelectronics for chip fabrication donation in advanced CMOS processes. I also would like to thank in particular John Kazana and the Columbia University Electrical Engineering department for their equipment support during this research project. I owe a great deal of gratitude to Elsa Sanchez, Janice Savage, Zachary Collins, Arturo Lopez, Yoel Rio, Laura Castillo and Jessica Rodriguez of the Electrical Engineering department for their administrative support over the course of my doctoral studies.

Outside of work, I have been very lucky to have a great friend circle. A special mention goes out to the my friends who have been a 'family' for me during the last couple years in NYC, in particular, Burak, Eymen, Nilufer, Filiz and Cagan, Hande, Anil, Charishma, Rachel, Esha, David and Jaebin. To Andrew Kirby, thank you for your support, your encouragement and also making the last couple years of my life a great adventure.

This thesis is dedicated to my family, especially my parents Emine Cantekinler and Abdullah Cikrikci, for their endless belief in me. They have been a constant source of support not only during my graduate studies at Columbia University, but throughout my entire life. This work would not have been possible without you.

Chapter 1

Introduction

1.1 Motivation

Wireless systems have become an essential part of every sector of the national and global economy. Mobile wireless data traffic is predicted to grow by several orders of magnitude over the coming decades, driven by applications like video over wireless, the Internet of Things, and machine-to-machine communications, while resources like energy and radio spectrum remain scarce. Due to the nature of EM wave propagation, the available bandwidth at different carrier frequencies, and the practical size of antennas, spectrum ranging from roughly 500MHz to 6GHz is of particular importance for mobile wireless communications. As such, the electromagnetic spectrum is a finite natural resource. If the consumer demand for instantaneous, over-the-air access to large volumes of content continues to grow at its current rate in the US, a 500MHz to 1GHz spectrum deficit is projected in the near to medium term. Responding to this 'artificial' spectrum shortfall, the US

President's Council of Advisors on Science and Technology (PCAST) released a report in 2012 that recommended sharing of up to 1GHz of federal government radio spectrum, ranging from roughly 2.7GHz to 3.7GHz, with non-governmental entities. Noting the spectrum usage inefficiency of existing scheduled access cellular systems, the council further recommended that future systems deployed in the PCAST bands deliver significantly improved spectrum utilization efficiency.

Cognitive radio is a paradigm proposed to overcome the existing challenge of underutilized spectrum [1]. In today's wireless communications shown in Fig. 1.1(a), particular frequency bands are assigned once-and-forever for fixed uses. Conceptually Fig. 1.1(a) is similar to a highway traffic scenario. While one of the lanes on the highway is overcrowded, other lanes including the lanes assigned to emergency vehicles are underutilized for most of the time. In emerging cognitive radio systems shown in Fig. 1.1(b), the mobile terminals will assess the spectrum usage in their specific location at the given time and dynamically access the available spectrum with the appropriate access technology (i.e. LTE, WiFi, etc.). This sort of dynamic and adaptive sharing of spectrum will significantly alleviate the spectrum scarcity problem, while respecting the rights of the spectrum incumbents. If we think about our conceptual example of the highway traffic scenario, utilizing the free lanes on the highway is equivalent to the operation of cognitive radios that are dynamic, adaptive, and opportunistic.

Future cognitive radio systems employing multi-tiered, shared spectrum access (MTSSA) shown in Fig. 1.2 are expected to deliver superior efficiency over existing scheduled access systems; they have several device categories (3 or more tiers) with different access privileges.

Tier 1 devices include those employed by federal and commercial RADAR, police and emer-

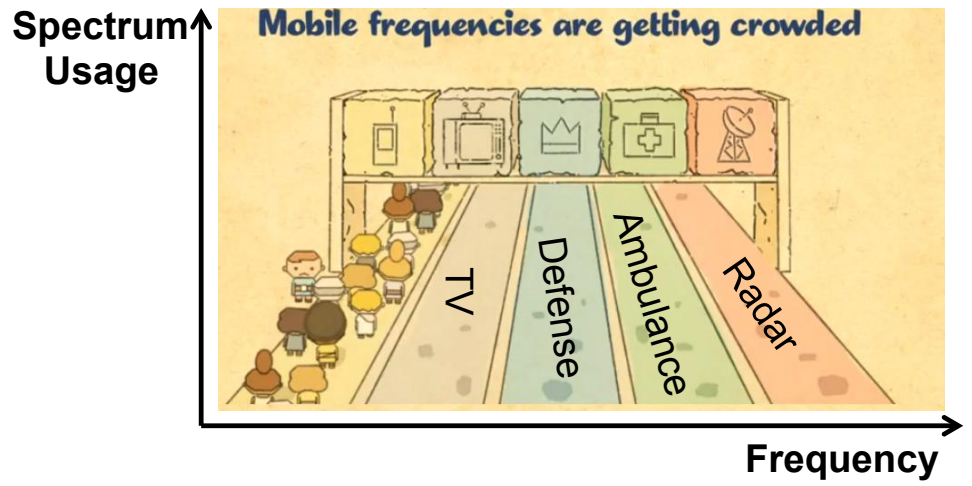

(a)

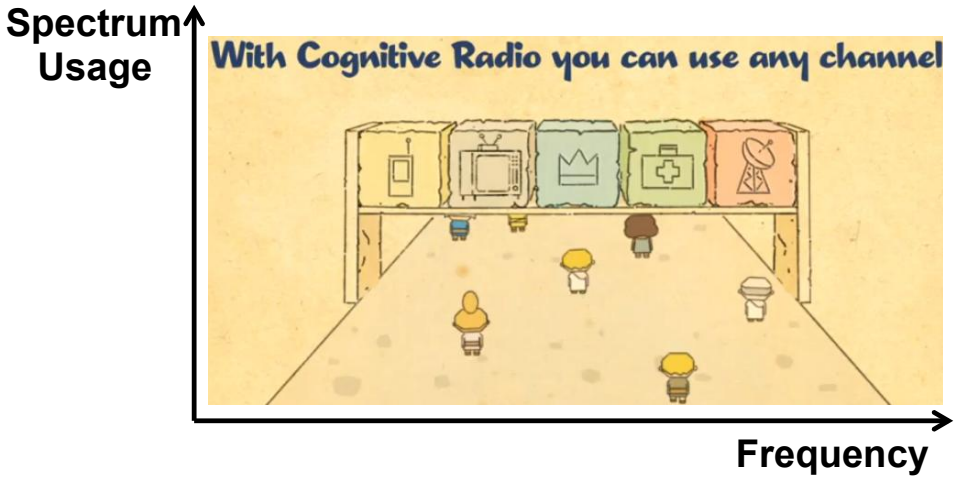

(b)

Figure 1.1: *Conceptual illustration of the spectrum usage in: (a) Today's wireless communications; (b) Next-generation wireless communication systems with cognitive radios [Source: Nokia].*

gency communication as well as classified military communication systems. Tier 1 devices are guaranteed exclusive access to designated channels. The spectrum access rights of Tier 1 devices are enforced by federal policy.

Tier 2 devices include those employed by commercial small cell operators that pay licensing fees to gain access to designated channels for a limited duration in specific geographical vicinities.

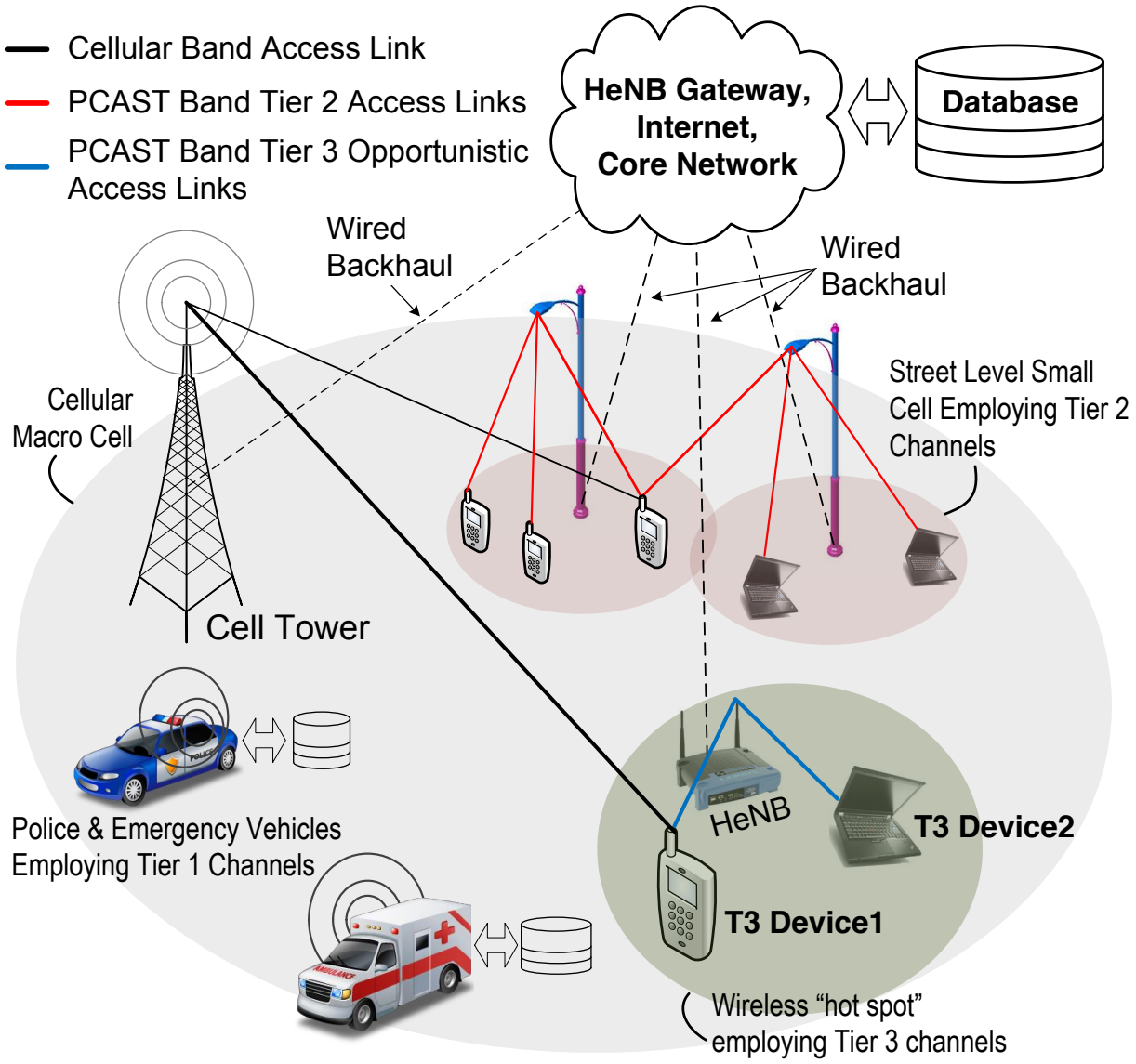

Figure 1.2: *Emerging cognitive radio systems utilizing multi-tiered, shared spectrum access.*

Scheduled access cellular communication schemes like UMTS/LTE are most likely to be employed by Tier 2 systems. Tier 2 systems deployed in the PCAST bands may be used to offload cellular networks deployed in other frequency bands. MTSSA systems are expected to maintain a database that enumerates channels designated for Tier 1 and Tier 2 use only.

Tier 3 'smart' devices are likely to be employed by various emerging commercial systems that opportunistically utilize the remaining spectrum. Tier 3 systems determine the availability of spectrum through database lookup and spectrum sensing. Contention-based spectrum access schemes, like CSMA in WiFi, are thought to be most suitable for Tier 3 systems. Examples of Tier 3 applications include hotspots for home and enterprise, mobile gaming, machine-to-machine communications, etc. The terminal labeled T3 Device 1 in Fig. 1.2 may, for example, take advantage of the 'hotspot' to download a movie (or other large volumes of content) by opportunistically aggregating several available Tier 3 PCAST band channels in its immediate geographical vicinity. This process may be facilitated by the cellular service provider of the Tier 3 device to offload the cellular network.

Emerging cognitive radio (CR) or 5G/next-G technologies like LTE-License Assisted Access (LTE-LAA) and LTE-Unlicensed (LTE-U) will employ under-utilized unlicensed spectrum in addition to designated licensed spectrum. Network operators will have the flexibility to move data traffic to terminals over the licensed and unlicensed spectrum. Knowing the instantaneous interference conditions in the unlicensed bands is key to managing the spectrum allocation of the LTE-LAA/LTE-U terminal and ensuring harmonious coexistence with WiFi and other devices in unlicensed spectrum. Lower-tier 'smart' devices evaluate the spectrum usage dynamically and op-

portunistically employ the underutilized spectrum. However, as in the highway example where the vehicles need to rapidly and frequently check if the lane is free or not before they move over to that lane on the highway, a key challenge for emerging cognitive radio systems is to assess the spectrum usage with a rapid and low-power sensing approach before each data packet transfer. They will require spectrum sensing for incumbent detection and interferer avoidance. Incumbent detection will rely on database lookup or narrowband, high-sensitivity sensing. Integrated interferer detectors, on the other hand, need to be fast, wideband, and energy efficient, while requiring only moderate sensitivity.

In the example shown in Fig. 1.3, the license-anchored LTE-LAA/LTE-U CR terminal periodically senses the spectrum and opportunistically aggregates component carriers in unlicensed spectrum. These future smart devices (e.g. carrier-aggregating receivers) operating in small cell environments will need to rapidly ($t_{sense} \approx$ 10s of μs) detect a few (e.g. 3 to 6) strong interferers within roughly a 1GHz span. The carrier-aggregating receiver can then be accordingly reconfigured on a frame (lasting 10s of ms) basis or can request adjustments to its wireless connection consisting of primary and secondary links in licensed and unlicensed spectrum.

As an example, future spectrum-aware receivers shown in Fig. 1.4 are envisioned to employ one or more tunable notch filters [2] that are digitally assisted by the fast interferer detector to filter out the interferers in a wideband spectrum. With novel circuit techniques in CMOS technology like N-path filters, it is possible to design precise notch filters with high selectivity and tunable center frequency. However, the key challenge is to determine where the interferers are located in a wideband spectrum. Interferer detectors that offer simultaneously fast detection over a wide in-

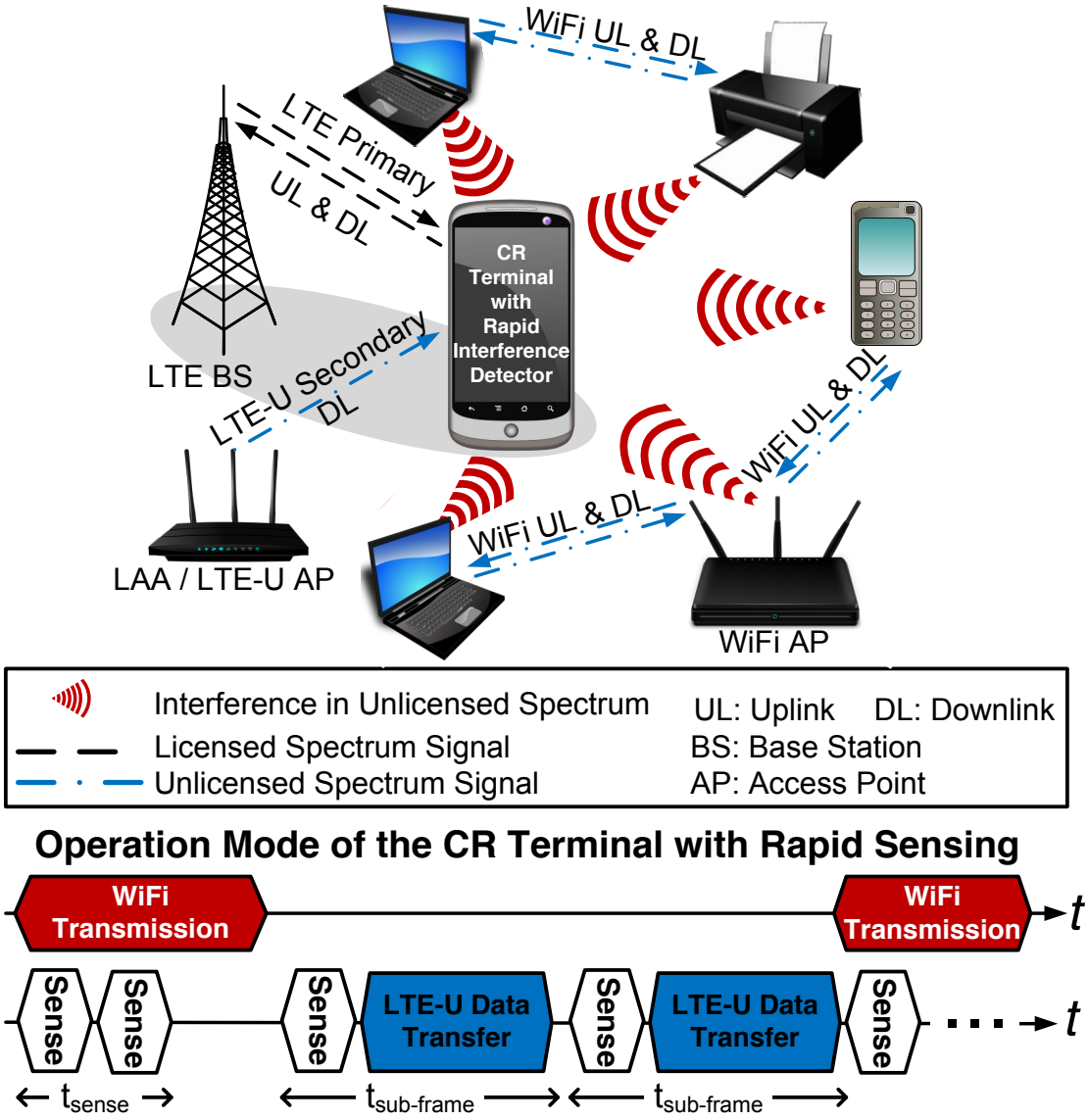

Figure 1.3: *LTE-U deployment scenario example: A cognitive radio terminal with* ***rapid interferer detector*** *that periodically senses the shared spectrum before every data packet transfer and opportunistically aggregates component carriers.*

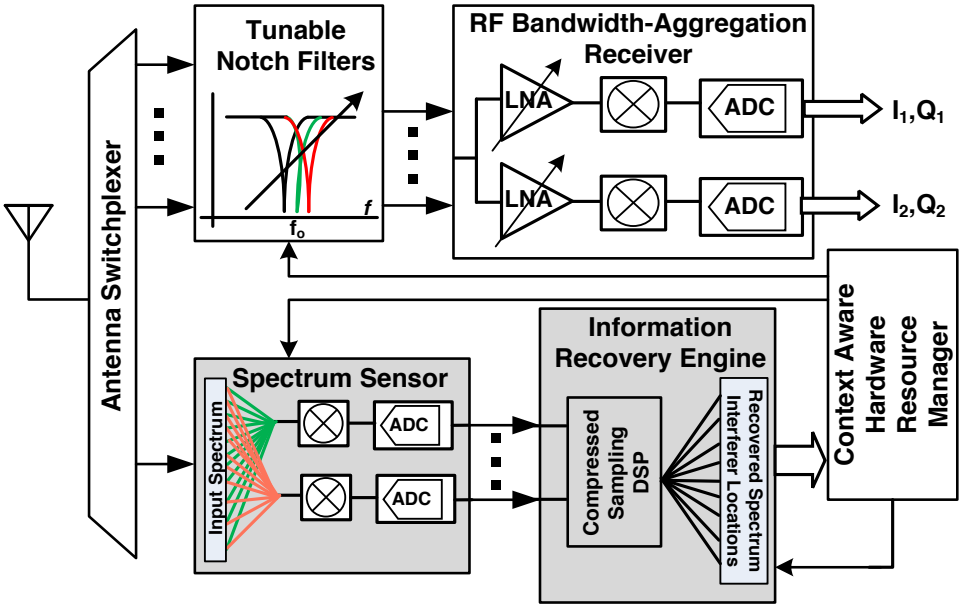

Figure 1.4: *Example of a spectrum-aware receiver using a rapid interferer detector to find the location of interferers so that interferer mitigation resources like tunable notch filters can be deployed.*

stantaneous bandwidth with fine frequency resolutions and low power, while requiring only modest hardware resources, are the key enabling components of future cognitive radio systems.

1.2 Outline

Displayed in Fig. 1.5 is the 'landscape' of spectrum scanners and sensors to show where the band-pass compressed sampling architectures that we have introduced [3–5] fit into this landscape. The key performance metrics of the spectrum scanners and sensors shown in Fig. 1.5 are energy consumption per scan, scan time, instantaneous bandwidth, and instantaneous dynamic range.

Traditional spectrum scanner and sensor architectures and their limitations in terms of the key performance metrics are presented in Chapter 2.

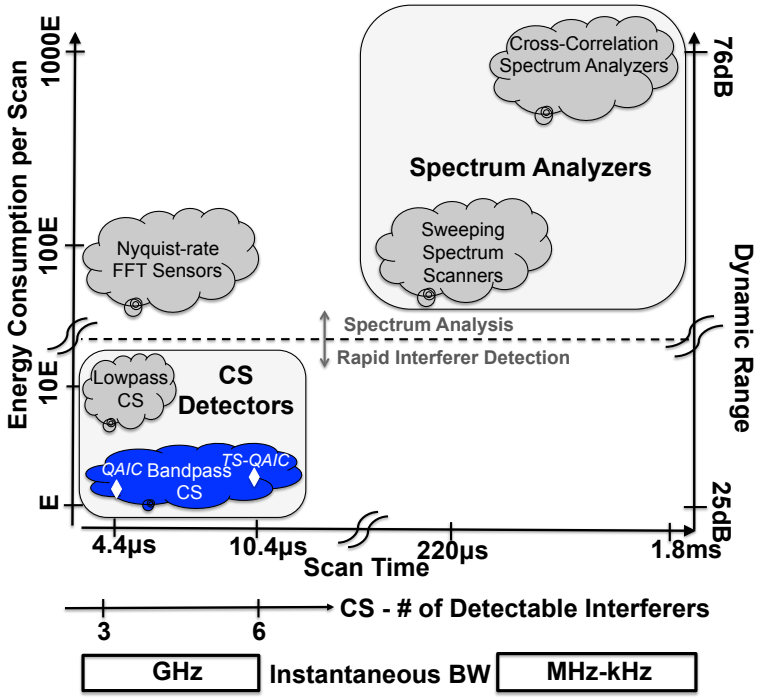

Figure 1.5: *Spectrum scanners and sensors 'landscape'.*

We introduced a new cluster of spectrum sensors that rapidly detect few interferers (e.g. 3 to 6) over a wide instantaneous bandwidth with low power and lower overhead [3, 5]. Compressive sampling (CS) [6, 7] is applied to break the traditional spectrum scanning trade-offs between frequency span, RBW, scan time and energy consumption. Why compressive sampling presents a solution to the spectrum sensing challenge in emerging cognitive radio systems and the challenges associated with implementing CS for RF spectrum sensing are discussed in Chapter 3.

We developed Quadrature Analog-to-Information Converters (QAICs) [3–5] to rapidly sense the spectrum of interest ranging from f_{min} to f_{max} in a band-pass fashion and an energy efficient way compared to existing spectrum scanning and sensing solutions.

The rapid interferer detector using band-pass compressed sampling with a quadrature analog-to-information converter is discussed in Chapter 4. The implementation of the interferer detector

system consisting of a QAIC front end and a CS information recovery engine is presented in Section 4.3. The measurement results of the interferer detector end-to-end system are presented in Section 4.4, followed by a performance summary and discussion in Section 4.6.

We implemented a CS time-segmented quadrature analog-to-information converter [8] that employs adaptive thresholding to react to the signal conditions and extends the physical hardware through time segmentation without additional silicon cost and complexity. The operation of the time-segmented quadrature analog-to-information converter (TS-QAIC) and the advantages offered by the TS-QAIC compared to existing compressed sampling approaches are discussed in Chapter 5. The implementation of the rapid interferer detector with a time-segmented quadrature analog-to-information converter is presented in Section 5.3. The measurement results of the time-segmented rapid interferer detector system are presented in Section 5.4, followed by a performance summary and discussion in Section 5.5.

The challenges and trade-offs associated with the design of compressed sampling architectures are discussed in Chapter 6. The Pseudorandom Noise (PN) mixer, which is the key circuit block of the interferer detector for rapidly capturing the wide instantaneous BW, is analyzed in terms of the design choices and effects of its operation on the instantaneous dynamic range of analog-to-information converters.

In Chapter 7, a summary of the research work on rapid interferer detectors that exploit bandpass compressed sampling is given with a possible direction for extending the topics of study included in this dissertation.

Chapter 2

Traditional Spectrum Scanning or Sensing Architectures

Integrated spectrum scanners, like e.g. [9–12], [13], [14], or [15, 16], rely on traditional spectral analysis which has an intrinsic trade-off between frequency span, RBW, scan time (T_{scan}) and hardware complexity [17].

In a single-branch sweeping spectrum scanner (Fig. 2.1), each frequency bin is scanned sequentially by progressively sweeping the local oscillator (LO) driving the quadrature I/Q down-converter.

The single-branch sweeping spectrum scanner architecture shown in Fig. 2.2 requires widely tunable, high quality RF components that are difficult to implement on a chip. Identifying signals over a 1GHz span with a 20MHz RBW requires a long scan time ($> 220\mu$s as will be demonstrated in Section 4.6) which is proportional to the number of bins N_0. There is a fixed trade-off between the scan time and the RBW. Finer frequency resolution over a wide span results in increased scan time. Therefore, the energy consumption is large and there is a risk of missing fast changing interferers in the spectrum.

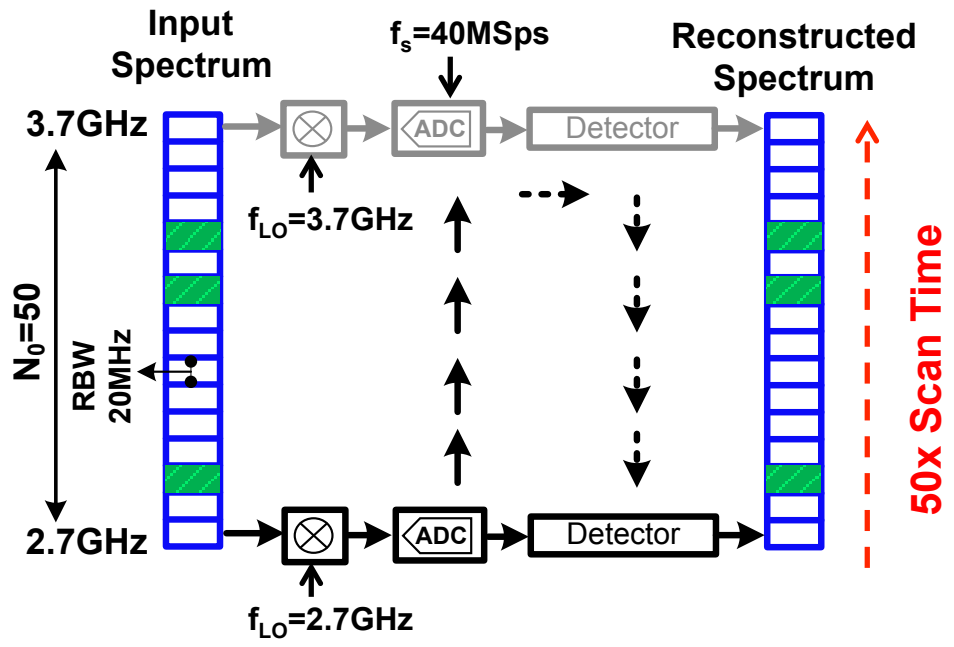

Figure 2.1: *Conceptual illustration of the operation of a traditional sweeping spectral analysis technique applied for a 2.7-3.7GHz spectrum with a 20MHz RBW; the occupied spectrum bins are shaded in green.*

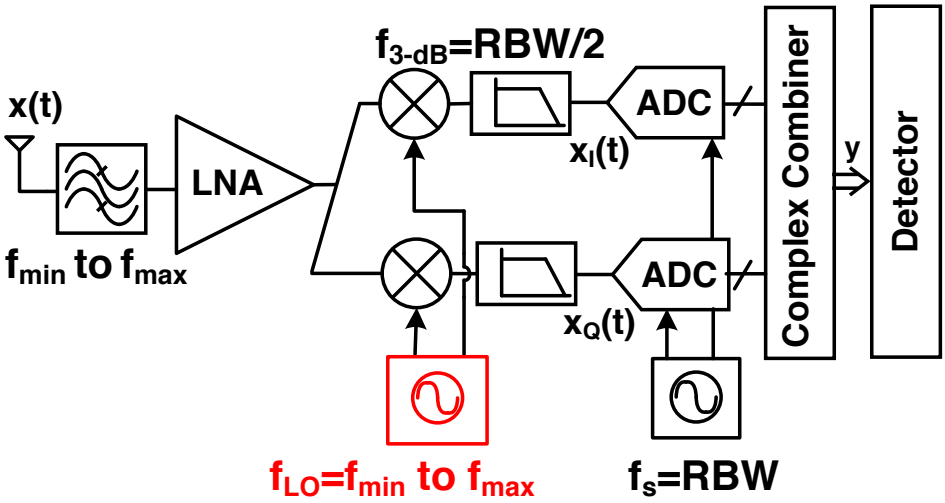

Figure 2.2: *Single-branch sweeping spectrum scanner architecture; sweeping PLL is drawn in red to indicate the block that is more difficult to implement and contributes most to its energy consumption.*

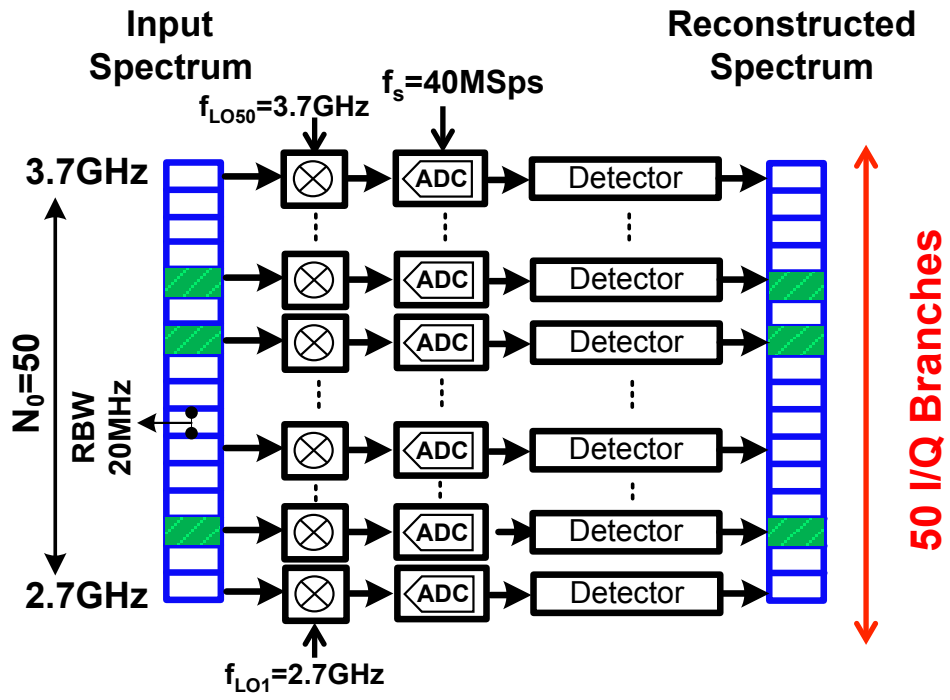

Figure 2.3: *Conceptual illustration of the operation of a traditional multi-branch spectral analysis technique applied for a 2.7-3.7GHz spectrum with a 20MHz RBW; the occupied spectrum bins are shaded in green.*

The scan time in sweeping scanners can in principle be reduced by using a multi-branch architecture with multiple narrowband scanners operating in parallel. However, the energy requirements do not improve but, to the first order, remain constant for a single-branch or a multi-branch realization.

For a 1GHz span ranging from 2.7 to 3.7GHz and a 20MHz RBW, a 50-branch realization as an example shown in Fig. 2.3, i.e. with a number of branches equal to N_0, would have a 50 times shorter scan time than a single-branch sweeping spectrum scanner, but at least a 50 times larger power consumption so that the energy consumption remains the same. However, the hardware complexity becomes impractical since the hardware consists of 50 branches and each branch re-

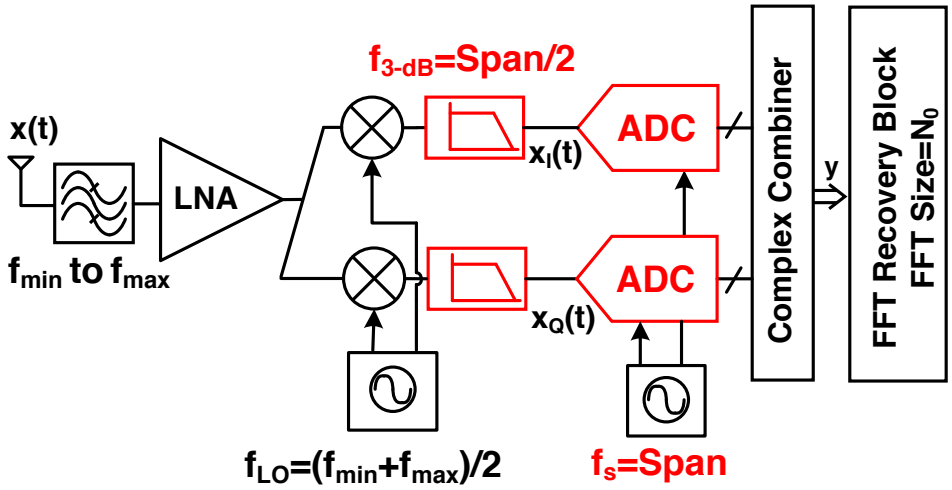

Figure 2.4: *Nyquist-rate FFT spectrum sensor architecture; low pass filters with a 3-dB bandwidth of Span/2 and ADCs with a sampling rate of Span are drawn in red to indicate the blocks that are more difficult to implement and contribute most to its energy consumption.*

quires a separate phase-locked loop (PLL) to generate the LO signal. The challenge is to generate the 50 PLL frequencies that would need to be spaced closely with a distance equal to the RBW.

A Nyquist-rate FFT spectrum sensor shown in Fig. 2.4 captures the wideband interest spectrum range with ADCs operating at a Nyquist rate of $Span/2$. Capturing the wideband interest spectrum information is followed by FFT-based digital signal processing with an FFT size of N_0 to map the information to the desired RBW.

As shown in Fig. 2.5, a Nyquist-rate FFT spectrum sensor would require a prohibitively high aggregate analog-to-digital (A/D) conversion rate of 2GSps after I/Q downconversion to sense a 1GHz bandwidth ranging from 2.7 to 3.7GHz. Even though the scan time is reduced, this is a power hungry approach due to the high sampling rate required for the Nyquist-rate wideband sensing.

A hybrid approach (see e.g. [18]) for a 1GHz bandwidth would have an IF bandwidth (IF_{BW}) limited to hundreds of MHz that is larger than the desired RBW (e.g. 20MHz) and it would be

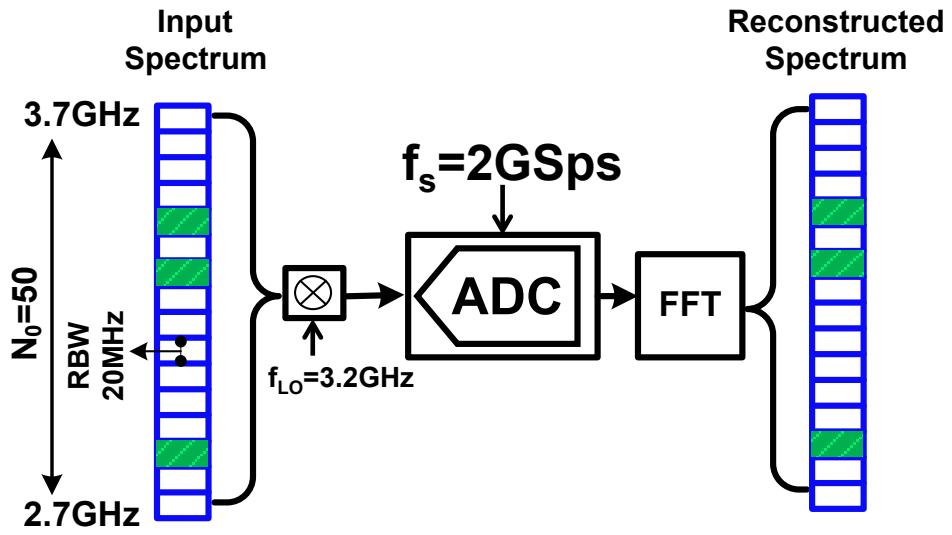

Figure 2.5: *Conceptual illustration of the operation of a traditional Nyquist-rate FFT spectral analysis technique applied for a 2.7-3.7GHz spectrum with a 20MHz RBW; the occupied spectrum bins are shaded in green.*

required to perform an FFT to further subdivide this into the desired RBW. This approach would not require as long a scan time as the single-branch sweeping spectrum scanner but the scan time would be limited by the IF bandwidth and the FFT size.

The energy consumption for a scan is given by the power consumption, P, times the scan time, T_{scan}, which has two contributions: front-end detector response time T_{resp} and recovery time T_{rec} (i.e. time required to complete the necessary signal processing):

$$E = P \cdot T_{scan} = P \cdot [T_{resp} + T_{rec}]. \tag{2.1}$$

The energy consumption for a single-branch sweeping spectrum scanner is given by:

$$E_{scanner} = P_{scanner} \cdot [N_0 \cdot (C_{settle}/BW_{filter}) + N_0 \cdot (N_s/f_s)] = P \cdot (N_0 \cdot T_{scan}). \tag{2.2}$$

where $P_{scanner}$ is the power consumption for a single-branch sweeping spectrum scanner; $T_{resp,scanner}$ is proportional to the number of bins, $N_0 = Span/RBW$, and the filter settling time which is inversely proportional to its bandwidth BW_{filter} ($BW_{filter} = RBW/2$); C_{settle} is the number of filter time constants needed for an accurate power reading[1]. $T_{rec,scanner}$ is proportional to the number of bins, N_0, the number of samples used for recovery, N_s, and inversely proportional to the ADC sampling rate, f_s.

The energy consumption for a multi-branch spectrum sensor is given by:

$$E_{multi} = P_{multi} \cdot [T_{resp,multi} + T_{rec,multi}] = P_{multi} \cdot [(C_{settle}/BW_{filter}) + (N_s/f_s)] = (N_0 \cdot P) \cdot T_{scan}. \quad (2.3)$$

For a multi-branch spectrum sensor, the scan time is reduced by N_0, while the power consumption P is increased by N_0 to the first order. So the energy consumption remains the same. Parallel architectures only allow the user to trade hardware complexity and power consumption for faster scan time.

The energy consumption for a Nyquist-rate FFT spectrum sensor is given by:

$$E_{nyquist} = P_{nyquist} \cdot [(C_{settle}/BW_{filter}) + N_0 \cdot (N_s/f_s)] \approx (N_0 \cdot P) \cdot T_{scan}. \quad (2.4)$$

For a Nyquist-rate FFT spectrum sensor, $T_{resp,nyquist}$ is proportional to the filter settling time which is inversely proportional to its bandwidth BW_{filter} ($BW_{filter} = Span/2$). This architecture subdivides the instantaneous BW into the desired RBW, $T_{rec,nyquist}$ is proportional to the FFT size,

[1] C_{settle} depends on the desired power reading accuracy; we estimate a C_{settle} value of 4 based on experiments with the Hewlett Packard 3585A spectrum analyzer.

N_0, the number of samples used for recovery, N_s, and inversely proportional to the ADC sampling rate, f_s. Since the ADC sampling rate is N_0 times higher than the sweeping spectrum scanner, the scan time is reduced by N_0.

For a Nyquist-rate FFT spectrum sensor, the ADC power is the dominant contribution to the power consumption. Assuming that the ADC FOM is $P_{ADC}/(f_s \cdot 2^{ENOB})$, to the first order, ADC power consumption is proportional to the sampling rate, f_s, (for this case f_s is the Nyquist rate for the Span/2) and the ADC resolution [19]. For a Nyquist-rate FFT spectrum sensor, the scan time is reduced by N_0 while the power consumption P is increased by N_0, so, to the first order, the energy consumption again remains the same.

Finally, for a hybrid approach, the scan time T_{scan} is reduced by IF_{BW}/RBW ($< N_0$); while the power consumption P is increased by IF_{BW}/RBW to the first order compared to a single-branch sweeping spectrum scanner so the energy consumption remains the same.

Performance summary of the traditional spectrum scanning or sensing solutions is shown in Table 2.1. We note that to a first order, the energy consumption remains constant for all architectures. Therefore, there is a fixed trade-off between scan time and power consumption.

The evolutionary sampling theorem 'Compressive Sampling' discussed in Chapter 3 that breaks the limitations of the traditional sampling is exploited for energy-efficient and rapid spectrum sensing. Compressive sampling (CS) [3, 4, 20–30] and other sub-Nyquist sampling methods [31–34] have the potential to deliver energy-efficient wideband spectrum sensors suitable for mobile terminal applications. In recent years, several CS approaches have been proposed to overcome the prohibitive energy costs associated with Nyquist-rate wideband spectrum sensing [4].

Table 2.1: *Performance summary of the traditional spectrum scanning or sensing solutions*

	Sweeping Scanner	Multi-branch Sensor	Nyquist-rate FFT Sensor
Scan Time	✗	✓	✓
Power Consumption	✓	✗	✗
Energy Consumption	✗	✗	✗
Hardware Complexity	✓	✗	✓
Branch Sampling Rate	✓	✓	✗

Chapter 3

Exploiting Compressive Sampling for Rapid Spectrum Sensing

3.1 Compressive Sampling to the Rescue

Compressive sampling (CS) is an evolutionary sampling paradigm that changes the perception of traditional sampling. The traditional Shannon/Nyquist sampling theorem requires uniformly sampling the signal at twice the maximum frequency of interest [35]. Conversely, CS is a blind sub-Nyquist sampling approach that allows the user to sample at a rate that is defined by the information bandwidth (a.k.a. signal bandwidth) rather than the instantaneous bandwidth with the prior assumption of sparsity [6, 7, 22, 23, 36–38].

Compressive sampling makes it possible to recover information from fewer measurements than the unknown signal values. Therefore, it tries to solve an 'underdetermined' system of linear equations (a.k.a. an ill-posed problem), that would have infinitely many solutions. With the prior assumption of sparsity, a unique solution, that is the 'sparsest solution', can be found for the underdetermined system of linear equations. The CS measurements are nonadaptive linear projections

onto an incoherent basis with the basis, where the signal could be defined as sparse with only a few nonzero coefficients [7, 37, 39].

Shown in Fig. 3.1 is an illustration of how compressive sampling remedies the spectrum sensing problem. The traditional multi-branch spectrum sensor with massively parallel branches (N_0 branches), which has one branch per bin of information, is an equivalent representation of a multi-pixel camera. The multi-branch spectrum sensor is a fast but impractical solution in terms of hardware complexity, energy consumption, and cost.

Compressive sampling has been extensively used for image reconstruction. It has been shown that a single-pixel camera that exploits CS has the ability to obtain an image with a single detection element, while measuring the image fewer times than the number of pixels with the prior assumption of sparsity [40, 41].

We exploited CS in the presented works to take a 'snapshot' of the spectrum, a 1-D spectrum image, with low energy consumption and high frequency resolutions. The compressed sampling quadrature analog-to-information converter shown in Fig. 3.1 is the equivalent of the CS single pixel camera [40, 41]. The QAIC takes a 'snapshot' of a 1GHz spectrum with only 8 I/Q branches, compared to 50 I/Q employed by a traditional multi-branch spectrum sensor. Therefore, a CS spectrum sensor with a QAIC offers more than a sixfold reduction in the number of branches.

3.2 Using Compressive Sampling for Spectrum Sensing

We apply compressive sampling [6, 7] to break the energy consumption, scan time and hardware complexity trade-off. We are interested in detecting active interferers above a certain signal-level

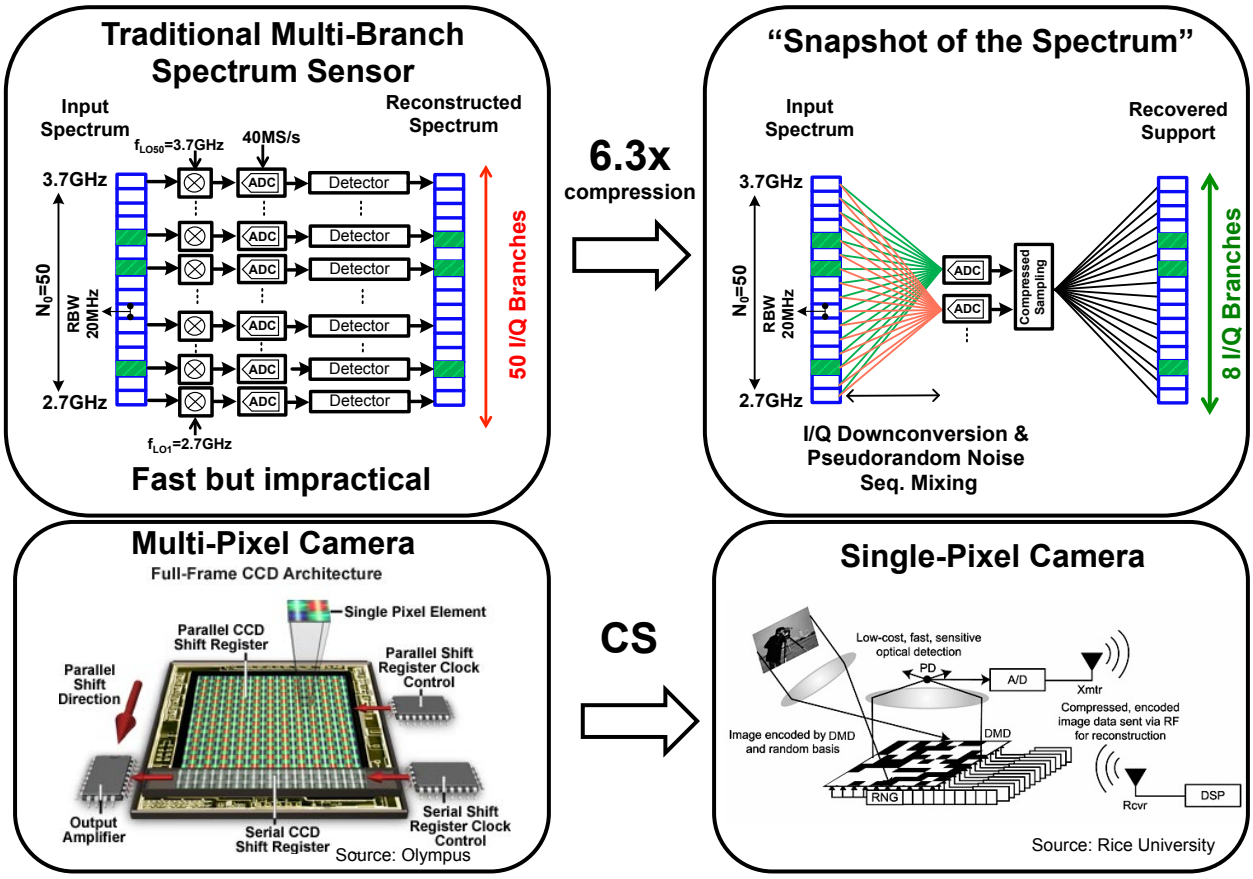

Figure 3.1: *Compressive sampling evolution from imaging to spectrum sensing.*

threshold, which can be represented by sparse multi-band signal model shown in Fig. 3.2 [4, 23]. Sparse multi-band signal model, that is used in modulated wideband converter (MWC) type architectures [23, 42, 43] and in our band-pass CS architectures, QAIC [3–5] and TS-QAIC [8], is explained in detail in Section 3.2.1.

CS spectrum sensors use incoherent measurements obtained by mixing the wideband RF input signal with independent unique pseudorandom noise (PN) sequences that fold the wideband input signal onto narrowband baseband channels. CS digital signal processing (DSP) techniques identify the active bands (a.k.a. supports) from the samples. A band is considered active if it contains energy above a certain adaptive threshold.

CS signal detection [25, 44–46] is a statistical process and key metrics are the detection probability P_D, and the false alarm probability P_{FA}. P_D is the probability that the detector indeed correctly detects an interferer that is present in the RF input spectrum; P_{FA} is the probability that the detector reports a spectrum bin as occupied when there is no signal present in the RF input spectrum.

In a CS spectrum sensor the required number of parallel branches [4, 42], m_{CS}, is significantly smaller than N_0 and it is determined by the maximum number of supports, K_0, the length of the PN sequence, L, and a constant, C:

$$m_{CS} \approx C \cdot K_0 \cdot \log\left(\frac{L}{K_0}\right). \tag{3.1}$$

3.2.1 Sparse Multi-band Signal Model

We consider real-valued, square-integrable signals, $x(t)$, as our *sparse multi-band signals* [4, 23]. The sparse multi-band signal $x(t)$ satisfies two properties: (i) the Fourier transform $X(f)$ vanishes

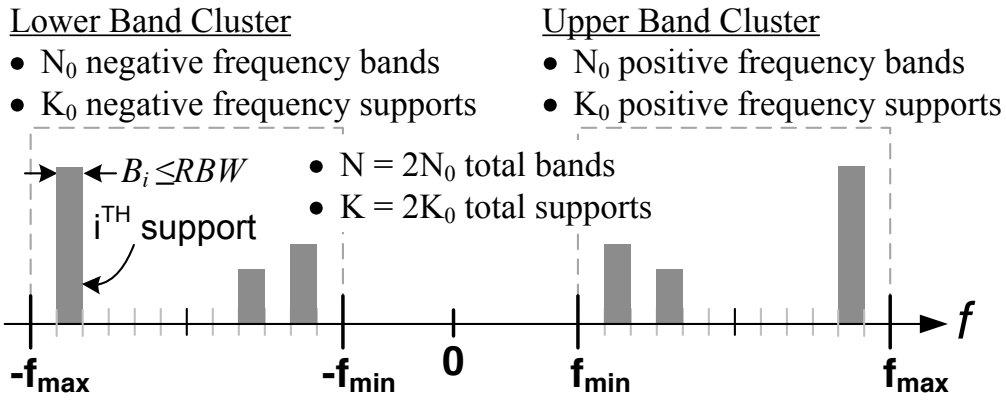

Figure 3.2: *Example of a sparse multi-band signal spectrum with its signal parameters.*

outside of a known interval $\mathcal{F} = (-f_{max}, -f_{min}] \bigcup [f_{min}, f_{max})$ and (ii) the support of $X(f)$ is a relatively small subset of $\mathcal{F}$ (i.e., $X(f)$ is *sparse*).

To formalize the second property, we assume that $\mathcal{F}$ has been partitioned into $N = 2N_0$ disjoint bands, each of width at most RBW, and that $X(f)$ is supported on only $K = 2K_0 < N = 2N_0$ of these bands. Specifically, the power of $2K_0$ bands exceeds a predefined level (a.k.a. threshold). We refer to these $2K_0$ bands as active bands or supports. If the *spectral occupancy* K_0/N_0 is small, then the support of $X(f)$ has Lebesgue measure $\leq K \cdot RBW$ Hz much smaller than the Nyquist bandwidth, twice the maximum frequency ($f_{NYQ} = 2f_{max}$ Hz) of the signal $x(t)$.

An example of a sparse multi-band signal spectrum is shown in Fig. 3.2. We let $\mathcal{M}$ denote the set of such sparse multi-band signals. Our goal is to efficiently sense signals from $\mathcal{M}$, even if the spectral locations of the K supports are not known in advance.

3.2.2 Existing Low-pass CS Architectures

Existing low-pass CS architectures [26, 28, 42, 43], such as the modulated wideband converter (MWC) [42, 43] shown in Fig. 3.3, sense the input spectrum from DC to f_{max}. Since the MWC operates on a real signal $x(t)$, it processes $2N_0$ total bands with $2K_0$ active supports. The required number of branches for the MWC is m_{MWC}. The input signal $x(t)$ is first amplified by a low noise amplifier and then mixed with m_{MWC} unique PN sequences and low pass filtered. These +1/-1 unique PN sequences need to have low cross-correlation for robust recovery performance.

The MWC uses ADCs operating at a rate commensurate with the desired resolution bandwidth and the aggregate sampling rate is lower than the traditional Nyquist-rate architectures thanks to the use of CS DSP techniques and the reduction in the number of branches. While the aggregate sampling rate and the power consumption of the ADCs are reduced, the need to mix with high-rate PN sequences diminishes the energy savings.

In a low-pass CS MWC architecture the clock rate, f_{CLK}, of the PN sequences is set by the Nyquist rate for f_{max} ($f_{CLK} \geq 2f_{max}$), while the length of the sequences depends on the desired RBW, $L = f_{CLK}/RBW$. E.g., to sense a 1GHz span ranging from 2.7 to 3.7GHz with 3 active interferers with a 20MHz RBW, f_{CLK} is 10.22GHz for a 511-long maximal length sequence (m-sequence) based on a linear feedback shift register (LFSR) implementation. Since an LFSR based implementation by using n flip-flops generates m-sequences with $2^n - 1$ length, 511 is the shortest length to obtain 20MHz RBW and generate an m-sequence that operates at a rate, $f_{CLK} \geq 2f_{max}$. Also the required m_{MWC} is 29, proportional to the K_0 and the logarithmic factor (L/K_0) given in (3.1). See Table 4.1 for the details. Since the m_{MWC} is reduced to 29, the aggregate sampling

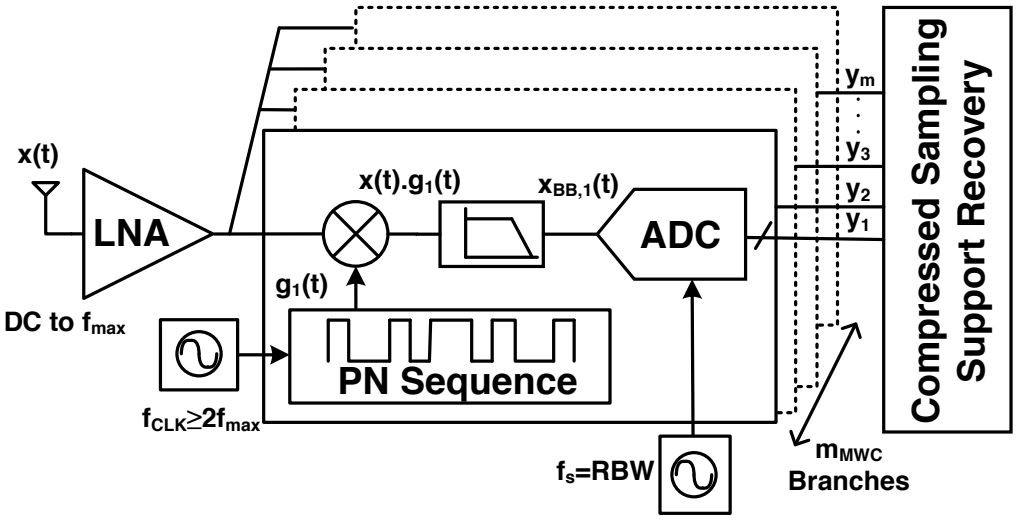

Figure 3.3: *Low-pass compressed sampling spectrum sensor employing a modulated wideband converter architecture; for a maximum input signal frequency, f_{max}, of 3.7GHz and a RBW of 20MHz, the PN sequence clock frequency, f_{CLK}, needs to be 10.22GHz and the sequence length needs to be 511 for an LFSR implementation; to recover up to 3 interferers, 29 branches are required.*

rate is 580MSps compared to 2GSps for a traditional Nyquist-rate architectures. The low-pass CS MWC architecture offers a 3.45 times compression in the aggregate sampling rate to sense a 1GHz of spectrum ranging from 2.7 to 3.7GHz. In practical realizations, the generation and distribution of the high-rate PN sequences is the most power hungry block of the low-pass CS architectures [26, 28].

Fig. 3.4 shows how low-pass compressive sampling maps the information in the input spectrum onto the m_{MWC} branches. The m_{MWC} unique PN sequences fold the wideband input RF signal ranging from DC to f_{max} onto m_{MWC} narrowband baseband channels. After A/D conversion, the CS DSP disentangles the information and identifies the supports (i.e. the interferers). For a spectrum sensing application where there are no signals of interest below f_{min}, the sensitivity is degraded due

to the extra noise folding in from DC to f_{min} frequency range in the low-pass compressed sensing approach.

Fig. 3.5 also shows the spectra of the signals at various nodes of a branch i of the low-pass CS spectrum sensor. $X(f)$ is the band of interest from 2.7 to 3.7GHz with K_0 active bands (interferers) above a certain threshold level. The spectrum of $G_i(f)$ with a length, L, and $f_p = f_{CLK}/L$ which is equal to RBW, is estimated by spectral lines δ with a sinc square shape with the following relation [47]:

$$G_i(f) = \left[\sum_{\substack{r=-\infty \\ r\neq 0}}^{\infty} \delta(f - r f_p) \right] \frac{L+1}{L^2} \left(\frac{\sin \pi f / f_{CLK}}{\pi f / f_{CLK}} \right)^2 + \frac{1}{L^2} \delta(f); \tag{3.2}$$

the main lobe of the sinc square shaped spectrum $G_i(f)$ extends from DC to twice the maximum frequency (f_{max}). The spectrum of the output signal of the PN mixer is the convolution of the PN sequence $G_i(f)$ spectrum with the input spectrum as shown in Fig. 3.5. Mixing with a PN sequence spreads the spectrum, shifts the information of each band by multiples of RBW, and every bin contains energy from all bins. After low pass filtering, the signal $x_{BB,i}$ is obtained that contains one replica of the folded spectrum which is then sampled and converted into the digital domain. The CS signal recovery provides an index set of active interferer locations.

For an MWC based spectrum sensor, the scan time contributors are the front-end detector response time $T_{resp,MWC}$ and recovery time $T_{rec,MWC}$ (3.3). Energy consumption for an MWC based spectrum sensor is given by:

$$E_{MWC} = P_{MWC} \cdot [T_{resp,MWC} + T_{rec,MWC}] = P_{MWC} \cdot [(C_{settle}/BW_{filter}) + (N_s/f_s)] = P_{MWC} \cdot T_{scan}. \tag{3.3}$$

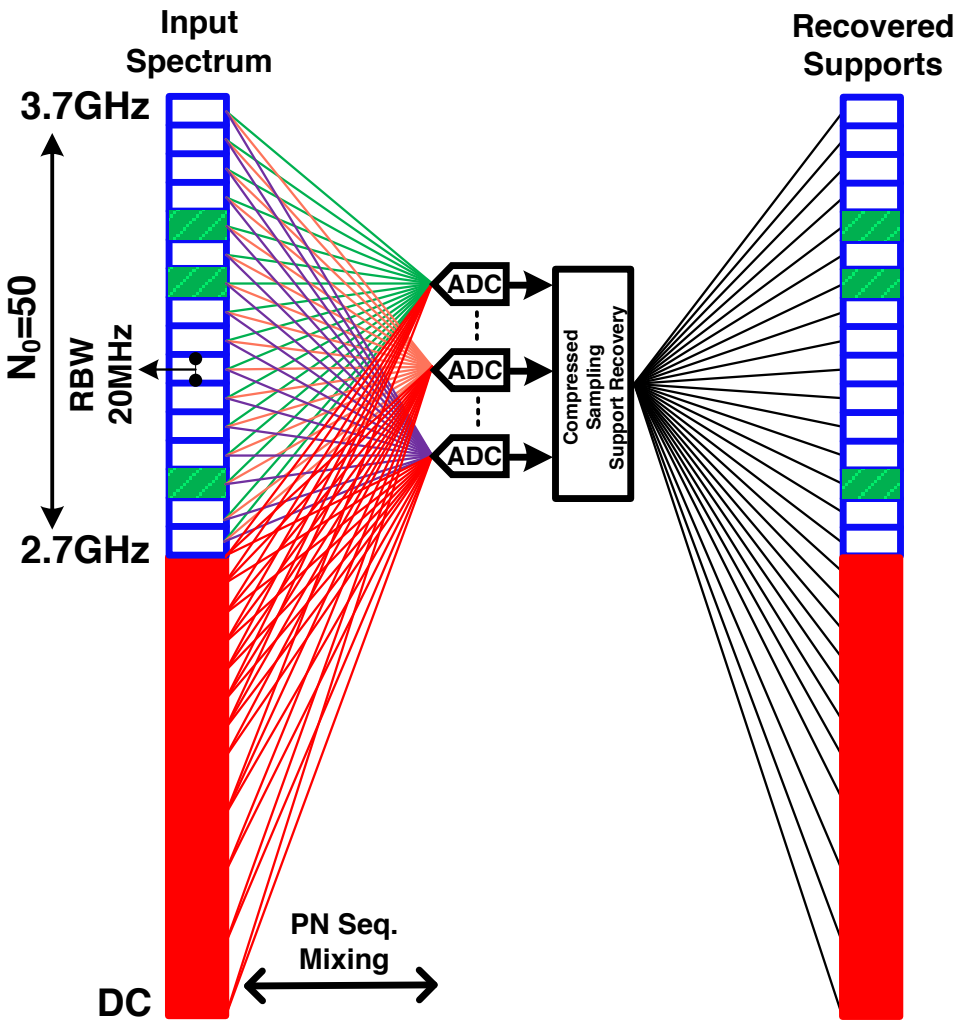

Figure 3.4: *Conceptual illustration of the operation of the low-pass compressed sampling spectrum sensor employing a modulated wideband converter shown in Fig. 3.3; the occupied spectrum bins are shaded in green.*

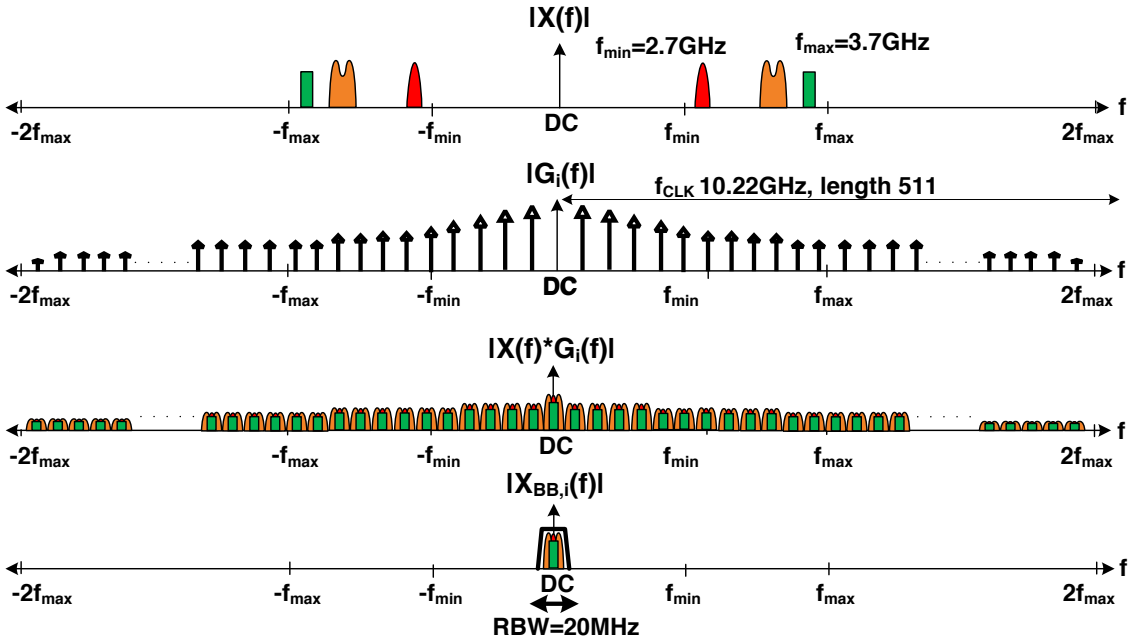

Figure 3.5: *Spectra of the key signals of the low-pass compressed sampling spectrum sensor employing a modulated wideband converter shown in Fig. 3.3.*

To sense a 1GHz of span ranging from 2.7 to 3.7GHz, the MWC based spectrum sensor offers 50 times faster scan time compared to the sweeping spectrum scanners, 3 to 4 times compression in the aggregate sampling rate compared to multi-branch spectrum sensors and Nyquist-rate FFT spectrum scanners. The low-pass CS MWC based spectrum sensor also offers 3 to 4 times compression in the number of branches compared to multi-branch spectrum sensors. However due to the high rate and long length of the PN sequences, the power consumption of an MWC based spectrum sensor, P_{MWC}, is relatively high which diminishes the potential energy savings compared to traditional approaches.

A band-pass CS architecture shown in Fig. 3.6 is proposed as an enabling solution for rapid interferer detection over a wide span at the same time with lower power consumption, reduced

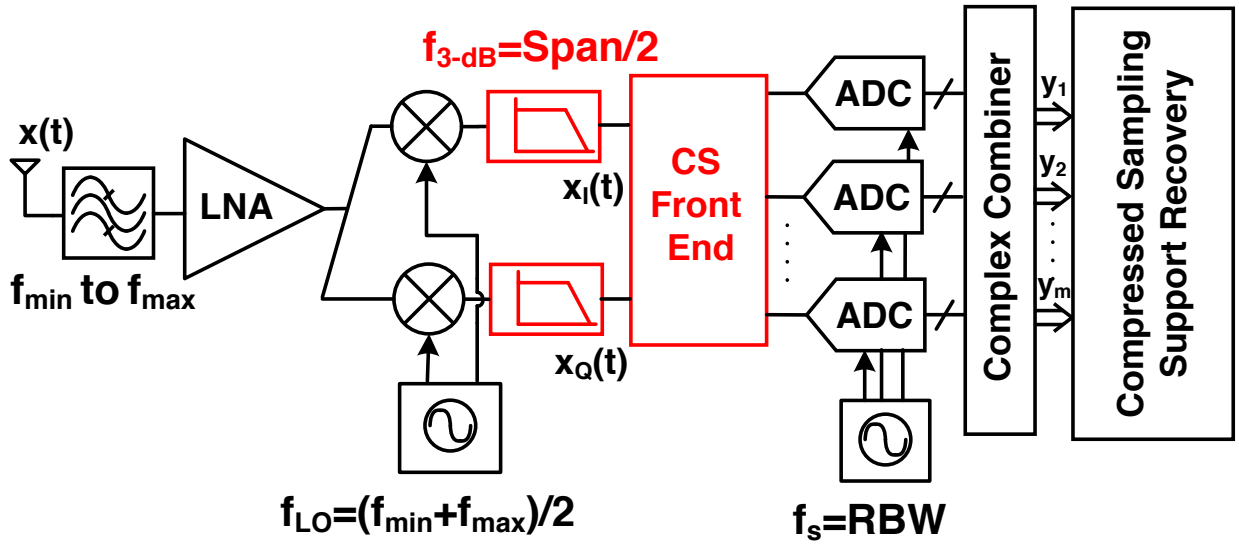

Figure 3.6: *Band-pass compressed sampling (CS) architecture; low pass filters with a 3-dB bandwidth of Span/2 and CS front end that consists of several PN mixing stages are drawn in red to indicate the blocks that are more difficult to implement and contribute most to its energy consumption.*

number of branches and improved sensitivity compared to the existing low-pass CS architectures, while breaking the limitation of the sampling in traditional Nyquist-rate architectures by employing the CS front-end block prior to ADCs operating at a sub-Nyquist rate shown in Fig. 3.6. The band-pass CS architecture overcomes the majority of the limitations associated with the existing low-pass CS architectures, but it still has an intrinsic trade-off between the instantaneous bandwidth and the instantaneous dynamic range.

Chapter 4

Energy-Efficient, Wideband and Rapid Interferer Detectors with Compressed Sampling Quadrature Analog-to-Information Converters

4.1 Using the Quadrature Analog-to-Information Converter for Spectrum Sensing

In [3–5], we introduced a quadrature analog-to-information converter (QAIC) architecture shown in Fig. 4.1. QAIC is a band-pass architecture and only senses the spectrum from f_{min} to f_{max} which is superior for spectral analysis applications. The required number of branches for QAIC is m_{QAIC}. The QAIC consists of a wideband LNA followed by a wideband RF I/Q downconverter and baseband I/Q PN mixing branches driven by m_{QAIC} unique PN sequences.

Thanks to the signal bandwidth reduction performed by the RF I/Q downconverter stage at the input of the I/Q PN mixers, the f_{CLK} for the PN sequences is now only (f_{max}-f_{min}), while the length of the sequences depends on the desired RBW, $L = f_{CLK}/RBW$. For a 1GHz frequency span and

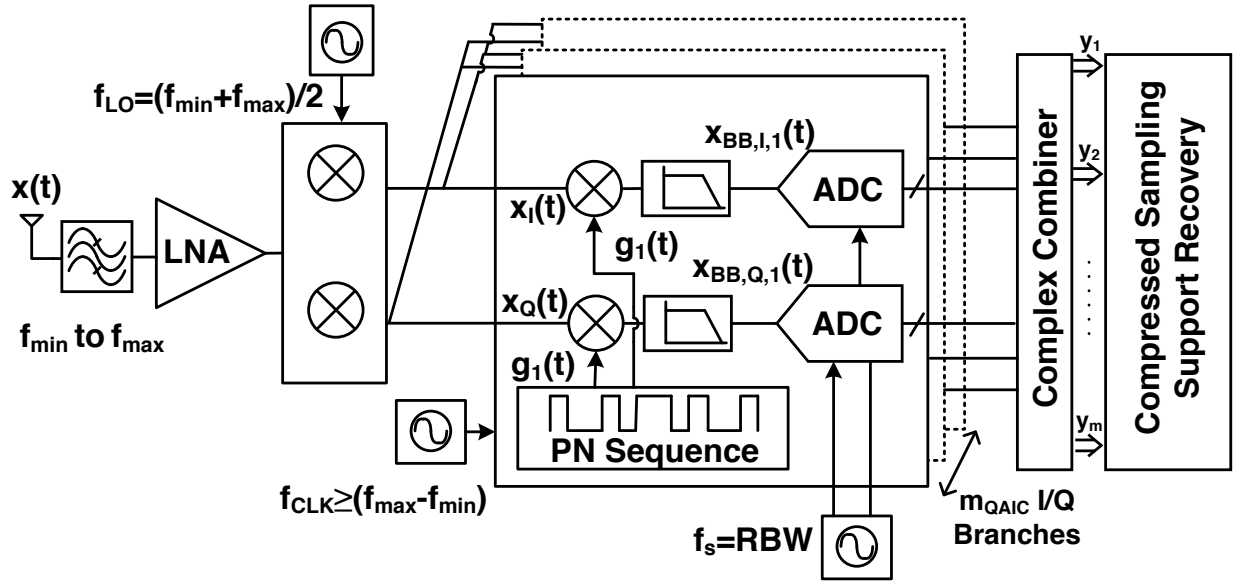

Figure 4.1: *Proposed band-pass compressed sampling spectrum sensor employing a quadrature analog-to-information converter (QAIC) architecture. For an input signal frequency range* $[f_{min}, f_{max}]$ *from 2.7 to 3.7GHz and a RBW of 20MHz the PN sequence clock frequency,* f_{CLK} *needs to be 1.26GHz and the sequence length needs to be 63 for an LFSR implementation. To recover up to 3 interferers, 8 I/Q branches are required.*

RBW of 20MHz, f_{CLK} is 1.26GHz with a 63-long LFSR implementation. The reduced clock rate and the reduced length of the PN sequences yield significant power savings compared to low-pass CS architectures.

Fig. 4.2 shows how the QAIC processes the information in the input spectrum. The band-pass compressed sampling approach folds the information onto narrowband baseband channels from all bins ranging from 2.7 to 3.7GHz by first mixing with an I/Q LO signal and then mixing the complex baseband signal with 8 unique +1/-1 pseudorandom noise sequences. Compressed sampling support recovery to disentangle this mapping is performed in the information recovery engine (IRE) with complex domain signals in this work.

Fig. 4.3 shows the spectrum at various nodes of a branch *i* of the band-pass CS architecture.

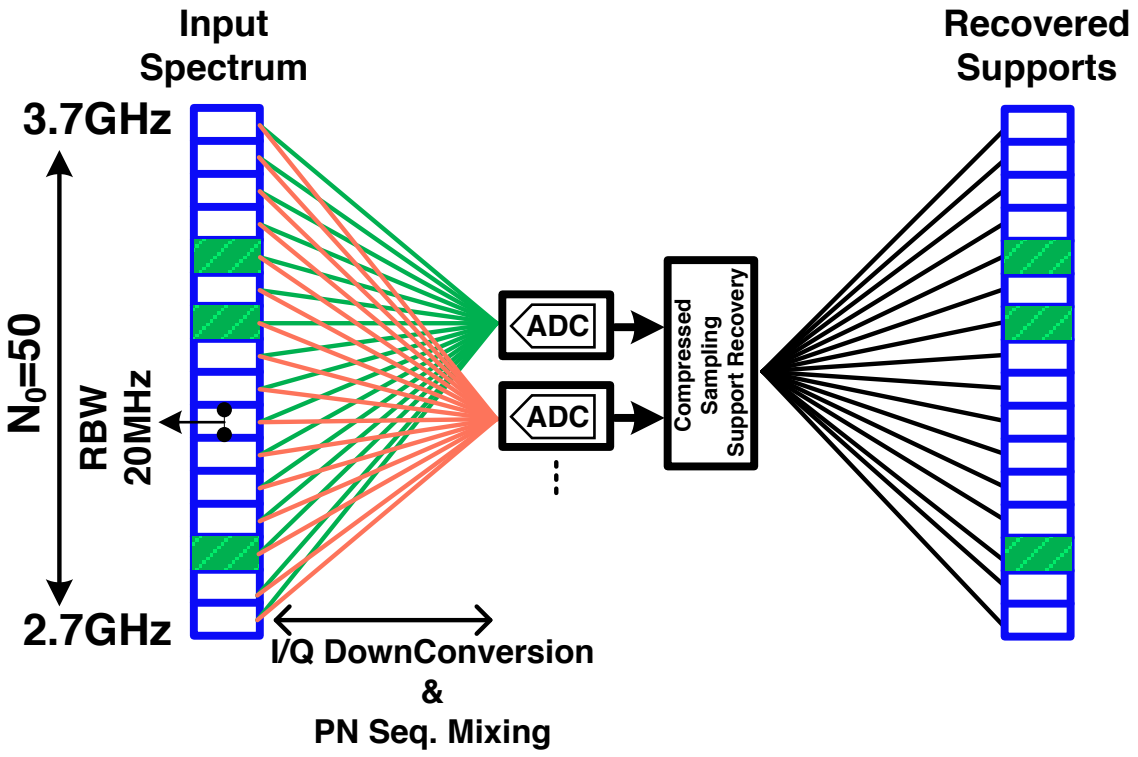

Figure 4.2: *Conceptual illustration of the operation of the band-pass compressed sampling spectrum sensor employing a QAIC shown in Fig. 4.1; the occupied spectrum bins are shaded in green.*

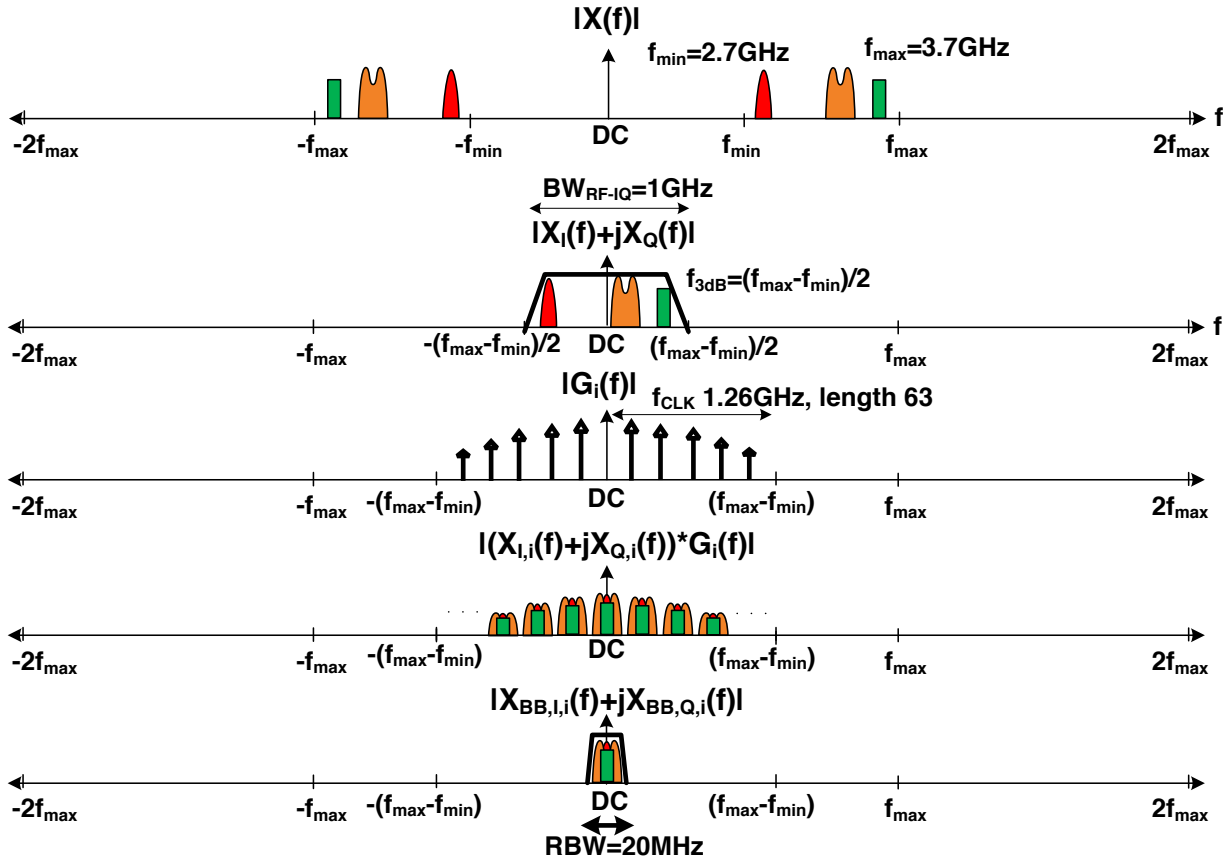

Figure 4.3: *Spectra of the key signals in the band-pass compressed sampling spectrum sensor employing a QAIC shown in Fig. 4.1 [3].*

$X(f)$ is the interest spectrum band ranging from 2.7 to 3.7GHz with K_0 active bands (interferers) above a certain threshold level. $X_{I,i}(f) + jX_{Q,i}(f)$ shows the down converted complex baseband signal in branch i around DC after the filtering with a 3-dB BW of $(f_{max} - f_{min})/2$. $G_i(f)$ is the spectrum of the i^{th} PN sequence with a length of 63 and a clock rate of 1.26GHz. Convolution of the PN sequence $G_i(f)$ spectrum with the band-limited complex baseband spectrum and low pass filtering with a 3-dB BW of $RBW/2$ in the I and Q legs yields the complex-domain baseband output $X_{BB,I,i}(f) + jX_{BB,Q,i}(f)$ which is then digitized.

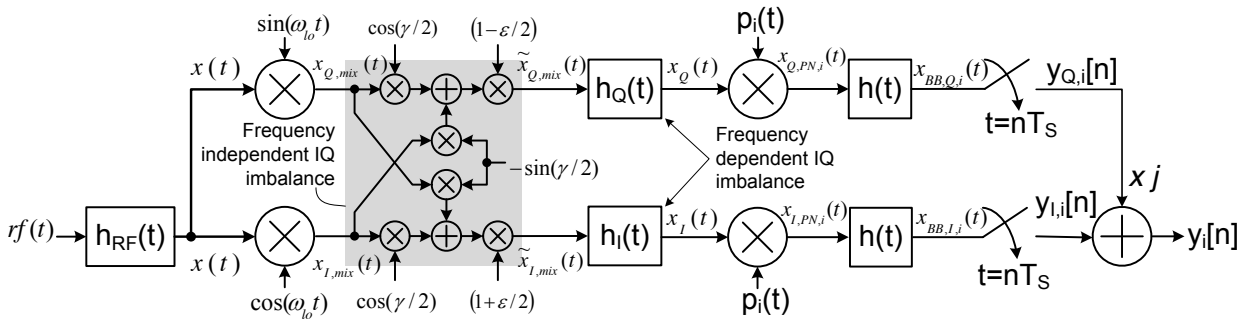

Figure 4.4: *QAIC block diagram used to derive a set of equations that describe the QAIC system operation*

4.2 Frequency Domain Analysis of a QAIC

The QAIC block diagram shown in Fig. 4.4 is used to derive a set of equations that describe the QAIC system operation. Since the key new subsystem block introduced into the QAIC is the downconverter, its impairments are included in the frequency domain model. Only linear impairments are considered in this analysis. The downconverter frequency independent impairment model described by (4.1) is shown in Fig. 4.4.

$$\begin{pmatrix} \tilde{x}_{I,mix}(t) \\ \\ \tilde{x}_{Q,mix}(t) \end{pmatrix} = \begin{pmatrix} \kappa_{11} & \kappa_{12} \\ \\ \kappa_{21} & \kappa_{22} \end{pmatrix} \begin{pmatrix} x_{I,mix}(t) \\ \\ x_{Q,mix}(t) \end{pmatrix} \tag{4.1}$$

The in-phase (I) and quadrature-phase (Q) local oscillator signals of the downconverter, $LO_I(t)$ and $LO_Q(t)$, are modeled as (4.2) [48]. The parameters ε and γ specify the downconverter gain imbalance and phase imbalance.

$$\begin{aligned} LO_I(t) &= (1+\varepsilon/2)\cdot\cos(\omega_{lo}t+\gamma/2) \\ LO_Q(t) &= (1-\varepsilon/2)\cdot\sin(\omega_{lo}t-\gamma/2) \end{aligned} \tag{4.2}$$

The composite parameters that models the phase and gain imbalance of the I/Q downconverter in (4.1) are given by (4.3).

$$\begin{aligned}
\kappa_{11} &= (1+\varepsilon/2)\cdot\cos(\gamma/2) \\
\kappa_{12} &= -(1+\varepsilon/2)\cdot\sin(\gamma/2) \\
\kappa_{21} &= -(1-\varepsilon/2)\cdot\sin(\gamma/2) \\
\kappa_{22} &= (1-\varepsilon/2)\cdot\cos(\gamma/2)
\end{aligned} \tag{4.3}$$

The frequency dependent mismatch [49] between the I and Q paths introduced by the downconverter and other components is modeled with low-pass filters $h_I(t)$ and $h_Q(t)$ as illustrated in Fig. 4.4. For the purpose of this analysis, frequency dependent I, Q mismatch is ignored and only frequency independent I, Q impairments are included in the rest of the analysis.

Let $x(t) \in \mathcal{M}$ be a sparse multi-band signal as defined in Section 3.2.1. $x_I(t)$ and $x_Q(t)$ are the low-pass filtered outputs of the I/Q downconverter. Assume that $p_i(t)$ is a T_p-periodic PN sequence of length $L = 2L_0 + 1$, where $L_0 \in \mathbb{Z}^+$. Let $f_p = 1/T_p$ and therefore, $p_i(t) = \sum_{n=-\infty}^{\infty} b_{i,n}\, e^{j2\pi n f_p t}$. The weights $b_{i,n}$ are evaluated in (4.4), where $\beta_{i,0} \ldots \beta_{i,L-1}$ are the amplitudes of the i^{th} branch PN sequence employed by the QAIC [47]. Note that $\theta_n = (1 - e^{-j\frac{2\pi}{L}n})/\, j2\pi n$ and $\psi_{n,k} = e^{(-j\frac{2\pi}{L}nk)}$ in (4.4).

$$b_{i,n} = \begin{cases} \frac{1}{L}\sum_{k=0}^{L-1} \beta_{i,k} & \text{when } n = 0 \\ \sum_{k=0}^{L-1} \beta_{i,k}\, \theta_n\, \psi_{n,k} & \text{when } n \neq 0 \end{cases} \tag{4.4}$$

The Fourier transform of $x_{BB,I,i}(t) = x_{I,PN,i}(t) * h(t)$ and $x_{BB,Q,i}(t) = x_{Q,PN,i}(t) * h(t)$ are given in

(4.5). The inputs $X_{I,PN,i}(f)$ and $X_{Q,PN,i}(f)$ to the filters with impulse response $h(t)$ are linear combinations of the f_p shifted copies of $X_I(f)$ and $X_Q(f)$.

$$\begin{aligned} X_{BB,I,i}(f) &= \sum_{n=-L_0}^{L_0} b_{i,n} \left[\kappa_{11} X_{I,mix}(f-nf_p) + \kappa_{12} X_{Q,mix}(f-nf_p)\right] \\ X_{BB,Q,i}(f) &= \sum_{n=-L_0}^{L_0} b_{i,n} \left[\kappa_{21} X_{I,mix}(f-nf_p) + \kappa_{22} X_{Q,mix}(f-nf_p)\right] \end{aligned} \tag{4.5}$$

Since $X_I(f)$, $X_Q(f) = 0$ when f is not in the range $-(f_{max}-f_{min})/2$ to $(f_{max}-f_{min})/2$, the Fourier transform in (4.5) can be expressed with a finite sum. The signals $x_{BB,I,i}(t)$ and $x_{BB,Q,i}(t)$ are sampled at f_s samples per second. The samples $y_{I,i}[n]$ and $y_{Q,i}[n]$ are combined and the output of the complex combiner $y_i[n]$ are used to recover the support of the input signal $x(t)$. The Fourier transform of the signals $y_i[n]$ is given in (4.6).

$$\begin{aligned} Y_i(e^{j2\pi f T_s}) = \frac{1}{T_s} \sum_{n=-L_0}^{L_0} \sum_{k=0}^{L-1} \{ \\ \beta_{i,k}\, \psi_{n,k}\, \theta_n [\kappa_{11} X_{I,mix}(f-nf_p) + \kappa_{12} X_{Q,mix}(f-nf_p)] \mp \\ j\, \beta_{i,k}\, \psi_{n,k}\, \theta_n [\kappa_{21} X_{I,mix}(f-nf_p) + \kappa_{22} X_{Q,mix}(f-nf_p)] \} \end{aligned} \tag{4.6}$$

The QAIC operation is described by (4.7), where $\tilde{\mathbf{\Phi}} \in \mathbb{R}^{2m \times 2L}$ is the sensing matrix, $\tilde{\mathbf{\Psi}} \in \mathbb{C}^{2L \times 2L}$ is the dictionary matrix and $\tilde{\mathbf{\Theta}} \in \mathbb{C}^{2L \times 2L}$ is a diagonal matrix containing a set of complex weights.

$$\boldsymbol{Y}(e^{j2\pi f T_s}) = \boldsymbol{A}\, \tilde{\boldsymbol{z}}(f) = \mathbf{\Sigma} \tilde{\mathbf{\Phi}} \tilde{\mathbf{\Psi}} \tilde{\mathbf{\Theta}} \boldsymbol{\mathcal{K}}\, \tilde{\boldsymbol{z}}(f) \tag{4.7}$$

The matrices $\mathbf{\Sigma}$ and $\boldsymbol{\mathcal{K}}$ represent the complex combiner action and the downconverter impair-

ments respectively. The complex combiner action is described by the matrix $\mathbf{\Sigma} \in \mathbb{C}^{m\times 2m}$ given in (4.8).

$$\mathbf{\Sigma} = \left[\begin{array}{ccc|ccc} 1 & \cdots & 0 & \mp j & \cdots & 0 \\ \vdots & \ddots & \vdots & \vdots & \ddots & \vdots \\ 0 & \cdots & 1 & 0 & \cdots & \mp j \end{array}\right] \tag{4.8}$$

The block diagonal matrices $\tilde{\mathbf{\Phi}} \in \mathbb{R}^{2m\times 2L}$, $\tilde{\mathbf{\Psi}} \in \mathbb{C}^{2L\times 2L}$ and $\tilde{\mathbf{\Theta}} \in \mathbb{C}^{2L\times 2L}$ described in (4.9) consist of the matrices $\mathbf{\Phi} \in \mathbb{R}^{m\times L}$, $\mathbf{\Psi} \in \mathbb{C}^{L\times L}$ and $\mathbf{\Theta} \in \mathbb{C}^{L\times L}$ respectively. The rows of the matrix $\mathbf{\Phi}$ contain the amplitudes of the m_{QAIC} unique pseudo-random noise sequences employed by the QAIC. $\mathbf{\Psi}$ is a discrete Fourier transform matrix and $\mathbf{\Theta}$ is a diagonal matrix containing the complex weights θ_n given in equation (4.4).

$$\tilde{\mathbf{\Phi}} = \left[\begin{array}{c|c} \mathbf{\Phi} & 0 \\ \hline 0 & \mathbf{\Phi} \end{array}\right]; \tilde{\mathbf{\Psi}} = \left[\begin{array}{c|c} \mathbf{\Psi} & 0 \\ \hline 0 & \mathbf{\Psi} \end{array}\right]; \tilde{\mathbf{\Theta}} = \left[\begin{array}{c|c} \mathbf{\Theta} & 0 \\ \hline 0 & \mathbf{\Theta} \end{array}\right] \tag{4.9}$$

The action of the quadrature RF downconverter with frequency independent linear impairments is described by the matrix $\mathcal{K} \in \mathbb{R}^{2L\times 2L}$ given in (4.10). The entries of the matrix $\mathcal{K}$ are those given

in (4.1). We note that $\boldsymbol{\mathcal{K}}$ is an identity matrix for an impairment free downconverter.

$$\boldsymbol{\mathcal{K}} = \left[\begin{array}{ccc|ccc} \kappa_{11} & \cdots & 0 & \kappa_{1,2} & \cdots & 0 \\ \vdots & \ddots & \vdots & \vdots & \ddots & \vdots \\ 0 & \cdots & \kappa_{11} & 0 & \cdots & \kappa_{12} \\ \hline \kappa_{2,1} & \cdots & 0 & \kappa_{22} & \cdots & 0 \\ \vdots & \ddots & \vdots & \vdots & \ddots & \vdots \\ 0 & \cdots & \kappa_{2,1} & 0 & \cdots & \kappa_{22} \end{array}\right] \tag{4.10}$$

The vector $\tilde{\boldsymbol{z}}(f) \in \mathbb{C}^{2L}$ in (4.7) includes all of the $(2L_0+1)$ frequency shifts of $X_{I,mix}(f)$ and $X_{Q,mix}(f)$ by f_p Hz. The vector $\tilde{\boldsymbol{z}}(f)$ is described in (4.11).

$$\tilde{\boldsymbol{z}}(f) = \begin{pmatrix} \frac{1}{2}[X(f-f_{lo}+L_0f_p)+X(f+f_{lo}+L_0f_p)] \\ \vdots \\ \frac{1}{2}[X(f-f_{lo}-L_0f_p)+X(f+f_{lo}-L_0f_p)] \\ \\ \frac{1}{2j}[X(f-f_{lo}+L_0f_p)-X(f+f_{lo}+L_0f_p)] \\ \vdots \\ \frac{1}{2j}[X(f-f_{lo}-L_0f_p)-X(f+f_{lo}-L_0f_p)] \end{pmatrix} \tag{4.11}$$

Given observations (4.7), we can attempt to recover the sparse vectors $\tilde{\boldsymbol{z}}(f)$ from measurements $\boldsymbol{Y}(f)$, and hence determine the frequency support of the input signal $x(t)$. This can be done efficiently using techniques from convex optimization [6, 7, 36, 37] if the matrix $\boldsymbol{A}$ in (4.7) respects

the geometry of the sparse vector $\tilde{\boldsymbol{z}}(f)$. Specifically, if for a small constant δ, (4.12) holds then the sampling and reconstruction procedure will succeed.

$$(1-\delta)\|\boldsymbol{s}\|_2^2 \leq \|\boldsymbol{A}\boldsymbol{s}\|_2^2 \leq (1+\delta)\|\boldsymbol{s}\|_2^2 \quad \forall\, 2K_0\text{-sparse } \boldsymbol{s} \tag{4.12}$$

For example, if in (4.7) $\tilde{\boldsymbol{\Phi}}$ is a random matrix (say with entries independent uniform ± 1), the product $\tilde{\boldsymbol{\Phi}}\tilde{\boldsymbol{\Psi}}$ satisfies requirement (4.12) with high probability.

4.2.1 System Design Parameters of Band-pass and Low-pass Compressed Sampling Architectures

Low-pass CS architectures, like the MWC [42] sample a real signal $x(t) \in \mathcal{M}$ at RF. Its frequency span extends from DC to f_{max} and contains $N_0 = \lceil f_{max}/RBW \rceil$ bands. The PN mixing stages employed by the MWC processes $2N_0$ total bands (N_0 positive, N_0 negative frequency bands) and $2K_0$ active bands or supports [42]. In contrast, band-pass CS architectures, like the QAIC [3–5] and the TS-QAIC sample a complex signal $x_I(t) + j \cdot x_Q(t)$ at an intermediate frequency (IF). Span of the band-pass CS architectures extends from f_{min} to f_{max} and contains $N_0 = \lceil (f_{max} - f_{min})/RBW \rceil$ total bands. The I and Q path PN mixing stages employed by the QAIC together process N_0 total bands and K_0 active bands. We note that the number of bands $2N_0$ processed by the MWC is much larger than that processed by the QAIC when $f_{min} >> 0$. The downconverter parameters f_{lo} (local oscillator frequency) and f_{3dB-RF} (RF low-pass filter bandwidth) afford the QAIC an additional degree of frequency span adjustability compared to the MWC. Employing values for the parameter

pair $\{f_{lo}, f_{3dB-RF}\}$ as shown in Table 4.1, both the lower and upper ends of the QAIC frequency span may be adjusted. In contrast, only the upper end of the MWC span is adjustable and this has significant sensitivity implications. Note however, that the QAIC flexibility comes at the cost of an unwanted band cluster residual at IF caused by I, Q path gain and phase imbalances. Depending on the level of I, Q imbalance, this can increase the false alarm probability of the QAIC.

It is assumed that both the MWC and QAIC systems employ maximal length PN sequences generated with linear feedback shift register (LFSR) structures. The sequence length L is equal to $2^n - 1$, where $n \in \mathbb{Z}^+$ for a maximal length LFSR type PN sequence. The number of shift registers n in the LFSR structure must be chosen such that $L \geq 2N_0$ for the MWC and $L \geq N_0$ for the QAIC. The chipping frequency f_{CLK} of the PN sequences employed by the MWC must be greater than twice the maximum frequency f_{max} of the input signal. See [42] for details. In contrast, f_{CLK} for the QAIC must be greater than the band cluster width ($f_{max} - f_{min}$) of the input signal. Note that for an input signal with $f_{min} >> 0$ the difference between the chipping frequency and length of the PN sequences employed by the MWC and QAIC may be quite significant. This has significant energy consumption and sensitivity implications. Therefore, these features of the low-pass CS architectures make it a more suitable solution for baseband applications, while the band-pass CS architectures offer lower energy consumption and better sensitivity compared to the low-pass CS architectures especially at RF frequencies.

The total number of branches m_{CS} needed by the MWC, QAIC for successful signal recovery is proportional to the number of observed supports multiplied by a logarithmic factor and constants $C_{MWC} \geq 1$, $C_{QAIC} \geq 1$. $m_{CS} \propto 2K_0$ branches are required by the MWC [42]. Due to its complex

I, Q structure the QAIC requires $m_{QAIC} \propto K_0$ in-phase and quadrature-phase branches. The QAIC therefore employs $m_{CS} = 2m_{QAIC}$ total branches. The required sampling rate per branch for both systems is $f_s \geq RBW$ Hz. The aggregate sampling rate of each system is $m_{CS} \cdot f_s$. It should be noted that the number of branches m_{CS} may be traded, can be reduced by a factor q, where $q \in \mathbb{Z}^+$ ($q > 1$), for the branch sampling rate f_s, while maintaining the same aggregate sampling rate as shown in Table 4.1.

The MWC and QAIC system design parameters are summarized in Table 4.1. The required number of branches for MWC and QAIC is provided to sense a 1GHz of spectrum ranging from 2.7 to 3.7GHz with a RBW of 20MHz. The estimated constants for MWC and QAIC are $C_{MWC} = 2.96$ and $C_{QAIC} = 2$ respectively [4]. Since the QAIC observes only the bins in the frequency range of interest, it requires significantly fewer branches, 8 complex I/Q branches (16 physical branches) vs 29 branches, for a 1GHz span with a 20MHz RBW. Reduced number of branches of a QAIC thus allows a smaller aggregate sampling rate, up to 1.8 times less than MWC and 6.3 times less than traditional Nyquist-rate architectures [3, 4].

The effective noise bandwidth to account for the noise folding tracks the instantaneous bandwidth of the QAIC and is defined by $L \cdot RBW$ which scales with the span. To half the RBW for a given span, L needs to double; the effective noise folding then remains the same; in essence the impact of noise folding will not reduce when reducing RBW but only when reducing the span. The smaller signal bandwidth after downconversion results in a reduced noise folding and thus an improved sensitivity of the QAIC by $10\log(511/63)$ or 9.1dB that is proportional to the ratio of

Table 4.1: *Design parameters for compressed-sampling spectrum sensors with a design example for a 2.7 to 3.7GHz sensor with a 20MHz RBW*

System Parameters		MWC based spectrum sensor		QAIC	
I/Q Downconverter LO Frequency	f_{lo}	N/A	N/A	$(f_{max}+f_{min})/2$	3.2GHz
3-dB RF I/Q BW	$f_{3dB\text{-}RF}$	N/A	N/A	$(f_{max}-f_{min})/2$	500MHz
Number of branches	m_{CS}	$\lceil 2K_0.C_{MWC}.\log(L/4K_0)/q \rceil$	29	$2\lceil K_0.C_{QAIC}.\log(L/K_0)/q \rceil$	16
Length of the PN Sequences	L	$(2^n\text{-}1)\geq 2N_0$	511	$(2^n\text{-}1)\geq N_0$	63
PN Sequence Generator Clock Frequency	f_{CLK}	$L.RBW\geq 2f_{max}$	10.22GHz	$L.RBW\geq(f_{max}-f_{min})$	1.26GHz
Aggregate Sampling Rate	$m_{CS}.f_s$	$\geq q.m_{CS}.RBW$	580MSps	$\geq q.m_{CS}.RBW$	320MSps

N/A = Not Applicable

the length of the PN sequences [3, 4]. These advantages lead to significant energy efficiency and sensitivity improvements as demonstrated in Section 4.6.

4.2.2 Key Performance Metrics of the Band-pass Compressed Sampling Spectrum Sensors with a QAIC

For a QAIC based spectrum sensor, the scan time is set by the front-end detector response time $T_{resp,QAIC}$ and recovery time $T_{rec,QAIC}$ (4.13). Energy consumption is given by:

$$E_{QAIC} = P_{QAIC} \cdot [T_{resp,QAIC} + T_{rec,QAIC}] = P_{QAIC} \cdot [(C_{settle}/BW_{filter}) + (N_s/f_s)] = P_{QAIC} \cdot T_{scan}. \tag{4.13}$$

To sense a 1GHz of span ranging from 2.7 to 3.7GHz, the QAIC based spectrum sensor offers 50 times faster scan time compared to the sweeping spectrum scanners, while 6.3 times compression in the aggregate sampling rate compared to multi-branch spectrum sensors and Nyquist-rate FFT spectrum scanners. The QAIC based spectrum sensor furthermore offers 6.3 times compression in the number of branches compared to multi-branch spectrum sensors that require 50 I/Q

branches in parallel to sense a 1GHz span with a 20MHz RBW. While keeping the scan time short, the power consumption of a QAIC based spectrum sensor, P_{QAIC}, is reduced compared to an MWC based spectrum sensor by an order of magnitude proportional to the reduction of the rate and length of PN sequences thanks to architectural changes. With these reductions in the power consumption and the scan time, QAIC offers potentially two orders of magnitude reduction in the energy consumption compared to traditional spectrum scanner and sensor architectures.

The QAIC based spectrum sensor further offers a 1GHz-wide instantaneous bandwidth as a key performance metric compared to the traditional sweeping spectrum scanners that have a smaller instantaneous bandwidth equal to their RBW. There is a fixed trade-off between the instantaneous bandwidth and the instantaneous dynamic range. This relationship between the instantaneous bandwidth and the instantaneous dynamic range for analog-to-information converters (AICs) and the system design parameters that have an impact on the instantaneous dynamic range especially for QAIC and TS-QAIC systems are explained in detail in Chapter 6.

In addition to the high energy efficiency, short scan time and wide instantaneous bandwidth, the QAIC is a highly scalable system. The QAIC scalability is demonstrated in terms of varying ADC resolutions and the number of parallel branches in Section 4.4.5.

4.3 Implementation of Rapid Interferer Detector Using a QAIC

4.3.1 Architecture of the Rapid Interferer Detector Using a QAIC

The block diagram of the band-pass CS rapid interferer detector system employing a QAIC is shown in Fig. 4.5. The system controller configures the QAIC hardware and software resources according to user specified system constants and performance targets such as RBW, sensitivity, maximum and minimum frequencies of interest, f_{max} and f_{min}, P_D and P_{FA}. The implementation details of the QAIC chip are presented in Section 4.3.2 with RF front-end circuit details and Section 4.3.3 with baseband circuit consists of PN sequence generation details, while the CS DSP is discussed in Section 4.3.4.

4.3.2 Circuit Implementation of the CS QAIC RF Front-End Blocks

The 2.7-3.7GHz QAIC prototype circuit implementation is shown in Fig. 4.6. It implements the functions in the shaded box in the band-pass CS interferer detector system diagram in Fig. 4.5. The chip has been implemented in a 65nm CMOS GP technology.

The QAIC chip uses a wideband noise-canceling low-noise amplifier (LNA) [50, 51]. A wideband noise-canceling LNA is preferred since impedance matching is required for a wide instantaneous bandwidth of 1GHz. The post-layout simulated LNA gain for typical process corner is 15.8dB to 14.6dB from 2.7 to 3.7GHz and the simulated $S_{11} < -10dB$ for a wide bandwidth from 1 to 3.7GHz for typical process corner. The measured LNA power consumption is 14mW from a 1.1V supply.

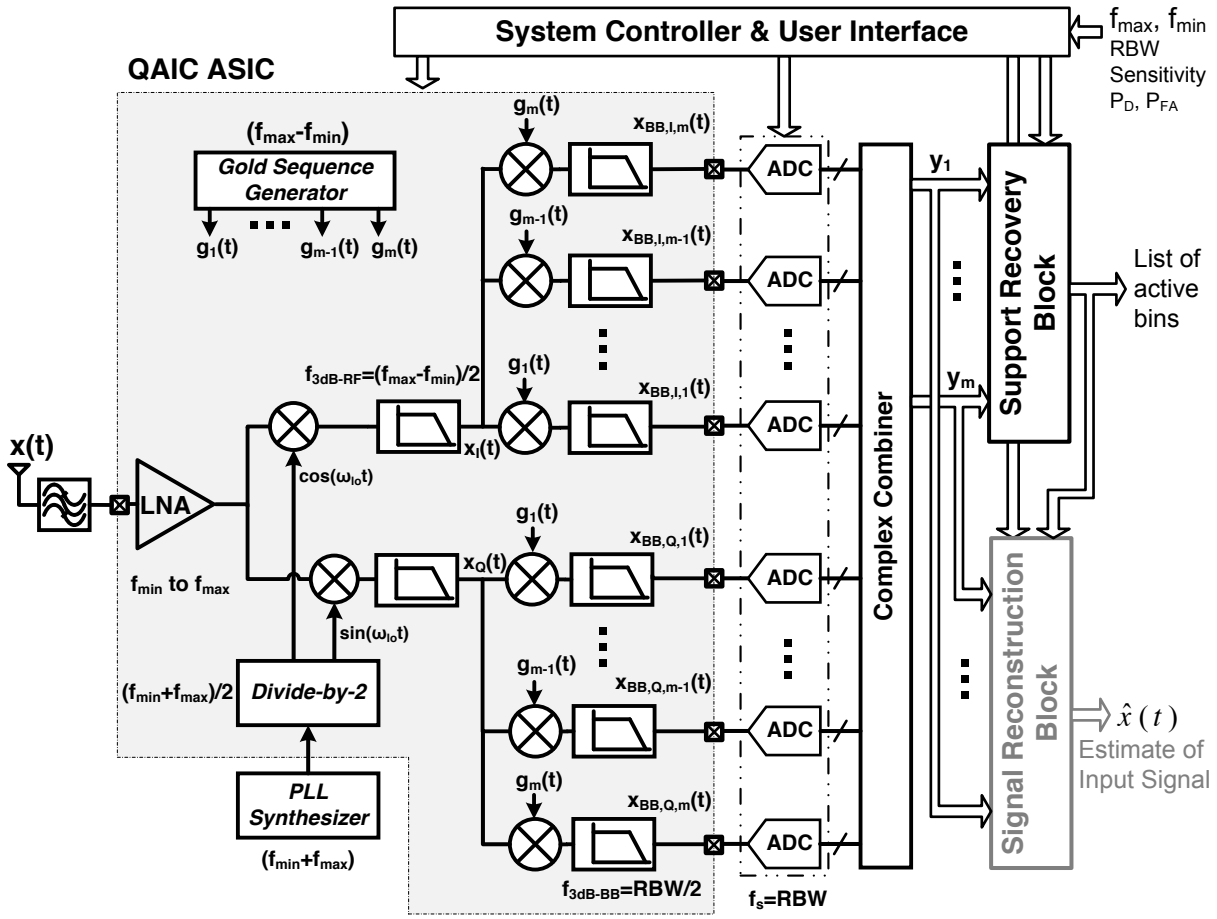

Figure 4.5: *Block diagram of the rapid interferer detector based on band-pass compressed sampling with a QAIC.*

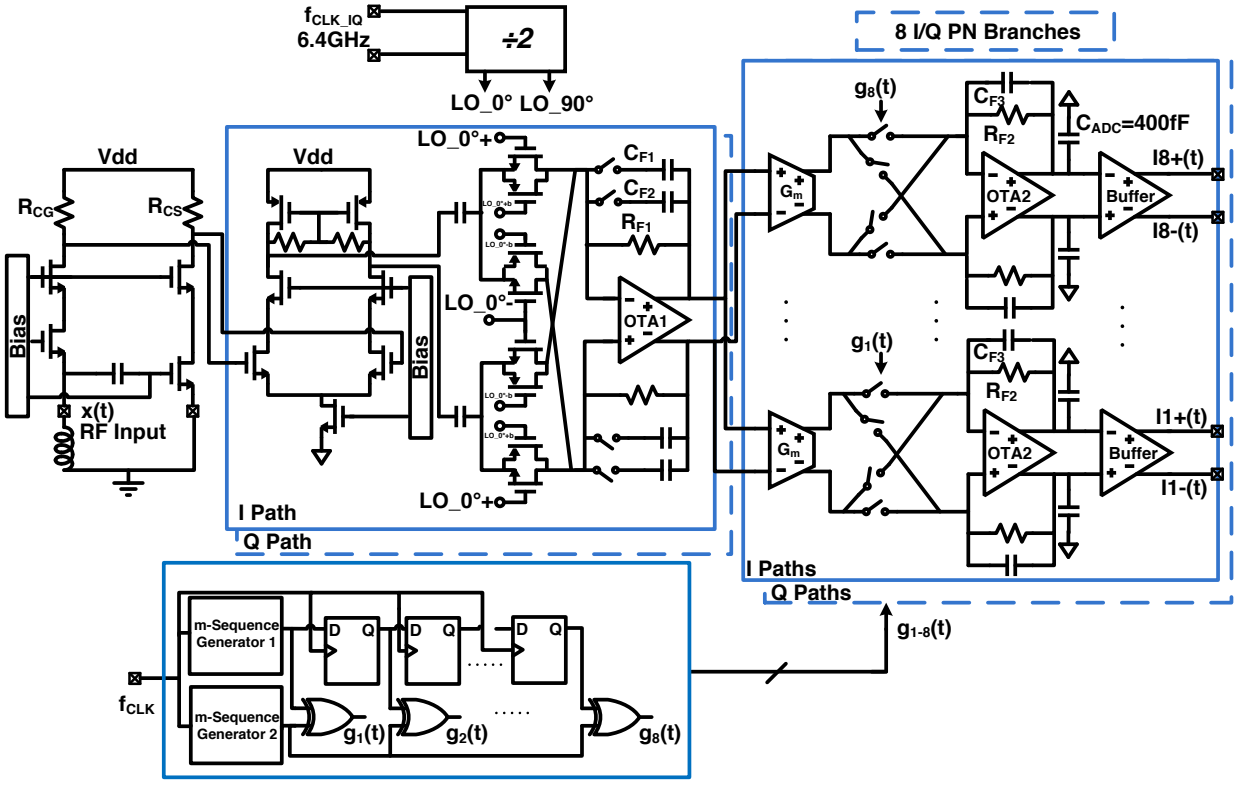

Figure 4.6: *Circuit implementation details of the QAIC front end.*

The LNA is followed by current-driven passive I/Q mixers and transimpedance amplifiers (TIAs) [52–54]. The input stage is implemented as a transconductance G_m amplifier operating at an RF frequency range 2.7 to 3.7GHz followed by four pairs of CMOS transmission gate switches driven by complementary clock phases at 3.2GHz. An off-chip RF clock fed to the chip is 6.4GHz and 3.2GHz quadrature LO signals with a 50% duty cycle driving the RF I/Q downconverter mixers, $\cos(\omega_{lo}t)$ and $\sin(\omega_{lo}t)$, are generated by the on-chip divide-by-2 circuit that is followed by clock buffers and a non overlap generator that is formed by two cross-coupled NAND gates with inverter chains to generate complementary phase clocks for transmission gate type passive mixer switches. The downconverted current signal is converted into a voltage output by a transimpedance amplifier that is configured as an RF I/Q filter. Single stage OTA topology [55] is chosen for RF I/Q filter design since it was critical to achieve a wide 500MHz bandwidth while driving the 8 I/Q PN paths and minimizing the power consumption. Measured power consumption of the RF I/Q downconversion stage including the current-driven passive I/Q mixers, TIA based filters and I/Q LO generation based on divide-by-2 circuitry is 20.9mW from a 1.1V supply.

4.3.3 PN Sequence Generation and CS Baseband Circuits

The RF TIAs drive eight I/Q PN paths, each with a current-driven passive mixer and TIA used as a baseband filter loaded with 400fF, C_{ADC} in Fig. 4.6, emulating the equivalent load of an 8-bit ADC. Measured power consumption of the 8 I/Q PN branches is 38.9mW from a 1.1V supply.

I/Q PN mixing stages are driven by 8 unique gold sequences [47, 56] generated on-chip with a gold sequence generator. Gold sequences are preferred because a large set of periodic sequences

with good cross-correlation and autocorrelation properties can be generated with less circuitry compared to a shift register implementation [47]. Gold sequences generated from preferred m-sequence pairs satisfy the following inequalities in (4.14) for cross-correlation, θ [47, 56]:

$$|\theta| \leq t = 2^{(n+2)/2} + 1, \; n \; even$$
$$|\theta| \leq t = 2^{(n+1)/2} + 1, \; n \; odd. \tag{4.14}$$

The on-chip gold sequence generator shown in Fig. 4.7 has various length options of 15, 31, 63 and 127 for programmable RBW options. The switches $C0$, $C0_b$, $C4$, $C4_b$, $C5$, $C6$ and $C7$ shown in Fig. 4.7(a) are used to control the length of the gold sequences by changing the length of the m-sequences. It generates 8 ($2^n - 1$) long gold sequences by XORing two m-sequences generated by two n-flip-flop LFSRs. By keeping one m-sequence shown in Fig. 4.7(a) the same and delaying the other one before the XOR, up to $2^n - 1$ distinct gold sequences can be generated with sufficiently low cross-correlation as shown in Fig. 4.7(b).

Fig. 4.8(a) shows the autocorrelation and cross-correlation properties of one of the 8 unique gold sequences for a length of 63 which satisfy the sequence requirements i.e. θ. Fig. 4.8(b) shows the measured input referred conversion gain from 2.7 to 3.7GHz of the 8 PN I/Q mixing stages driven by 8 unique gold sequences for a RBW of 20MHz. Some of the implemented gold sequences are balanced while others are unbalanced. Balanced gold sequences have better spectral properties (i.e. are more evenly distributed) [57]. Also 8 unique m-sequences that are known to have uniform (evenly distributed) spectrum can be used in future work to overcome the conversion

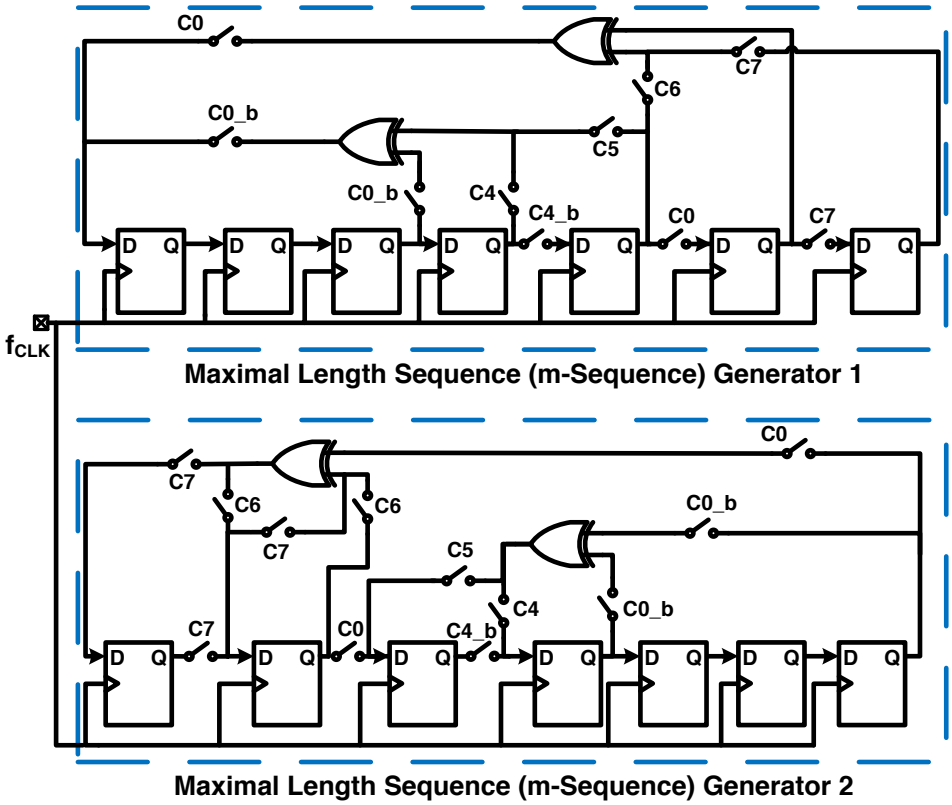

	C0	C0_b	C4	C4_b	C5	C6	C7
L=15	Open	Closed	Closed	Open	Open	Open	Open
L=31	Open	Closed	Open	Closed	Closed	Open	Open
L=63	Closed	Open	Open	Closed	Open	Closed	Open
L=127	Closed	Open	Open	Closed	Open	Open	Closed

(a)

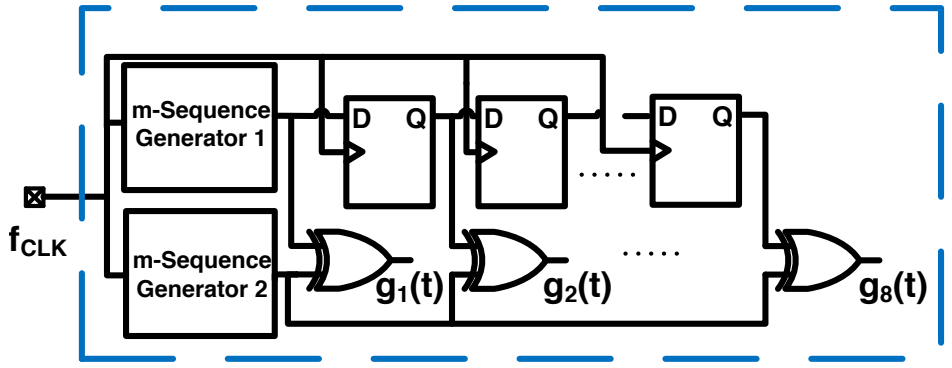

(b)

Figure 4.7: *Circuit implementation details of gold sequence generator for 8 unique gold sequences with low cross-correlation operating at 1.26GHz for length 15, 31, 63 and 127; (a) Two unique m-sequence generators based on an LFSR implementation (b) 8 unique gold sequences generation based on the two unique m-sequences with RBW programmability.*

gain fluctuations over frequency. Measured power consumption of the on-chip gold sequence generator for the nominal length of 63 is 7.04mW from a 1.1V supply.

4.3.4 CS Digital Signal Processing

The Orthogonal Matching Pursuit (OMP) algorithm is used to identify the input bands that exceed a user-defined threshold. The OMP is a simple greedy heuristic for sparse recovery, which forms an estimate of the signal support one element at a time. It offers an attractive trade-off between algorithm simplicity and recovery guarantees [58,59]. The OMP stopping criterion is derived from the system dimension and a user-defined threshold. This threshold can be set to optimize P_D or P_{FA}. In this work, the threshold is set close to the QAIC noise floor to maximize P_D performance of the system. Note that while the main focus of this work is support or interferer spectral location discovery, simple signal estimation has been performed for results included in Section 4.4.2. This is accomplished by applying the pseudo-inverse of the reduced (or indexed) measurement matrix to the QAIC complex samples.

If a particular band of a multi-band signal does not nicely fall into a grid consisting of 10MHz or 20MHz RBW-wide bins, for example part of it false in one bin and a part of it in the next bin, the CS support recovery algorithm will indicate that 2 adjacent bins are occupied.

CS DSP Energy Estimation for a Complex-Domain Support Recovery: For m_{QAIC} the number of complex branches, L the length of the gold sequence employed by the QAIC, to a first order, $m_{QAIC} \cdot L$ complex multiplications and additions are needed to complete a single iteration of the OMP for a complex-domain support recovery. For a single set of measurements, K_0 iterations are

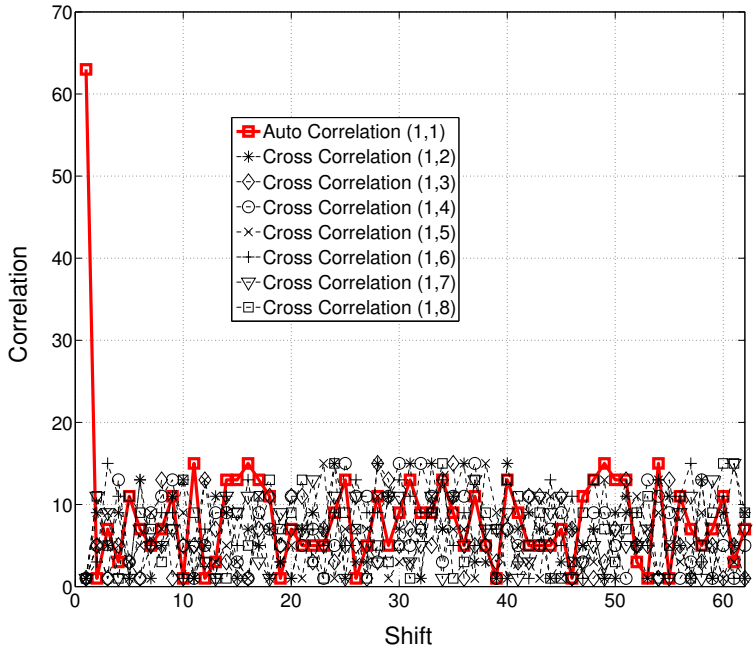

(a)

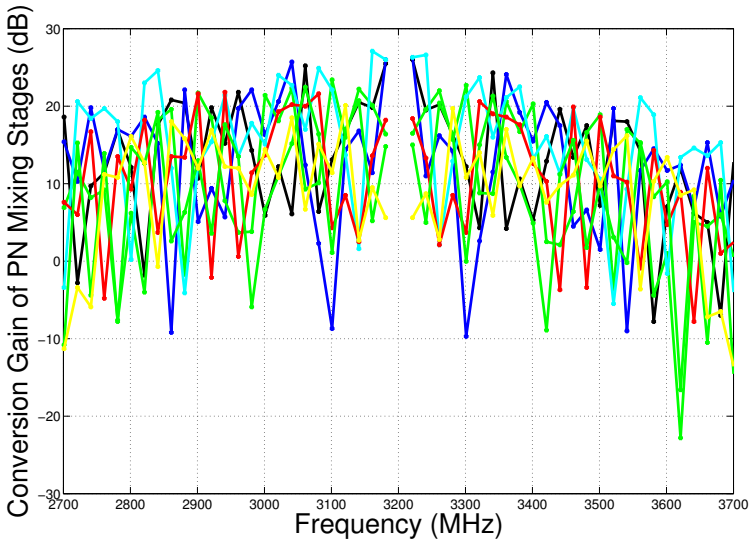

(b)

Figure 4.8: *Properties of the 8 unique gold sequences generated on chip; (a) Autocorrelation and cross-correlation properties of one of the 8 gold sequences is shown for a shift of 63 for a length 63; (b) Input referred conversion gain from 2.7 to 3.7GHz of the 8 PN mixing stages driven by the 8 gold sequences for a length of 63, and RBW of 20MHz.*

required with an ADC sampling period of T_s, the time required to complete a single iteration is $T_{iteration} = T_s/K_0$. Therefore, the energy consumption of a single iteration is given by (4.15), where P_{adder} and P_{multi} are the power consumption of adders and multipliers respectively.

$$E_{iteration} = m_{QAIC} \cdot L \cdot (P_{adder} + P_{mult}) \cdot T_{iteration} \tag{4.15}$$

If n_s consecutive samples from the QAIC are used for a complex-domain support recovery to detect K_0 active bins, then the total number of complex multiplications and additions needed by the OMP is roughly $n_s \cdot K_0 \cdot m_{QAIC} \cdot L$. To a first order, the total energy consumption of the OMP for a complex domain support recovery is given by (4.16).

$$E_{OMP} = m_{QAIC} \cdot L \cdot (P_{adder} + P_{mult}) \cdot T_s \cdot n_s \tag{4.16}$$

Assuming n_s = 80, m_{QAIC} = 8, L = 63 and K_0 = 3, for real multiplications and additions, the computational load of the OMP is found to be roughly $535nJ$. Here we assume that an 16x16 multiplier and an 16-bit adder with a settling time less than $17ns$ consume $60\mu W$ and $5\mu W$ respectively [60, 61].

4.4 Band-pass CS QAIC Measurement Methods and Results

4.4.1 Measurement Setup of the Band-pass CS Interferer Detector Using a QAIC

The QAIC prototype chip shown in Fig. 4.9 has an active area of $0.428mm^2$ in 65nm CMOS [3,5]. Measured power consumption of the QAIC chip in a 64-pin QFN package is 81mW from a 1.1V supply with the power consumption breakdown as shown in Fig. 4.10. Fig. 4.11 shows the system measurement setup of the band-pass CS rapid interferer detector with a QAIC. Multi-band RF input signals are generated by upconverting band-limited noise. RF input signal combinations are fed into the QAIC chip and the outputs are digitized by using 8-bit oscilloscopes at a rate of 20MSps and captured for off-line CS complex-domain support recovery.

4.4.2 QAIC Instantaneous Bandwidth and Programmable Resolution Bandwidth Demonstration

The wideband sensing capability of the band-pass CS interferer detector for a 1GHz wideband spectrum ranging from 2.7 to 3.7GHz is demonstrated in Fig. 4.12. Three -37dBm/10MHz band-limited upconverted noise signals at 2.76GHz, 3.54GHz, 3.58GHz are presented to the QAIC and their locations are correctly recovered.

The QAIC RBW programmability is demonstrated in Fig. 4.13. The QAIC RBW is changed from 20MHz to 10MHz by switching the length of the gold sequences from 63 to 127. The solid curves and the dashed curves are the input three band signal spectrum and the reconstructed signal

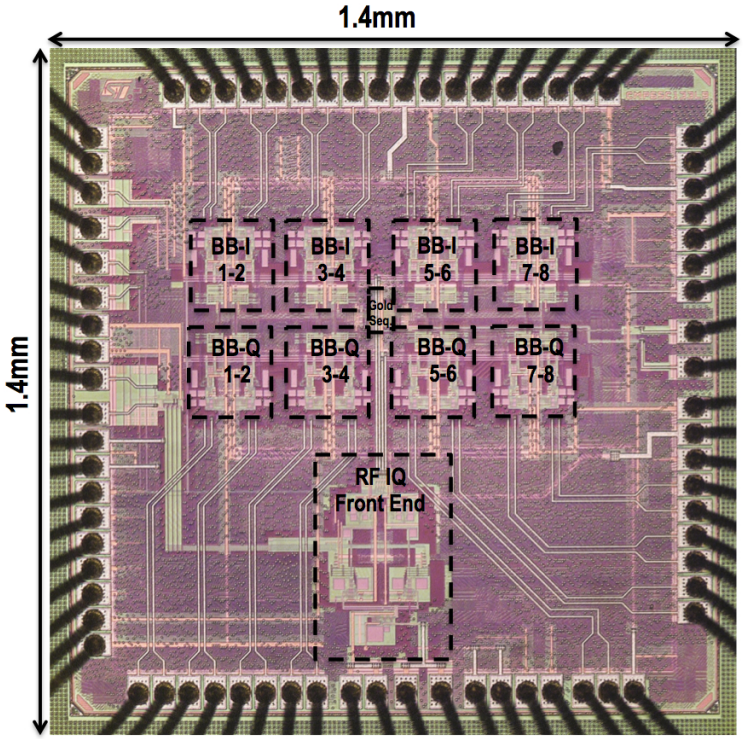

Figure 4.9: *Die photograph of the 65nm QAIC prototype*

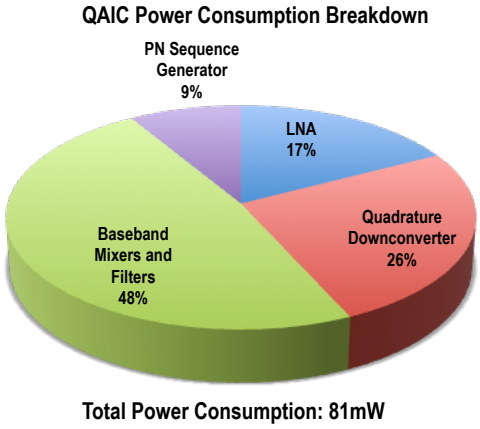

Figure 4.10: *Measured power consumption breakdown of the QAIC chip.*

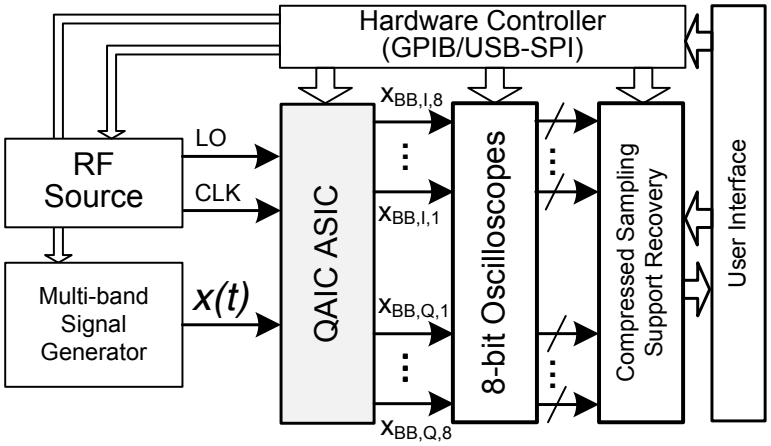

Figure 4.11: *Measurement setup for the rapid interferer detector system based on band-pass compressed sampling with a QAIC.*

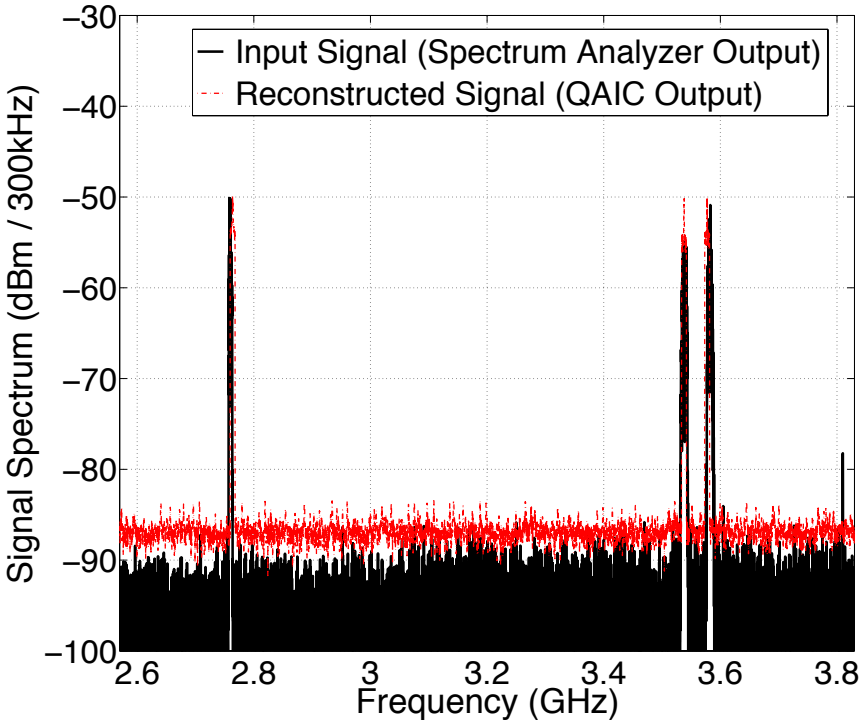

Figure 4.12: *QAIC 1GHz wideband sensing capability; demonstrated with the detection of three -37dBm/10MHz bands located between 2.7 to 3.7GHz; the solid curve and the dashed curve are the input spectrum and the reconstructed spectrum respectively.*

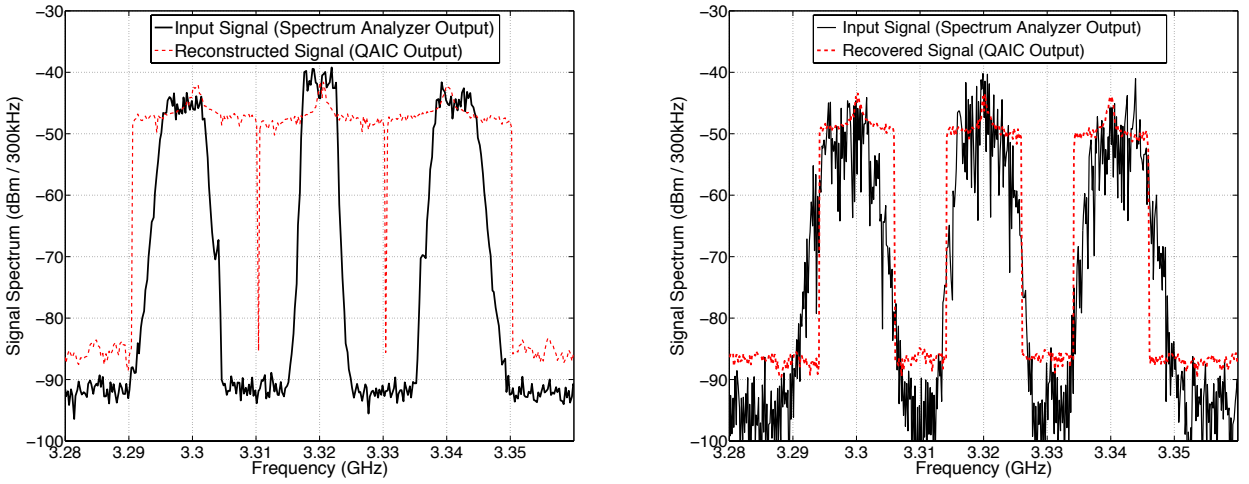

(a) (b)

Figure 4.13: *QAIC RBW programmability; 20MHz and 10MHz respectively by changing the gold sequence length from 63 to 127; the solid curves and the dashed curves are the input three band signal spectrum and the reconstructed signal spectrum respectively; (a) middle band centered at 3.32GHz is -30dBm/10MHz and side bands centered at 3.3GHz and 3.34GHz are -33dBm/10MHz; (b) middle band centered at 3.32GHz is -37dBm/10MHz and side bands centered at 3.3GHz and 3.34GHz are -40dBm/10MHz; 10MHz spectrum gaps in between are detected.*

spectrum respectively. Input signal consists of three 10MHz bands. In Fig. 4.13(a), the middle band centered at 3.32GHz is -30dBm/10MHz and the side bands centered at 3.3GHz and 3.34GHz are -33dBm/10MHz. The input signal spectrum is first recovered with a 20MHz QAIC RBW; the three interferers are located in the adjacent bins. In Fig. 4.13(b), the middle band centered at 3.32GHz is -37dBm/10MHz and the side bands centered at 3.3GHz and 3.34GHz are -40dBm/10MHz. The QAIC RBW is changed to 10MHz and the 10MHz spectrum gaps between the signals are correctly detected.

4.4.3 QAIC Time Agility Demonstration

The time agility of the QAIC is demonstrated with a measurement of $T_{resp,QAIC}$ in Fig. 4.14. The input signal is shown in the 3D plot, the top plot of Fig. 4.14, with time, frequency and power level axes. The input signal spectrum is switched from a -42dBm single tone with a 250kHz-offset-from-bin-center shown as the dashed curve to the same -42dBm tone with two additional -58dBm 10MHz band-limited upconverted noise signals shown as the solid curve. The QAIC baseband output signal is captured with a scope. The QAIC baseband output signal as shown in the bottom plot of Fig. 4.14 changes from a single tone to noise with a tone. The band-pass CS rapid interferer detector uses blind algorithms to locate the signals that are unknown interferers to the detector. The signal support change command is used to trigger the input signal source to control the input test spectrum. This trigger signal is also observed and is going from low to high at the instant the input spectrum is changed. This measurement shows that QAIC baseband output responds to the change in the input spectrum within $0.4\mu s$. This response time is limited by settling of the 10MHz anti-aliasing filter. In addition to the detector response, $T_{resp,QAIC}$, the support recovery time, $T_{rec,QAIC}$, contributes to the total scan time of the interferer detector system as given by (4.13). Robust support recovery requires 80 samples (i.e. $N_s = 80$) so that a scan time of $4.4\mu s$ can be guaranteed with 20MSps ADCs. For the same settings, traditional approaches require $220\mu s$ scan time proportional to N_0 (i.e. $N_0 = 50$) as given by (2.2). Therefore, the QAIC is far superior to traditional spectrum scanning approaches, allowing for energy savings and fast tracking of dynamically changing interferers in a wideband spectrum.

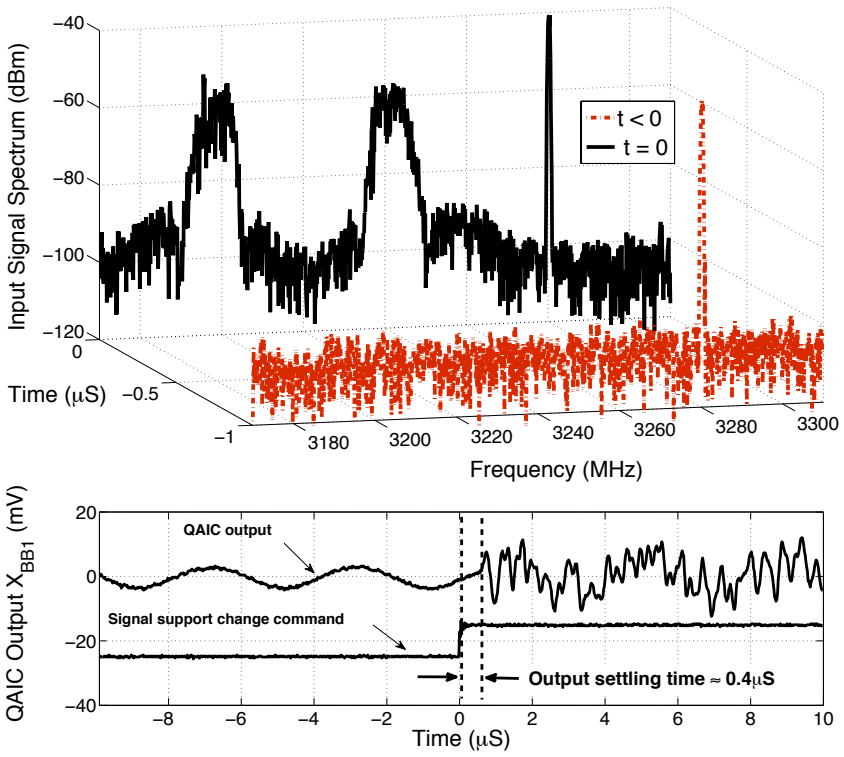

Figure 4.14: *Time agility of QAIC detector; the detector baseband response to a change of the input spectrum from a -42dBm single tone with a 250kHz-offset-from-bin-center (dashed curve) to a tone with two -58dBm 10MHz bands (solid curve) is 0.4μs.*

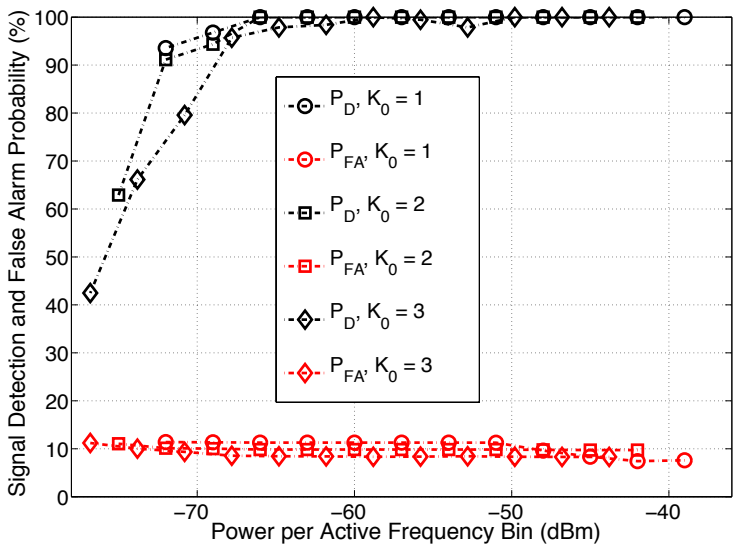

Figure 4.15: *Demonstration of the QAIC sensitivity in terms of detection probability, P_D, and false alarm probability, P_{FA}, for active supports K_0=1,2 and 3 by varying signal power level per active frequency bin based on 80 samples for recovery and 125 experiments per power level; detection probability$\geq$ 90% and false alarm probability$\leq$ 15% is satisfied for as small as -68dBm three equal power supports.*

4.4.4 QAIC Sensitivity Demonstration

Detection and false alarm probabilities, P_D and P_{FA}, are used to evaluate the performance of the band-pass CS rapid interferer detector system with a QAIC. P_D and P_{FA} are reported based on the correct detections (CD) and the false alarms (FA) from 125 experiments (number of experiments, N_E) per power level setting with:

$$P_D = \frac{\sum CD}{N_E \cdot K_0} \text{ and } P_{FA} = \frac{\sum FA}{N_E \cdot (L - K_0)} \tag{4.17}$$

Fig. 4.15 demonstrates the sensitivity of the band-pass CS rapid interferer detector in terms of P_D and P_{FA} as a function of support (a.k.a. active bin) power. The cluster of curves on the top

correspond to P_D and the cluster of curves on the bottom correspond to P_{FA} for 3 measurements with 1,2 and 3 equal power interferers. Three equal power interferers as small as -68dBm can be detected with a P_D better than 90%, whereas a single interferer as small as -72dBm can be detected with the same P_D. We note that 80 samples are used to achieve these sensitivity levels. Results in Fig. 4.16(b) with 160 samples and 8 I/Q branches demonstrate that doubling the number of samples improves the sensitivity by 3dB. The effect of number of samples on the sensitivity level is explained in detail in Chapter 6.

The P_{FA} is below 15% for all measurements. Note that P_{FA} depends on two main factors: the user-defined threshold and the stopping criterion proportional to the dimension of the measurement matrix. The maximum P_{FA} for the QAIC is m_{QAIC}/L or $(8/63)\%$ in this work. When the threshold is set close to the noise floor, P_{FA} remains roughly constant and P_D is maximized.

4.4.5 QAIC Scalability and Robustness to Support Overload Demonstration

The QAIC scalability is demonstrated along three of its axes; number of branches, samples per branch and the number of bits employed in the ADCs in Fig. 4.16. Measured P_D and P_{FA} are used to illustrate the QAIC performance along these axes. Below a number of examples is given on how this flexibility can be used during the design or operation of a band-pass CS interferer detector with a QAIC.

The QAIC can operate with varying ADC resolutions. Assuming a performance of $P_D > 90\%$ and $P_{FA} < 15\%$ and an RF input spectrum consisting of 2 active interferers, a QAIC using 8 complex I/Q branches with 8-bit ADCs can detect -72dBm supports with 160 samples while the same

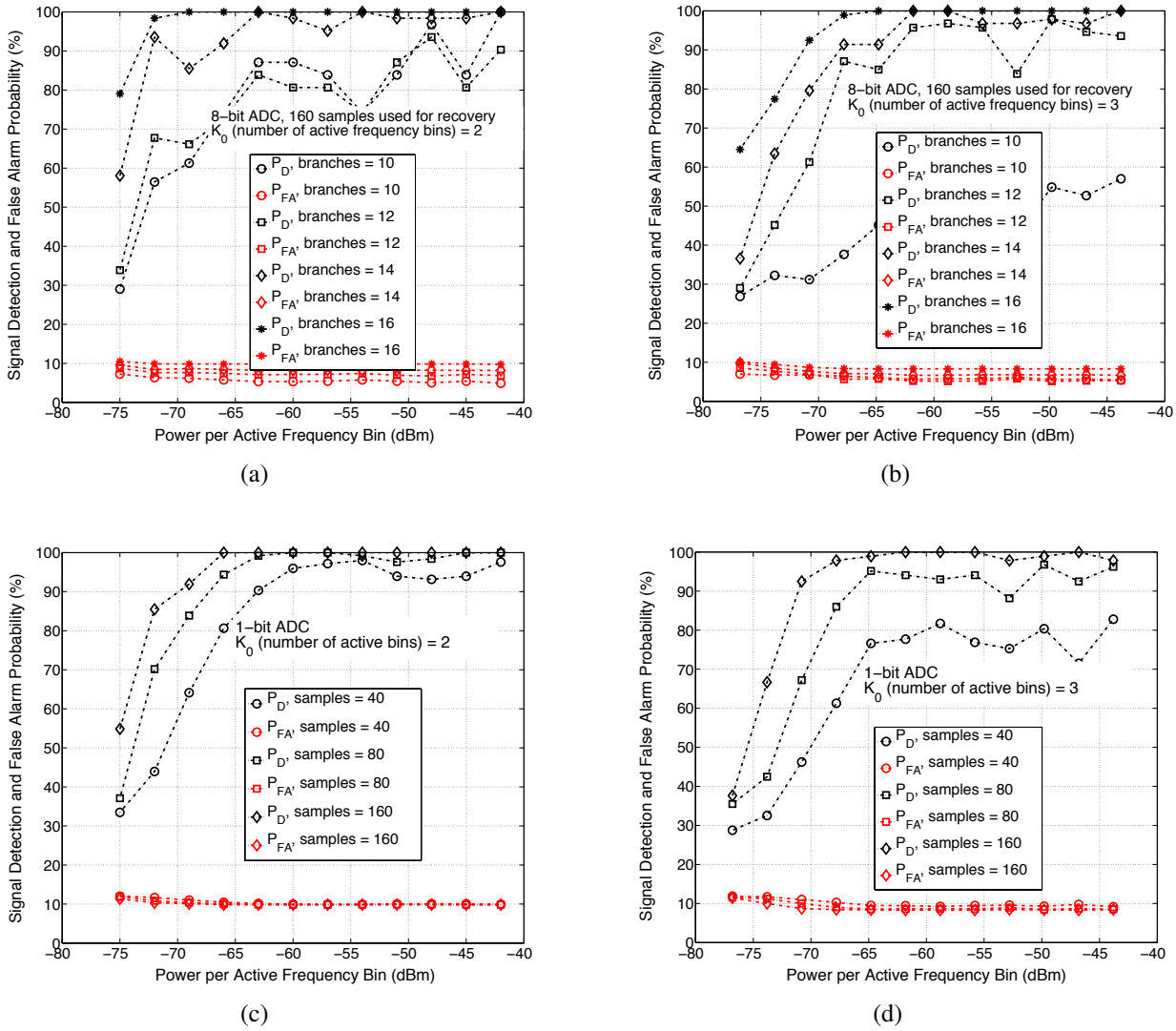

Figure 4.16: *QAIC scalability is demonstrated in terms of number of branches, samples per branch and ADC resolution in terms of detection probability, P_D, and false alarm probability, P_{FA} for K_0=2 and 3 by varying signal power level per active frequency bin based on 125 experiments per power level. To demonstrate the QAIC scalability and robustness to support overload; (a) Number of branches are scaled from 16 = 8 x I/Q branches to 10 = 5 x I/Q branches for K_0=2 with an 8-bit ADC and 160 samples for recovery, (b) Number of branches are scaled from 16 = 8 x I/Q branches to 10 = 5 x I/Q branches for K_0=3 with an 8-bit ADC and 160 samples for recovery, (c) Number of samples per branch is scaled from 40 to 160 samples and ADC resolution is scaled from 8-bit to 1-bit for K_0=2, (d) Number of samples per branch is scaled from 40 to 160 samples and ADC resolution is scaled from 8-bit to 1-bit for K_0=3.*

QAIC employing 1-bit ADCs can detect -68dBm with 160 samples as shown in Fig. 4.16(c). The DSP for a 1-bit QAIC will consume significantly less energy compared to its 8-bit counterpart. Note that the 1-bit QAIC will deliver a lower dynamic range compared to its 8-bit counterpart. This trade-off between energy consumption and dynamic range may be useful for many real world applications.

The QAIC robustness to support overload is also demonstrated in Fig. 4.16(a) and Fig. 4.16(b). Due to measurement setup limitations we could not increase the number of active interferers beyond three during the QAIC prototype testing, but the support overload phenomenon is emulated by keeping the number of active interferers fixed and reducing the number of branches used in the QAIC. In the experiments reported in Fig. 4.16(b), we present the QAIC with an RF input spectrum with 3 active interferers. Theory predicts that 8 I/Q branches are required to deliver robust recovery (3.1) [3, 4]. See Table 4.1 for the details. However, the results demonstrate, that even with 6 I/Q branches the P_D and P_{FA} remain at practically usable levels. With 5 I/Q branches the P_D and P_{FA} degrades drastically since the 5 I/Q branches are lower than the theoretical limit for the required branches.

Since we can only commit to a fixed number of branches in silicon, adaptive configurability and scalability is indispensable in real world applications. A possible adaptive action in response to support overload is to relax the recovery algorithms sensitivity threshold. In essence this makes the QAIC blind to lower power bins and effectively sparsifies the spectrum. Only interferers above the new threshold are detected with high confidence. Next, programmable notch filters can be deployed to filter these interferers from the detector input and a new scan can be performed with

a lower threshold to detect more interferers if needed. To detect twice the number of interferers compared to a QAIC with only 8 physical I/Q branches, without needing to double the amount of hardware as needed in a QAIC, we used time segmentation to virtually extend the physical hardware and the details of the time-segmented QAIC are discussed in Chapter 5.

It can be further noted that the QAIC architecture can be reconfigured as a Nyquist-rate receiver by disabling the PN mixing and by time-interleaving the ADCs of the 8 complex branches operating at an aggregate sampling rate of 320MSps with higher sensitivity.

4.4.6 QAIC Instantaneous Dynamic Range Demonstration

The instantaneous dynamic range (DR) performance of the QAIC system is illustrated in Fig. 4.17 for one weak and two strong interferers that are present over the interest spectrum range of the QAIC at the same time. The instantaneous DR of a QAIC system designed to handle K_0 interferers is defined as the maximum power difference between $k < K_0$ weak interferers and $(K_0 - k)$ strong interferers over a wide instantaneous bandwidth (IBW) that the system can handle in the presence of linear impairments, nonlinear distortion and noise while delivering a desired P_D, P_{FA} performance level [3,4]. For the results presented in Fig. 4.17, only linear impairments, i.e. down-converter gain and phase imbalance, are compensated. A calibration based compensation approach is adopted. A single tone offset by 1MHz from the center of the weak interferer frequency bin is used as the calibration signal. The estimated IQ imbalance level is then entered into the QAIC system matrix defined in Section 4.2. The information recovery engine uses this updated system

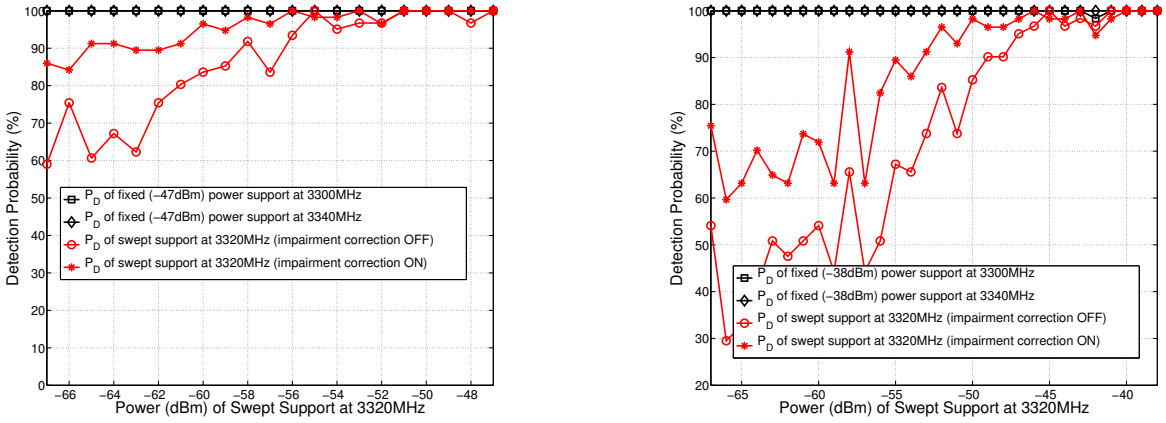

(a) (b)

Figure 4.17: *Detection probability P_D of a weak signal in the presence of two strong signals is demonstrated for various power levels based on 80 samples for recovery and 125 experiments per power level; (a) 2 band power fixed at -47dBm per active frequency bin and 1 band with varying power levels with/without linear impairments correction, (b) 2 band power fixed at -38dBm per active frequency bin and 1 band with varying power levels with/without linear impairments correction.*

matrix to deliver improved DR performance as illustrated in Fig. 4.17. See Section 4.2 for details of the QAIC system impairment model [4].

In Fig. 4.17(a), the two strong interferers are fixed at a moderate power level while the power of the weak interferer is swept. It is seen that the QAIC system without impairment compensation is able to detect a weak interferer at a power level as low as -58dBm with a 90% confidence level in the presence of two strong interferers fixed at a power level of -47dBm. Therefore, the uncompensated QAIC system delivers 11dB of dynamic range. Fig. 4.17(a) also demonstrates that the QAIC system is able to deliver 18dB of dynamic range when impairment compensation is activated. Fig. 4.17(b) demonstrates the QAIC system DR performance with and without impairment compensation for a scenario where the power of the two strong interferers is set to a higher level, -38 dBm for this experiment.

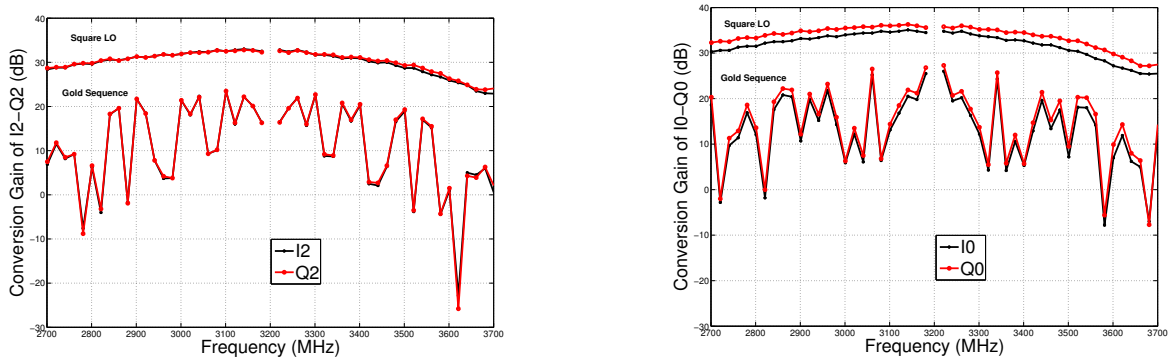

(a) (b)

Figure 4.18: *(a) Input referred conversion gain from 2.7 to 3.7GHz for square LO and unique gold sequences for a RBW of 20MHz; (a) I2-Q2 pair, (b) I0-Q0 pair.*

4.4.7 Conversion Gain of QAIC for Square LO and Gold Sequence

The QAIC branches are characterized for RF performance with square LOs driving the PN I/Q mixers in a test mode. Typical QAIC chain gain is 35dB with a 14dB NF. The QAIC is also characterized for the nominal setting of the rapid interferer detector in CS mode with 8 unique gold sequences driving the PN I/Q mixers. Fig. 4.18 shows the conversion gain of two I/Q branches, i.e. the I2-Q2 pair as shown in Fig. 4.18(a) and I0-Q0 pair as shown in Fig. 4.18(b), from 2.7 to 3.7GHz with a RBW of 20MHz, when the baseband PN I/Q mixers are driven by square LOs and unique gold sequences.

The theoretical conversion loss of uniformly distributed and spectrally diverse m-sequence is proportional to the length of the sequence [47]. For a 63-long m-sequence with a RBW of 20MHz, the conversion loss is 17.99dB due to the spreading effect of mixing with the PN sequences. Compared to mixing with a square LO that has a fundamental tone of $2/\pi$, 14dB of conversion loss is expected with a sinc shape frequency spectrum. Since the gold sequences are not uniformly dis-

tributed, it is observed in Fig. 4.18 that some bins have more energy than the others depending on the gold sequences driving the PN I/Q mixing stages and the typical maximum QAIC conversion gain is reduced to 24dB for the I2-Q2 pair and 27dB for the I0-Q0 pair. Since the PN mixer is the key block of AICs that allows us to capture the wide instantaneous bandwidth, the effects of the PN sequence spectral properties on analog-to-information converter performance are discussed more in detail in Chapter 6.

4.5 Demo System of the Rapid Interferer Detector with a QAIC from Stimulus to Compressed Sampling Digital Signal Processing

Fig. 4.19 shows the system demonstration setup of the band-pass CS rapid interferer detector with a QAIC from the stimulus to the CS digital signal processing back end that consists of the support recovery and the simple signal estimation algorithm [2]. The demo system of the band-pass CS rapid interferer detector is operating over a 1GHz span ranging from 1.5 to 2.5GHz including ISM and some of the LTE frequency bands. The operating frequency range for the demo is shifted from the 2.7-3.7GHz PCAST band, where all the measurements are demonstrated in Section 4.4, to the 1.5-2.5GHz band due to the operating frequency range limitation of the external I/Q modulator modules in the custom-made signal generator box. By using the band-pass CS interferer detector

[2]The compressed sampling rapid interferer detector system was also demonstrated at the ISSCC 2015 live demo session that show cases the rapid detection of up to 3 interferers over a 1GHz-wide spectrum. Demo video of paper 19.4: http://isscc.org/videos/2015_ids.html

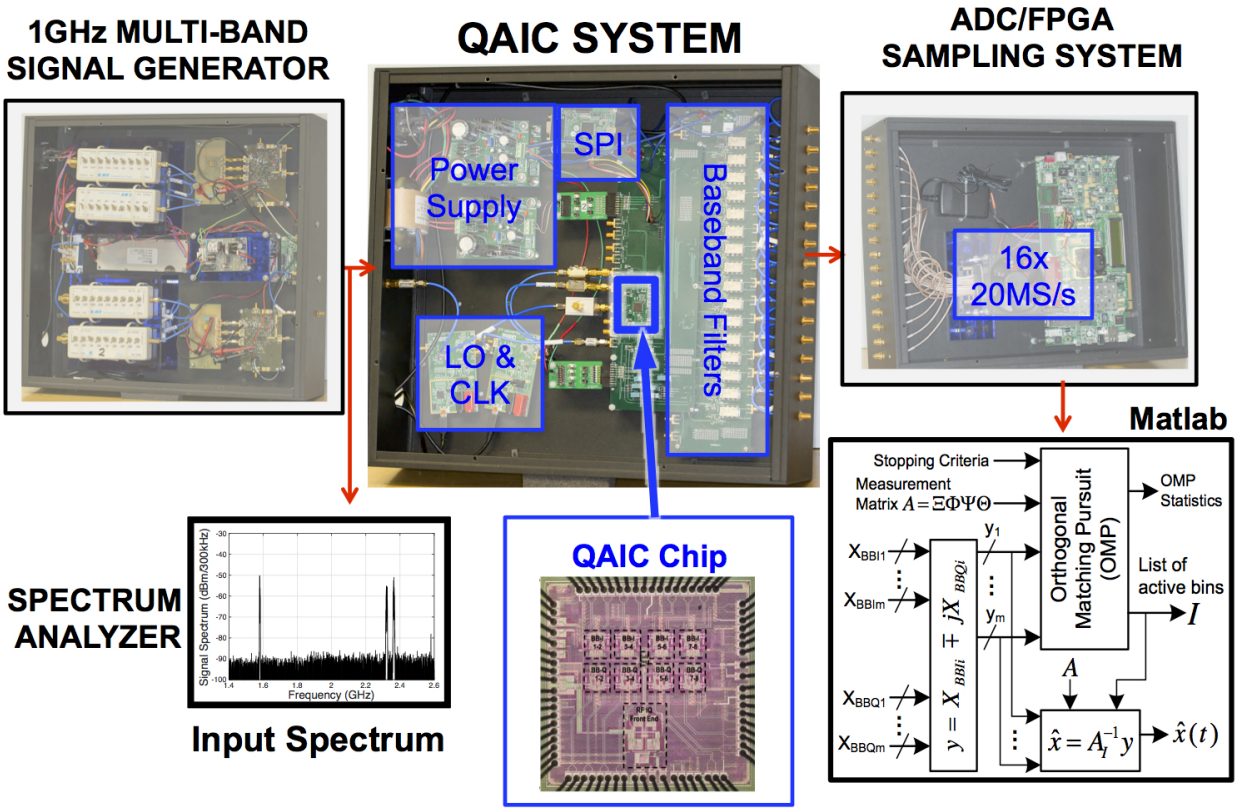

Figure 4.19: *The band-pass CS rapid interferer detector system with a QAIC demo platform from the stimulus to the CS digital signal processing back end.*

demo platform in the 1.5-2.5GHz frequency range, we further demonstrate the flexibility of the operating frequency range of the wideband QAIC system, when the quadrature downconverter clock is fed into the chip as an external clock to be divided by 2 on the chip.

The middle box is the quadrature analog-to-information converter system that consists of the QAIC chip implemented in 65nm CMOS GP technology. The QAIC system box further includes the sub-20 SPI interface module and off-chip PLL-based clock generator modules operating at 1.26GHz for the PN clock (f_{CLK}) and 4GHz for the I/Q downconverter clock that is divided by 2 on the chip to generate f_{lo} of 2GHz and baseband filters for testing flexibility.

At the output side, there is an ADC board together with an FPGA VC707 board which con-

stitute the sampling system of the band-pass CS interferer detector. The ADC board consists of 16 ADCs operating at a rate of 20MSps. We envision that the ADC sampling system with 16 20MSps-rate ADCs can be designed and integrated on a single chip with a QAIC front end. The CS complex-domain support recovery is implemented on MATLAB and employs the OMP algorithm to find the input signal frequency bins (a.k.a. supports) that exceed a pre-defined threshold. As the algorithm inputs, the OMP uses the QAIC complex-domain output samples, the measurement matrix based on the gold sequences, and the dictionary matrix. The dictionary matrix, $\mathbf{\Psi}$, is a discrete Fourier transform matrix with all the possible locations of the interferers in a 1GHz spectrum. User-specified performance targets like sensitivity are used to derive the adaptive stopping criteria for the OMP. Our main focus is support recovery that provides only the locations of the active interferers. Then we further perform a simple signal reconstruction for illustrative purposes that provides an estimate of the input signal. This is done by forming a pseudoinverse of the reduced measurement matrix (A_I) and solving directly for a solution from the QAIC complex-domain output samples y. An example test case, in which 1 active band is detected successfully at 2120MHz, is shown in Fig. 4.20 along with the graphical user interface that we use for the band-pass CS interferer detector with a QAIC system demo platform.

At the input side, we have a custom-made multi-band signal generator with a 1GHz-wide instantaneous bandwidth operating over the 1.5-2.5GHz interest spectrum range. Multi-band RF signals with up to 3 bands of 10MHz-wide upconverted filtered noise are generated and fed into the band-pass CS interferer detector with a QAIC. Users can set the active band (a.k.a. interferer) locations anywhere in between 1.5 to 2.5GHz and they can also select the desired RBW option

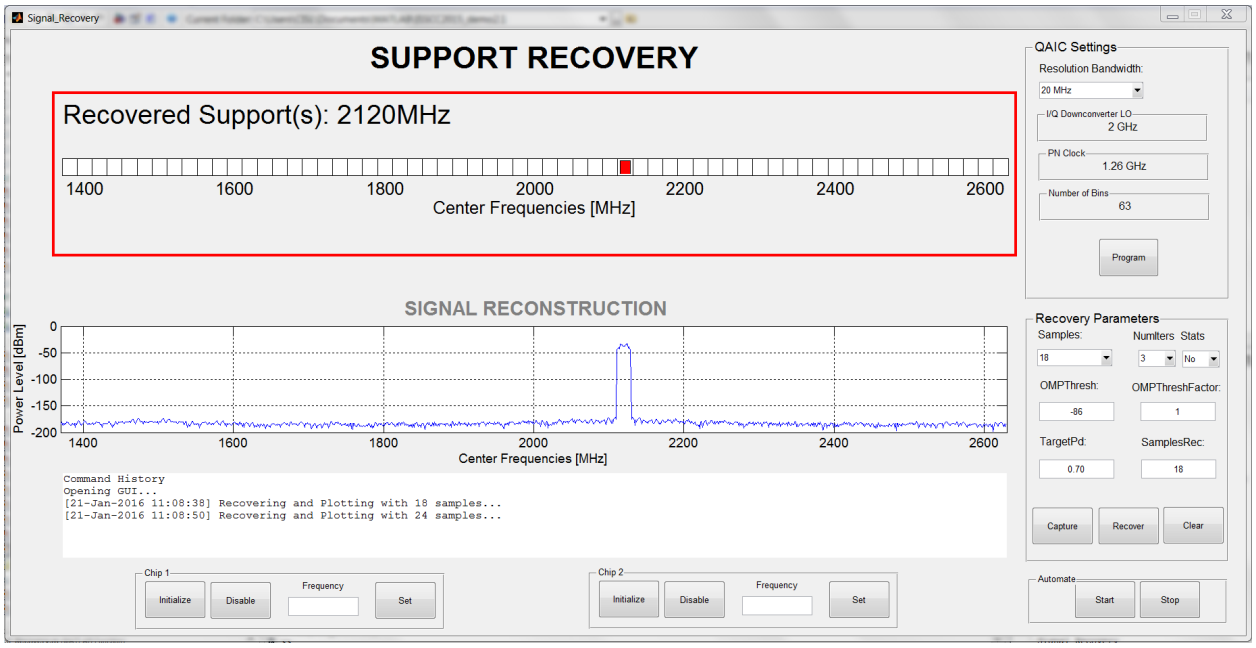

Figure 4.20: *The graphical user interface of the band-pass CS interferer detector with a QAIC system demo platform: An example test case, in which 1 active band (a.k.a. interferer) is detected successfully at 2120MHz.*

(10MHz or 20MHz) by using the graphical user interface shown in Fig 4.20. The power levels of the active bands are set manually with the step attenuators. The locations of the interferers are unknown to the band-pass CS detector with the QAIC chip but the signal power is split into a spectrum analyzer for the users to observe the input spectrum that emulates the interferers in the wideband 1GHz spectrum band.

4.6 Discussion and Comparison to the State of the Art

The available spectrum scanner and sensor architectures are compared in Table 4.2 in terms of scan time, estimated energy consumption and aggregate sampling rate for a 1GHz wideband spectrum sensing scenario with a 20 MHz RBW and it is assumed that all architectures use the same number

Table 4.2: *Comparison of the performance of spectrum scanner and sensor architectures estimated using first order models*

		Sweeping Spectrum Scanner	Nyquist FFT Spectrum Sensor	MWC Based Spectrum Sensor	This Work
Scan Time	**[µs]**	220	4	4.4	**4.4**
Relative Energy Consumption	**[E]**	50	50	10	**1**
Aggregate Sampling Rate	**[MSps]**	40	2000	580	**320**

of samples, $N_s = 80$. The proposed QAIC only requires $4.4\mu s$ of scan time given in (4.13) and it is 50 times faster than the sweeping spectrum scanner with a scan time given in (2.2). Assuming 3 supports in 50 bins, the QAIC requires only 8 I/Q branches in contrast to the 50 I/Q branches needed in a multi-branch traditional spectrum sensor for the same scan time. To the first order, it is 50 times more energy efficient than traditional architectures with an energy consumption given in (2.2). Furthermore, it is 10 times more energy efficient than a low-pass compressed sampling architecture employing a MWC with an energy consumption given in (3.3). The band-pass CS architecture with a QAIC only requires 320MSps aggregate sampling rate enabled by CS theory, which is a 6.3 times compression compared to Nyquist-rate architectures which require 2GSps.

Table 4.3 shows the comparison of the measured performance and system parameters of the QAIC [3, 5] and of state-of-the-art traditional and compressed sampling based spectrum scanners and sensors that are reported in [9, 10, 13–15, 18, 26, 28, 62, 63]. Table 4.4 shows the performance comparison of the QAIC [3] to the estimated performance of state-of-the-art traditional and compressed sampling based spectrum scanners and sensors [9, 10, 13–15, 18, 26, 28, 62, 63], that are scaled to sense a 1GHz span from 2.7 to 3.7GHz with a 20MHz RBW. The number of legs is scaled for 3 active supports, i.e. 16 for this work, 4 for [9, 10, 62], 2 for [13–15, 18, 63] and 29 for [26,28]. Even though the other CS approaches use more power hungry shift-register PN genera-

Table 4.3: *Comparison of the measured performance of the QAIC interferer detector to the state of the art in integrated spectrum sensors and scanners*

		[9, 10, 62]	[13]	[14]	[15]	[18, 63]	[26]	[28]	This Work [3, 5]
Architecture		Cross-Correlation SA	Dual Up/ Down Conversion SA	Multi-Resolution Spectrum Sensing	Tunable RF Filter & Dynamic-Range-Scalable Energy Detector	Digital & Analog Multi-Band Sensing (Hybrid SA)	Random-Modulation Pre-Integrator CS	Parallel Segmented CS	**CS with Quadrature Analog-to-Information Converter**
System Config.		Cross Correlation					Low pass CS	Low pass CS	**Band pass CS**
Application		Spectrum Analysis	Spectrum Analysis	Spectrum Analysis	Spectrum Analysis	Spectrum Analysis	Sub Nyquist Receiver	Sub Nyquist Receiver	**Sub Nyquist Interferer Detector**
CMOS Tech.	**[nm]**	65	130	180	90	40	90	90	**65**
Die Area	**[mm^2]**	< 0.26 (active area)	14.43	11.52	2.3	5	8.85	0.93	**1.96**
Supply Voltage	**[V]**	1.2	1.8	1.8	1.2	1.1	1.5 (A), 1.2 (D)	N/R	**1.1**
Frequency Range		50MHz-1.5GHz	100Hz-6GHz	600-603MHz[1]	30-334MHz (LPF) 334-800MHz (BPF) 800MHz-2.4GHz (Bypass)	500MHz-2.5GHz[2]	100MHz-2GHz	5-500MHz	**2.7-3.7GHz**
Number of Branches		4 = 2 x I/Q	2 = 1 x I/Q	2 = 1 x I/Q	2 = 1 x I/Q	2 = 1 x I/Q	8	8	**16 = 8 x I/Q**
RBW Options	**[MHz]**	1	0.4-11 (step 0.5)	0.194	0.2-30	1-40	N/R	5	**10, 20[3]**
PN Seq. Clock Rate	**[GHz]**	N/A	N/A	N/A	N/A	N/A	4	1.25	**1.26**
Sensitivity	**[dBm]**	-81 / -109[4,5]	-82[6]	-74	-83	N/R	-64[7]	N/R	**-72[8]**
Power	**[mW]**	166[9,10]	678.6[9]	180	30-44	33-99	506.4[9,11]	55[9,12]	**81[9,13]**

N/A = Not Applicable; N/R= Not Reported

[1] Measurements are shown for 600-603MHz signals; [2] Demo frequency range is reported; [3] RBW of 20MHz is the nominal setting for length 63; Fig. 15 shows RBW of 10MHz (length 127) and RBW of 20MHz (length 63); [4] Calculated the -81dBm from the -141dBm/Hz DANL for a 1MHz RBW and calculated the -109dBm from the -169dBm/Hz DANL for a 1MHz RBW; [5] After cross-correlation, the sensitivity is -109dBm for a 1MHz RBW; [6] Maximum gain setting; [7] For a single tone detection; [8] For a single band detection; [9] ADC off-chip; [10] Estimated DSP power consumption is 25mW; [11] Without output buffers; [12] Estimated ADC power is less than 1mW (neglected) and estimated PLL power is 1mW; [13] 400fF on-chip capacitors are included to emulate the ADC load.

Table 4.4: *Spectrum sensor and scanner performances normalized for 2.7 to 3.7GHz operation with a RBW of 20MHz*

		[9, 10, 62]	[13]	[14]	[15]	[18, 63]	[26]	[28]	This Work [3, 5]
Architecture		Cross-Correlation SA	Dual Up/ Down Conversion	Multi-Resolution Spectrum Sensing	Tunable RF Filter & Dynamic-Range-Scalable Energy	Digital & Analog Multi-Band Sensing (Hybrid SA)	Random-Modulation Pre-Integrator CS	Parallel Segmented CS	**CS with Quadrature Analog-to-Information Converter**
Scaled PN Seq. Clock for LFSR	**[GHz]**	N/A	N/A	N/A	N/A	N/A	10.22	10.22	**1.26**
Power Est. w/ PLL & ADC (Est.)	**[mW]**	375	256	335	115	111	607	1,056	**115**
Front-End Response Time	**[µs]**	20	20	20	20	20	0.4	0.4	**0.4**
Scan Response Time (Est.)	**[µs]**	220 - 1,760[1]	220	220	220	220[2]	4.4	4.4	**4.4**
Energy (Est.)	**[µJ/scan]**	83 - 660	56	74	25	24	2.7	4.6	**0.5**
Relative Energy per Scan (Est.)		166 - 1320x	112x	148x	50x	48x	5.4x	9.2x	**1x**

N/A = Not Applicable; Est. = Estimated

[1] Cross correlation doubles the measurement time for each 1.5dB NF improvement; we assumed NF from 17dB to 12.5dB for the scan response time estimation; [2] Reported scan time is 7.6ms for a 2GHz band given the LO settling time and assuming 1024 samples are needed at a sampling rate of 40MSps for a RBW of 20MHz.

tors, the PN generator power has been scaled assuming an LFSR with the required length and clock frequency. Power estimations of PLLs and ADCs included for all architectures; [13, 14, 18, 63] already includes on-chip synthesizers. ADCs are assumed to be 8-bit, 20MSps with 0.9mW power consumption [19]. The PLL power consumption of 20mW for the gold sequence generator clock, the quadrature downconverter fixed LO and the sweeping LO is estimated based on [64, 65].

Fig. 4.21 shows the front-end energy consumption per scan of various architectures [9, 10, 13–15, 18, 26, 28, 62, 63] relative to that of the QAIC [3, 5] versus the scan time. We note that the performance of all architectures has been normalized to sense a 1GHz span from 2.7 to 3.7GHz with a 20MHz RBW. The performance comparison shows that a QAIC offers rapid and energy-efficient spectrum sensing over a wide instantaneous bandwidth compared to the traditional spectrum scanners/sensors and the existing low-pass CS spectrum sensors.

The presented system architecture in this chapter, QAIC, uniquely exploits band-pass compressed sampling for the rapid sensing of large spectral bandwidths with high frequency resolutions, while keeping the hardware and energy requirements modest. We envision that the band-pass

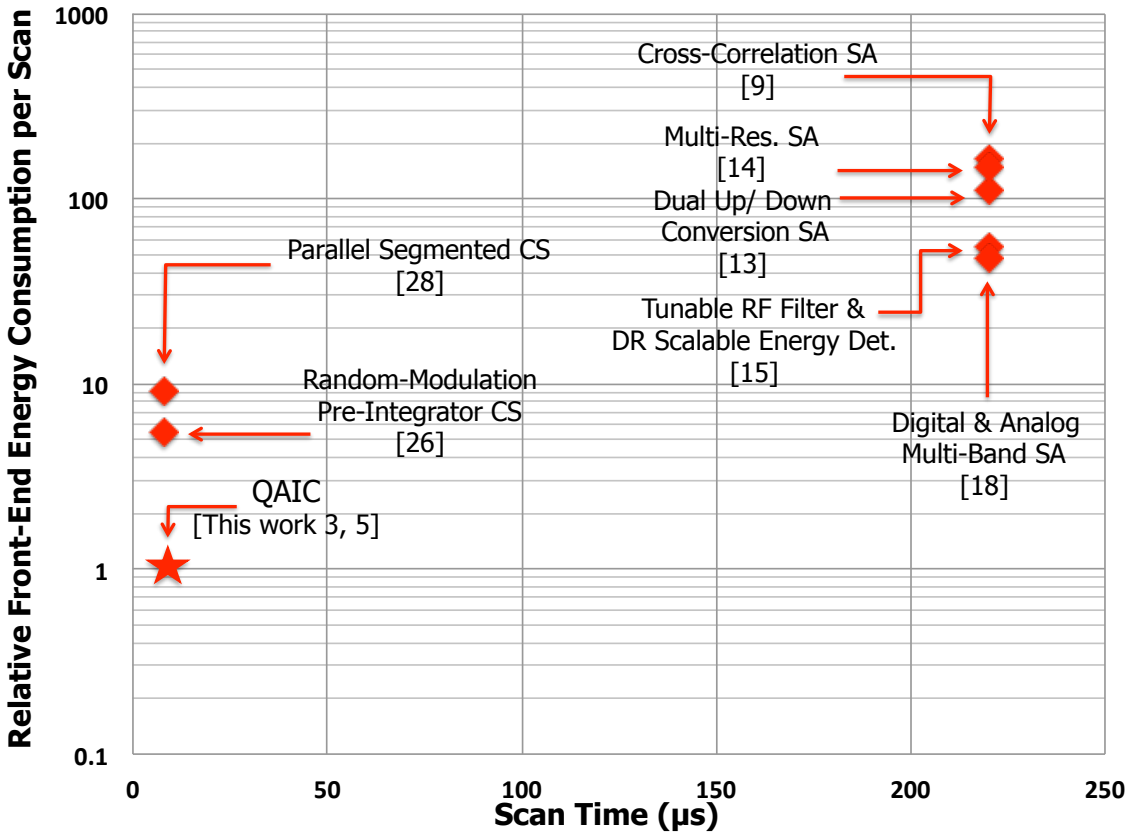

Figure 4.21: *Relative front-end energy consumption per scan versus scan time for various spectrum scanners and sensors; the energy has been normalized for operation over a frequency span from 2.7 to 3.7GHz with a RBW of 20MHz. See Table 4.4 for the details.*

compressed sampling solution opens promising avenues towards energy-efficient and rapid sensing architectures for future cognitive radio systems utilizing multi-tiered shared spectrum access.

Chapter 5

Compressed Sampling Time-Segmented Quadrature Analog-to-Information Converters with Adaptive Thresholding

Shown in the LTE-U deployment scenario example, Fig. 1.3, a cognitive radio terminal with a rapid interferer detector periodically senses the shared spectrum before every data packet transfer and opportunistically aggregates component carriers. As discussed in Chapter 1, such future cognitive terminals will need to rapidly (in 10s of μs) detect a few (e.g. 4 to 6) strong interferers within roughly a 1GHz span.

Integrated spectrum scanners, like [9, 13, 15] rely on traditional spectral analysis which has a fixed trade-off between span, RBW and scan time. Rapidly (e.g. in 10s of μs) detecting a few strong interferers over a 1GHz span with a 20MHz RBW and with low energy consumption is not possible with traditional Nyquist-rate spectrum analyzers. Recent work [34] demonstrates an under-sampling blocker detector that rapidly detects blockers with low power over a wide bandwidth, however their implementation is limited to 2 interferers. Compressive sampling can break the traditional trade-off between span, RBW and scan time by sampling at sub-Nyquist rates. Low-

pass CS architectures, like [26, 28, 42] sense the spectrum from DC to f_{max} and are more suitable for baseband applications. There is a need to mix with high Nyquist-rate pseudorandom noise (PN) sequences which diminishes the energy savings offered by low-pass CS especially at RF frequencies. Band-pass CS architectures, like the QAIC [3–5] discussed in Chapter 4 offer very short scan times compared to traditional spectrum analyzers and lower power consumption for RF frequencies compared to low-pass CS architectures. Increasing the number of interferers that can be detected with the QAIC requires a proportional increase in the number of physical I/Q branches. However, increasing the hardware complexity and silicon cost of the QAIC to accommodate 6 interferers would be overkill given the QAIC can detect 3 interferers in 4.4μs and the spectrum is typically stationary for 10s of μs.

In this chapter, adaptive thresholding and extension of physical hardware through time segmentation that enable the rapid (in 10.4μs) detection of 6 interferers without additional silicon cost and complexity are presented.

5.1 A Rapid Adaptive Sensing Approach Exploiting Compressive Sampling with Time Segmentation

A rapid adaptive sensing approach exploiting compressive sampling that employs a time-segmented quadrature analog-to-information converter front end (TS-QAIC) and an information recovery engine (IRE) back end that can detect up to 6 interferers over a 1GHz instantaneous bandwidth between 2.7 and 3.7GHz in 10.4μs is shown in Fig. 5.1. This 'sense-and-adapt' approach co-

optimizes the adaptive analog-to-information converter (AIC) front end and the scalable back-end IRE based on the user preferences and the application requirements.

Scalability dimensions of the rapid CS interferer detector system consisting of the TS-QAIC front end and the TS-IRE back end are shown in Fig. 5.1. Through time segmentation and adaptive thresholding, the TS-QAIC [8] extends its physical hardware that is otherwise limited by silicon cost and complexity. This enables adaptive system scaling for user specified performance goals (e.g. performance metrics shown in Fig. 5.1) like the number of detectable interferers, the energy consumption of the system, and the scan time allowed for the system based on the deployment scenario.

In implementing this adaptive system scaling, the TS-QAIC maintains advantage in power consumption and sensitivity of band-pass CS approaches [3, 5] as compared to low-pass CS architectures [26, 28, 42, 43].

5.2 Using Time Segmentation and Adaptive Thresholding to Increase the Number of Detectable Interferers

5.2.1 Compressed Sampling Time Segmentation

Assuming the spectrum is stationary for e.g. 10.4μs, Fig. 5.2 shows how a CS TS-QAIC maps the spectral information by employing time segmentation to detect 6 interferers in the 2.7 to 3.7GHz range successfully with only half the number of required physical I/Q branches compared to a QAIC (m_{QAIC}) [3]. TS-QAIC only requires 8 physical I/Q branches rather than 16 physical I/Q

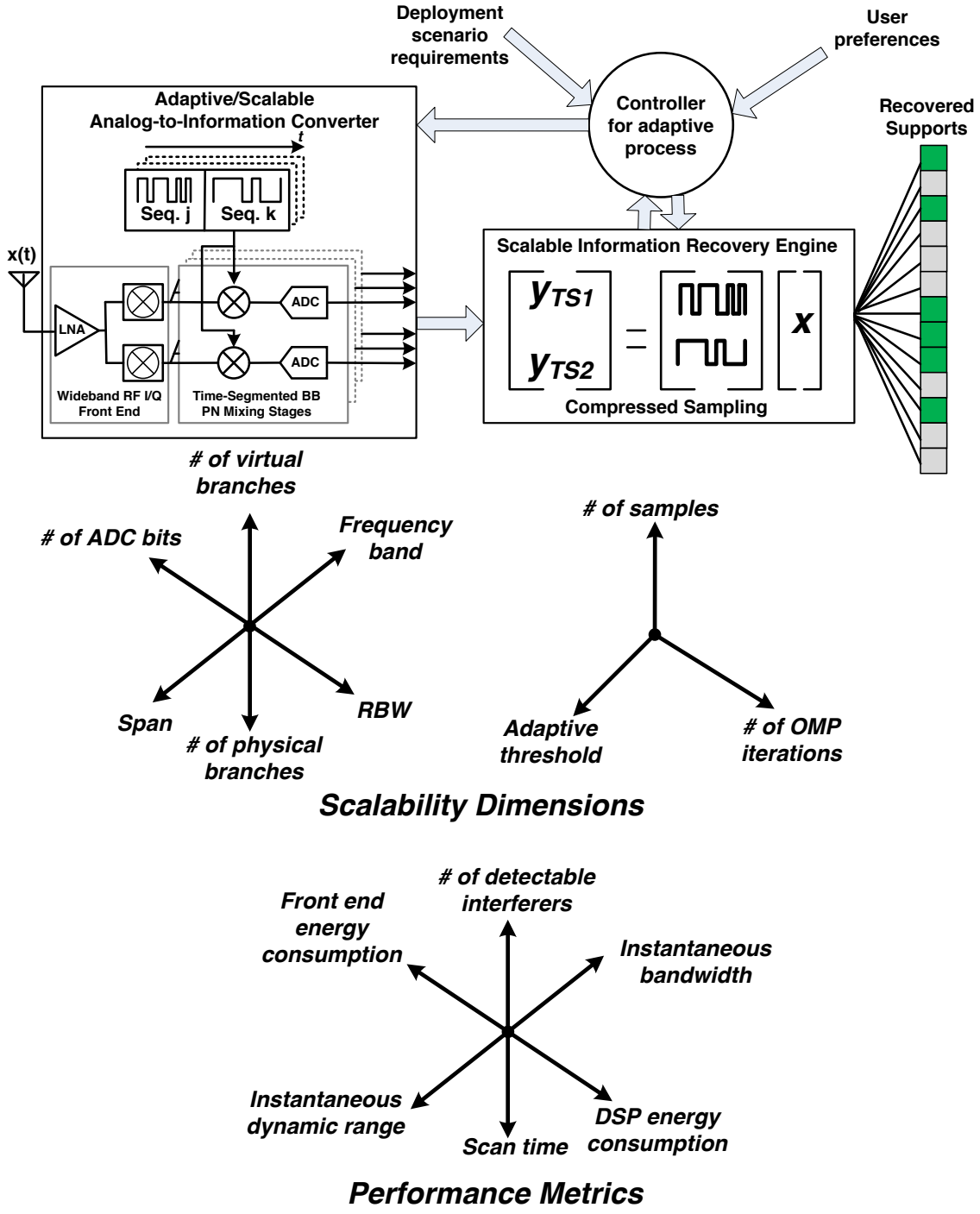

Figure 5.1: *A rapid adaptive sensing approach exploiting CS that employs a TS-QAIC front end and a TS-IRE back end with their scalability dimensions and the system performance metrics.*

branches for K_0=6 interferers in a 1GHz instantaneous bandwidth with a 20MHz RBW. Time segmentation accomplishes extension of physical branches by creating unique measurements of the spectrum from one branch with time-segmented gold sequences $\left(g_{j/k}(t)\right)$. For each successive use of the core physical hardware, time-segmented gold sequence generator is configured to generate a different set of 8 unique gold sequences. By switching between the gold sequences $g_j(t)$ and $g_k(t)$, twice the number of unique CS measurements are obtained. The CS time-segmented measurements are equivalent to the unique measurements that can be obtained from twice the number of physical branches for a stationary spectrum.

5.2.2 Compressed Sampling with Adaptive Thresholding

We further demonstrate adaptive thresholding in the time-segmented CS digital signal processing (DSP). Shown in Fig. 5.3 is an example of the adaptive thresholding approach employed by the CS TS-QAIC. Within the first sense slot shown in Fig. 5.3 and also in Fig. 1.3, the time segmentation is disabled (**TS OFF**) and only 8 complex-domain measurements are collected from the TS-QAIC's 8 physical I/Q branches. In the CS IRE (a.k.a. CS DSP), the adaptive threshold level is set to high to make the CS signal processing algorithm blind to the signals below the threshold level. In this example, the orthogonal matching pursuit (OMP) algorithm is employed for CS DSP complex-domain support recovery and the OMP residual is used as the feedback mechanism to assist the TS-QAIC hardware extension through time segmentation. The 3 strongest interferers are detected successfully in 4.4μs with 8 physical I/Q branches when the time segmentation is disabled (**TS OFF**) and the OMP residual is at a high level after 3 OMP iterations.

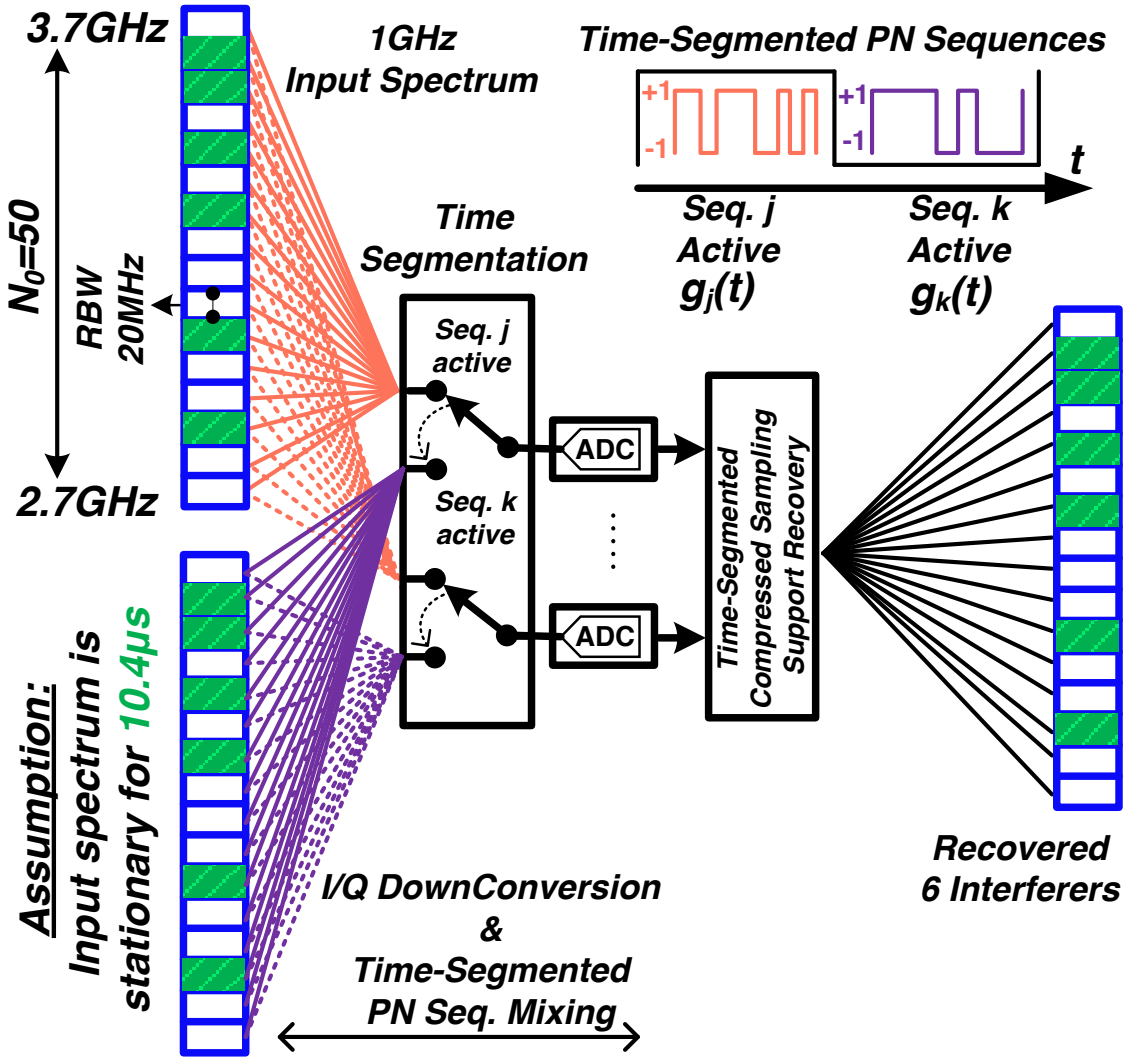

Figure 5.2: *Conceptual illustration of the band-pass compressed sampling time-segmented quadrature analog-to-information converter (TS-QAIC) operation. Six interferers above the adaptive threshold level in a 1GHz span are shaded in green.*

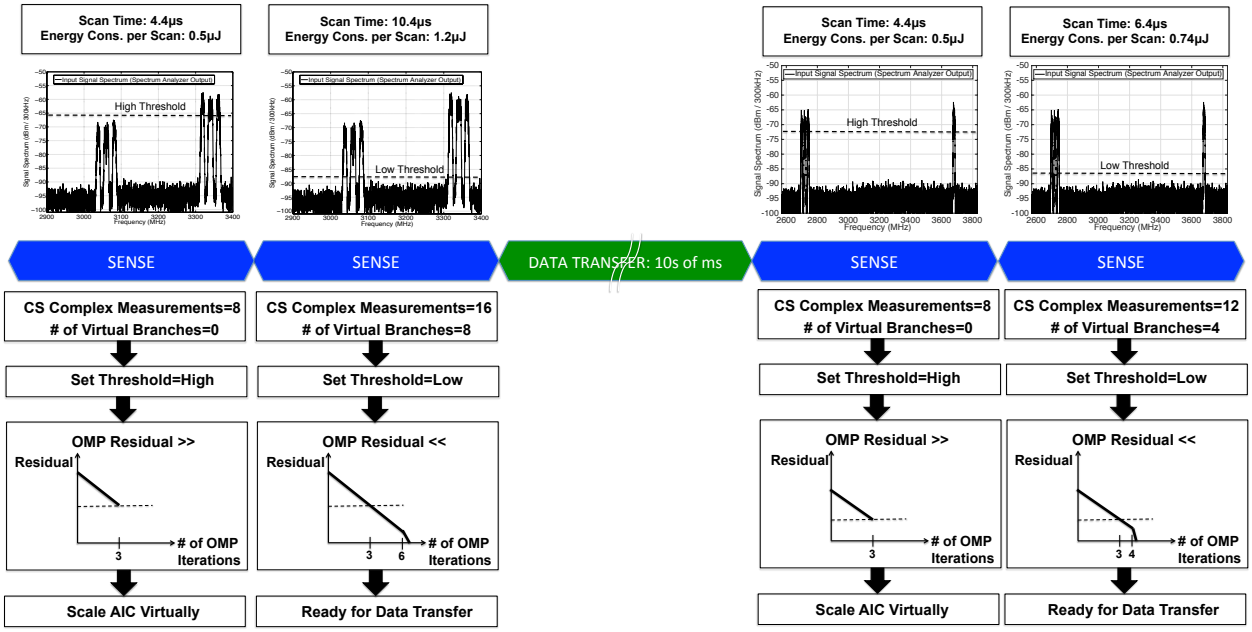

Figure 5.3: *An example of the 'sense-and-adapt' approach that is enabled by the adaptive scalability of the CS TS-QAIC through adaptive thresholding and time segmentation.*

If the OMP residual is at a high level, adaptive thresholding adjusts the threshold for the second sense period and time segmentation is enabled to detect more interferers and adapt to the signal conditions in the 1GHz spectrum band. The TS-QAIC is then scaled to extend the number of branches to 16 virtual I/Q and the adaptive threshold level is set to low to detect the remaining interferers that were below the high threshold during the first sense slot. Six interferers are detected successfully in 10.4μs. Since the OMP residual is low after 6 OMP iterations, interferer detection is completed during the second sense slot and the cognitive radio terminal is ready for data transfer. Following the data transfer, the spectrum is changed and it consists of 4 strong interferers. Based on the OMP residual feedback from the IRE, the TS-QAIC scales its branches to 12 virtual I/Q branches rather than 16, which reduces the scan time by 4μs and the energy consumption by 0.46μJ with adaptive scalability.

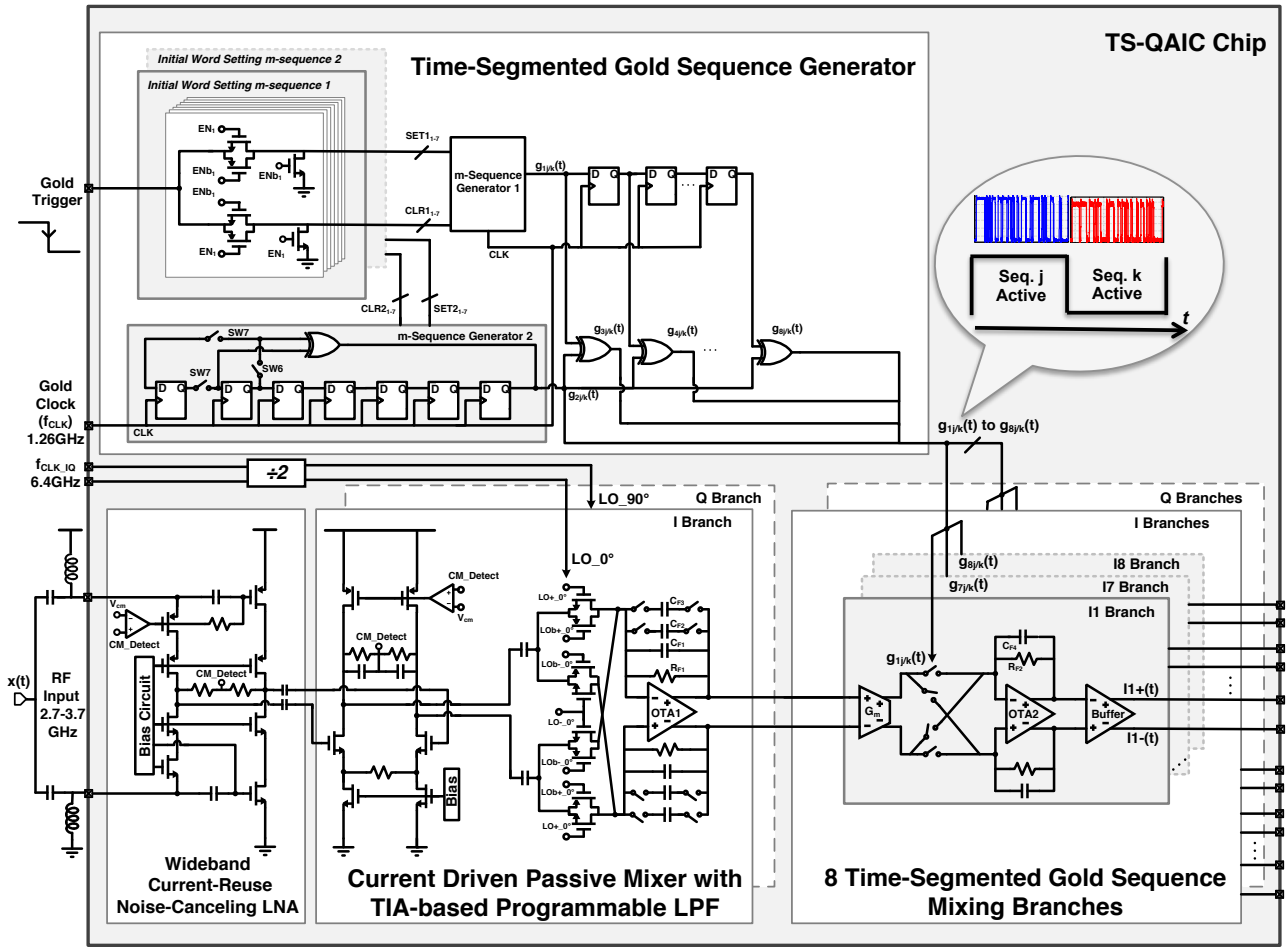

Figure 5.4: *Circuit implementation of the compressed-sampling time-segmented quadrature analog-to-information converter (TS-QAIC).*

5.3 Implementation of the Rapid Interferer Detector with a Time-Segmented Quadrature Analog-to-Information Converter

The 2.7-3.7GHz TS-QAIC prototype circuit implementation is shown in Fig. 5.4. The chip has been implemented in 65nm CMOS GP technology.

5.3.1 Circuit Implementation of the CS TS-QAIC RF Front-End Blocks

The TS-QAIC front end employs a wideband current-reuse noise-canceling low-noise amplifier (NC LNA) [66]. The complementary current-reusing approach provides current savings since it requires only half the g_m from the complementary branches with a small penalty in input bandwidth. For a typical process corner, the post-layout simulated LNA gain is 16.9 to 15dB from 2.7 to 3.7GHz while the post-layout simulated LNA noise figure is 2.4 to 2.69dB. The simulated $S_{11} < -15dB$ from 2.7 to 3.7GHz and the simulated in-band IIP3 is +6dBm. The measured LNA power consumption is 5.7mW from a 1.2V supply.

The current-reuse NC LNA is followed by an RF I/Q downconverter consisting of current-driven passive I/Q mixers and transimpedance amplifiers (TIAs) [52–54] with wideband programmable bandwidth settings of 125MHz, 250MHz, and 500MHz. The input stage is implemented as a transconductance G_m amplifier with a source degeneration resistor. An off-chip RF clock is fed to the chip to generate 3.2GHz quadrature LO signals with a 50% duty cycle with on-chip divide-by-2 circuitry. Programmable capacitors are added to the TIA feedback network so as to zoom into the span after a coarse sensing of the spectrum. The effective noise bandwidth that accounts for the noise folding due to the mixing with pseudorandom noise (PN) sequences tracks the instantaneous bandwidth (span) of the TS-QAIC. By programming the bandwidth of the wideband TIA-based filter, the user can reduce the impact of noise folding on the effective sensitivity level. The simulated in-band IIP3 is +8.2dBm for a typical process corner. The measured power consumption of the RF I/Q downconversion stage including the current-driven passive I/Q mixers,

programmable wideband TIA-based filters, and I/Q LO generation based on divide-by-2 circuitry is 18.37mW from a 1.2V supply.

5.3.2 Time-Segmented PN Sequence Generation and CS Time-Segmented Baseband Circuits

The RF I/Q downconverter is followed by 8 I/Q baseband time-segmented PN mixing branches that are driven by two sets of 8 unique time-segmented PN sequences. The baseband transconductance G_m amplifier employs a source degeneration resistor and an individual common mode feedback (CMFB) control. Baseband low-pass filtering is performed with a TIA that is implemented as a two-stage OTA with Miller compensation. Since AC coupling capacitors with a tolerable size can not be employed in the baseband, two individual CMFB control circuits are preferred to control the DC voltages on the source and drain terminals of the mixer switches to prevent DC current through the switches for flicker noise concerns. When the 8 I/Q baseband PN mixing branches are driven by a square LO for RF characterization, for a typical process corner, the simulated in-band IIP3 is +4.3dBm. The measured total power consumption of the 8 I/Q baseband time-segmented PN mixing branches is 36.88mW from a 1.2V supply.

The 8 I/Q baseband time-segmented PN mixing branches are driven by two sets of 8 unique time-segmented PN sequences generated by the on-chip time-segmented gold sequence generator. The on-chip time-segmented gold sequence generator block has a programmable set/reset option for two 6 flip-flop LFSRs to generate unique sequences by setting the initial word. When the external gold trigger signal goes from high to low, the initial word of the two m-sequences will be

set and the gold sequences will start switching in a synchronous manner with respect to each other. For a 20MHz RBW and a 1GHz instantaneous bandwidth, the 8 I/Q time-segmented PN mixing stages are driven by 6 time-segmented 63-long gold sequences and 2 time-segmented 63-long m-sequences with sufficiently low cross correlation and low mutual coherence in the CS sensing matrix [6, 47, 56]. Mutual coherence properties of an optimal sensing matrix ϕ_1 and a sub-optimal sensing matrix ϕ_2 constructed from two time-segmented gold sequence sets are shown in Fig. 5.8 for all the sensing matrix column combinations. Fig. 5.8 shows that the optimal sensing matrix ϕ_1 has a lower average and a lower maximum mutual coherence which is needed for successful CS support recovery. The measured power consumption of the time-segmented gold sequence generator is 6.68mW from a 1.2V supply.

5.3.3 CS Digital Signal Processing for Time-Segmented Rapid Sensing

Fig. 5.5 shows the time-segmented rapid sensing approach in terms of the CS problem '$y = \phi\psi x$', where y are samples from the TS-QAIC chip, x is the interferer spectrum that remains stationary during slot boundaries or portions of sub-frames (e.g. $10.4\mu s$), ψ is the dictionary matrix, and ϕ is the sensing matrix constructed from two sets of unique gold sequences generated by the time-segmented gold sequence generator on the TS-QAIC chip. This CS problem '$y = \phi\psi x$' is solved in the information recovery engine from the TS-QAIC complex samples to successfully locate up to 6 interferers in a 1GHz spectrum.

The CS digital signal processing details of the rapid interferer detector with a TS-QAIC are shown in Fig. 5.6 for m I/Q physical branches extended to m_j and m_k branches through time seg-

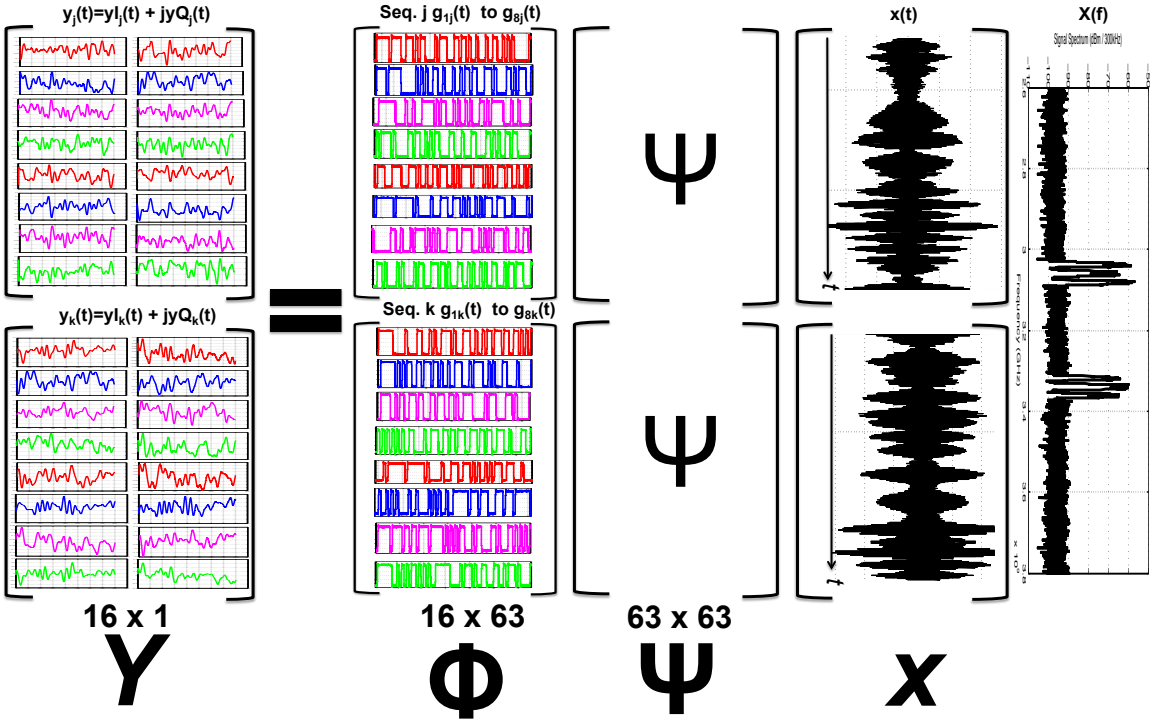

Figure 5.5: *Time-segmented rapid sensing approach is illustrated in terms of compressed sampling 'y = ϕψx' problem with physical waveforms collected from the TS-QAIC chip.*

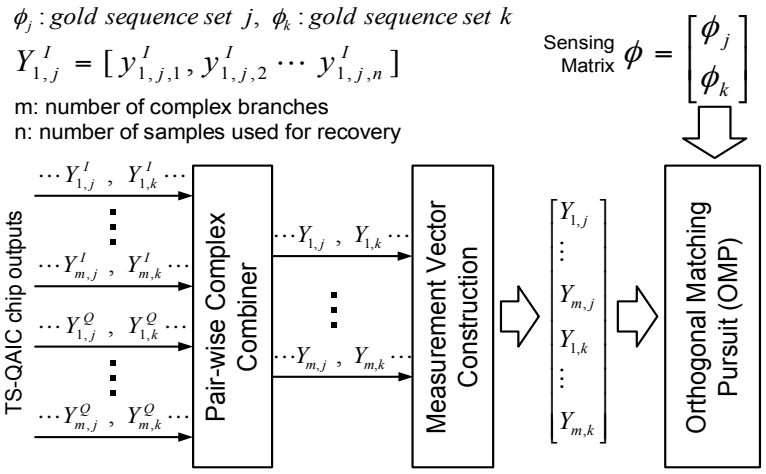

Figure 5.6: *CS time-segmented digital signal processing algorithm details.*

mentation. The time-segmented sensing matrix is constructed from two sets of m unique PN sequences indexed as j and k, while the orthogonal matching pursuit (OMP) algorithm [58, 59] is used to identify the input bands that exceed an adaptive threshold by using the time-segmented complex measurements from the TS-QAIC chip.

CS Time-Segmented DSP Energy Estimation for a Complex-Domain Support Recovery: For the successful detection of 6 interferers (K_0=6), 16 time-segmented I/Q branches ($m_{j,k}$=8 physical I/Q branches and 8 virtual I/Q branches) with 63-long gold sequences (L=63) and 100 samples (n_s=100) are employed to maximize the detection probability. The total number of complex multiplications and additions needed by the OMP is roughly $n_s \cdot K_0 \cdot m_{j,k} \cdot L$. The computational load of the OMP given in (4.16) is found to be roughly $2673nJ$ for real additions and multiplications, assuming that an 16x16 multiplier and an 16-bit adder with a settling time less than $17ns$ consume $60\mu W$ and $5\mu W$ respectively [60, 61].

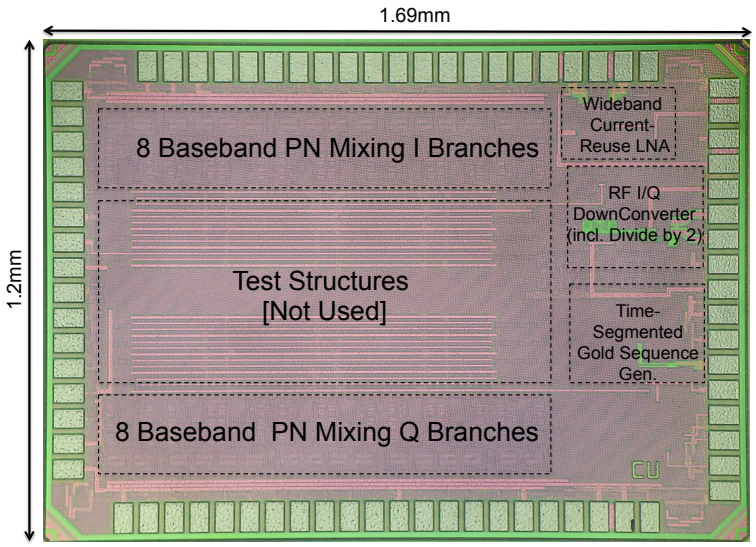

Figure 5.7: *Die photograph of the 65nm TS-QAIC prototype.*

5.4 Band-pass CS TS-QAIC with Adaptive Thresholding Measurement Methods and Results

Shown in Fig. 5.7, the TS-QAIC prototype active area consists of the RF I/Q front end, 8 I/Q baseband time-segmented PN mixing stages, and the time-segmented gold sequence generator. The active area of the TS-QAIC prototype chip is $0.517mm^2$ in 65nm CMOS GP technology. The measured power consumption of the TS-QAIC is 81.2mW from a 1.2V supply.

For experimental validation of the TS-QAIC, multi-band RF signals with up to 6 bands of 10MHz-wide upconverted filtered noise are generated and are fed into the chip. Time-segmented gold sequence sets with low mutual coherence are selected. The time-segmented I/Q outputs from the TS-QAIC chip are digitized by using 8 bit oscilloscopes at a rate of 20MSps and stored for off-line CS DSP complex-domain support recovery with adaptive thresholding.

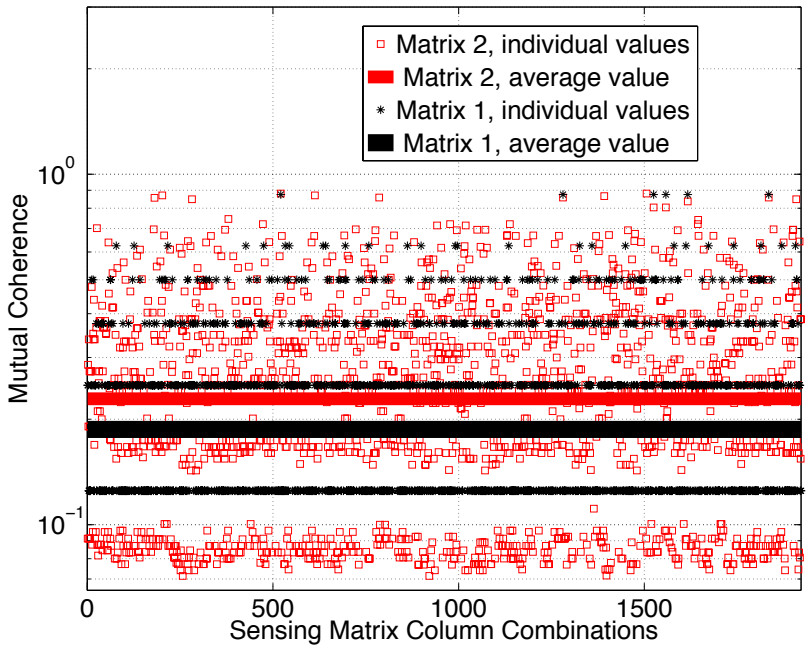

Figure 5.8: *Mutual coherence properties of an optimal sensing matrix (ϕ_1) and a sub-optimal sensing matrix (ϕ_2).*

5.4.1 Time-segmented Gold Sequence Set Selection Criteria

Fig. 5.8 and Fig. 5.9 illustrate how to select time-segmented gold sequence sets for optimal detection probability (P_D) and false alarm probability (P_{FA}) performance of the TS-QAIC. The measured P_D and P_{FA} for varying power levels per band for 6 interferers is shown in Fig. 5.9. Two sensing matrices, an optimal sensing matrix ϕ_1 and a sub-optimal sensing matrix ϕ_2, each constructed from two time-segmented gold sequence sets but with different properties, i.e. mutual coherence shown in Fig. 5.8, are employed for these measurements. The measured P_D is $\geq 90\%$ for signals with a power level ≥ -70dBm/10MHz when the optimal sensing matrix ϕ_1 is selected since the optimal sensing matrix has a lower average and a lower maximum mutual coherence, while the sub-optimal sensing matrix ϕ_2 cannot deliver a $P_D \geq 90\%$.

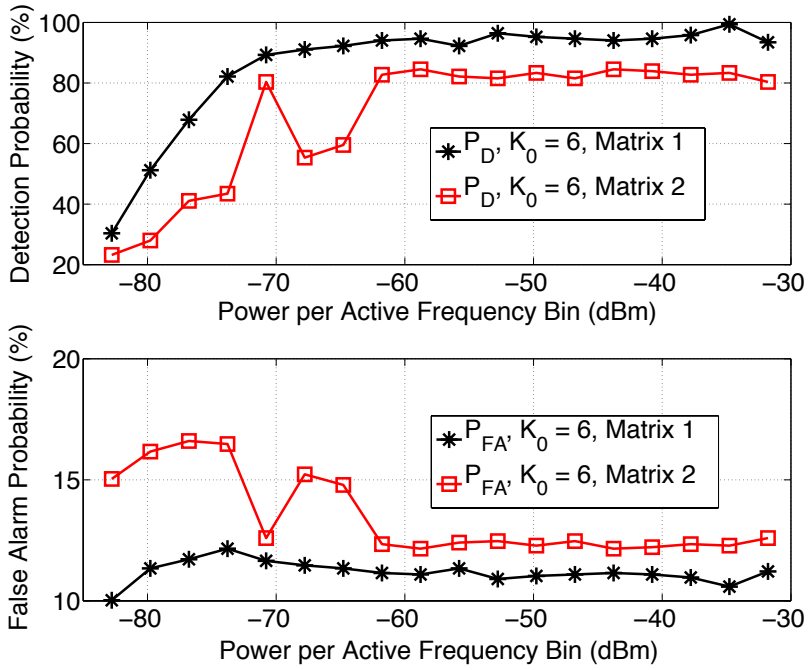

Figure 5.9: *TS-QAIC probability of detection and false alarm performance with sensing matrix* ϕ_1 *(optimal) and* ϕ_2 *(sub-optimal).*

5.4.2 Compressed Sampling Time-Segmented Digital Signal Processing Optimization

Fig. 5.10 shows the measured P_D and P_{FA} for varying power levels per band for $K_0 = 6$ interferers with a different number of OMP iterations employed in the information recovery engine. This measurement demonstrates an example of how to co-optimize the information recovery engine and the TS-QAIC system performance by choosing the optimum number of OMP iterations. Shown in Fig. 5.10, with 12 OMP iterations, the target P_D is $\geq 90\%$, while keeping the P_{FA} well below 15%. However, increasing the OMP iterations to 14 does not significantly increase P_D but rather inflates P_{FA} ($P_{FA} \geq 15\%$). In the information recovery engine, the OMP threshold is chosen first for the best detection probability performance and the false alarm probability is then controlled

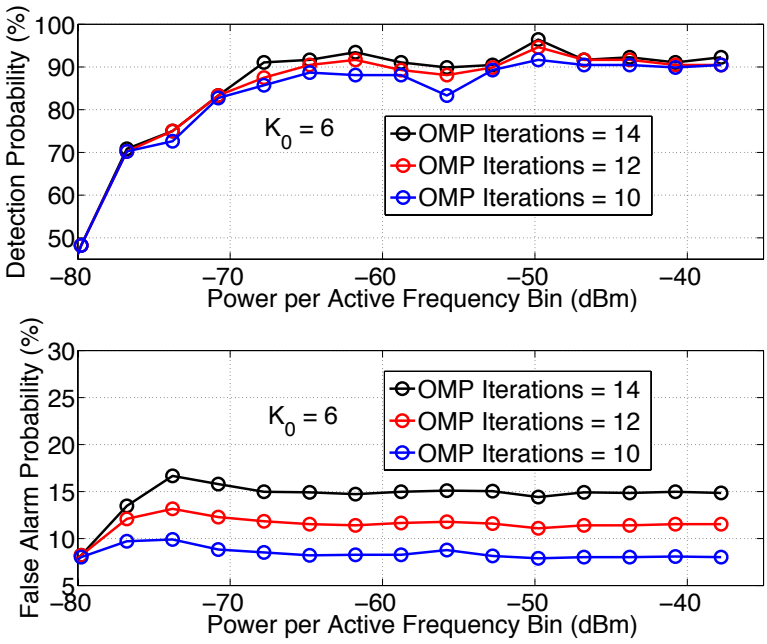

Figure 5.10: *Rapid interferer detector with a TS-QAIC measured system co-optimization illustration for minimum DSP energy consumption.*

by employing the appropriate OMP stopping criteria. Fewer OMP iterations lead to reduced DSP energy consumption.

5.4.3 TS-QAIC Time Segmentation Demonstration

The measured P_D and P_{FA} for varying power levels per band for $K_0 = 6$ interferers with and without enabling time segmentation are demonstrated in Fig. 5.11. When the time segmentation is disabled (**TS OFF**), the measured P_D degrades drastically and stays around a maximum value of 50% for 6 strong interferers since 8 I/Q branches is lower than the theoretical limit for the required number of branches [3, 4]. When the time segmentation is enabled (**TS ON**), the measured P_D performance improves significantly for the 16 virtual I/Q branches and the P_D remains $\geq 90\%$ for 6 interferers

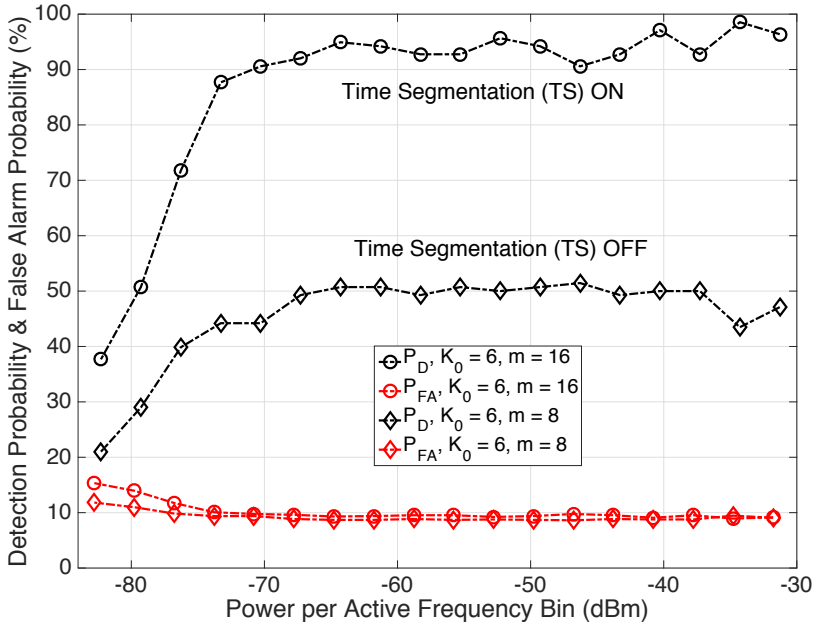

Figure 5.11: *Measured TS-QAIC probability of detection and false alarm for K_0 =6 interferers with 100 samples from 8 I/Q branches when the time segmentation is disabled (**TS OFF**), from 16 virtual I/Q branches when the time segmentation is enabled (**TS ON**) to extend the physical branches.*

with a power level per active band $\geq$-70dBm/10MHz. Enabling time segmentation thus allows the detection of twice the number of interferers without doubling the amount of hardware.

5.4.4 TS-QAIC Sensitivity with Time Segmentation

The measured P_D and P_{FA} for varying power levels per band for $K_0 = 4$, 5 and 6 interferers when the time segmentation is enabled (**TS ON**) and the optimal sensing matrix ϕ_1, consisting of two sets of time-segmented 8 unique gold sequences, is selected for the successful CS support recovery are shown in Fig. 5.12. For the measured P_D of $\geq 90\%$, six interferers as small as -70dBm/10MHz can be detected in 10.4μs by using 100 samples from 8 physical I/Q TS-QAIC branches extended

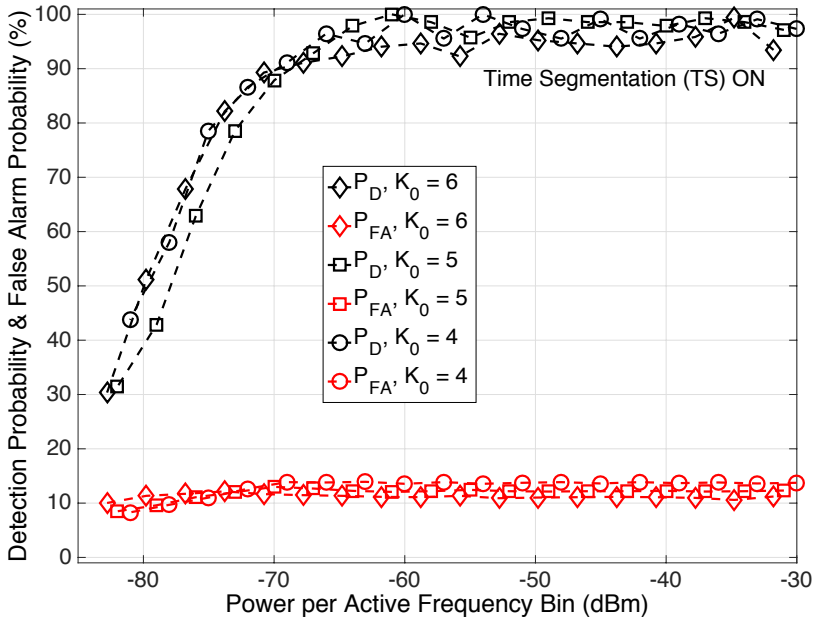

Figure 5.12: *Measured TS-QAIC probability of detection and false alarm with the optimal sensing matrix ϕ_1 for K_0 =4,5 and 6 interferers with 100 samples from 8 physical I/Q branches extended to 16 virtual I/Q through time segmentation.*

to 16 through time segmentation for CS complex-domain support recovery, while keeping the P_{FA} below 15%.

5.4.5 TS-QAIC Adaptive Thresholding Demonstration

TS-QAIC adaptive system scaling through adaptive thresholding when time segmentation is disabled and enabled is demonstrated in Fig. 5.13. In this measurement, the TS-QAIC system consisting of the analog-to-information converter (AIC) hardware and information recovery engine (IRE) is scaled through time segmentation by extending the physical AIC hardware and through adaptive thresholding in the IRE. Six interferers with a 10dB power difference between each of the 3 strong interferers with -44.77dBm/10MHz and the 3 weak interferers with -54.77dBm/10MHz are fed

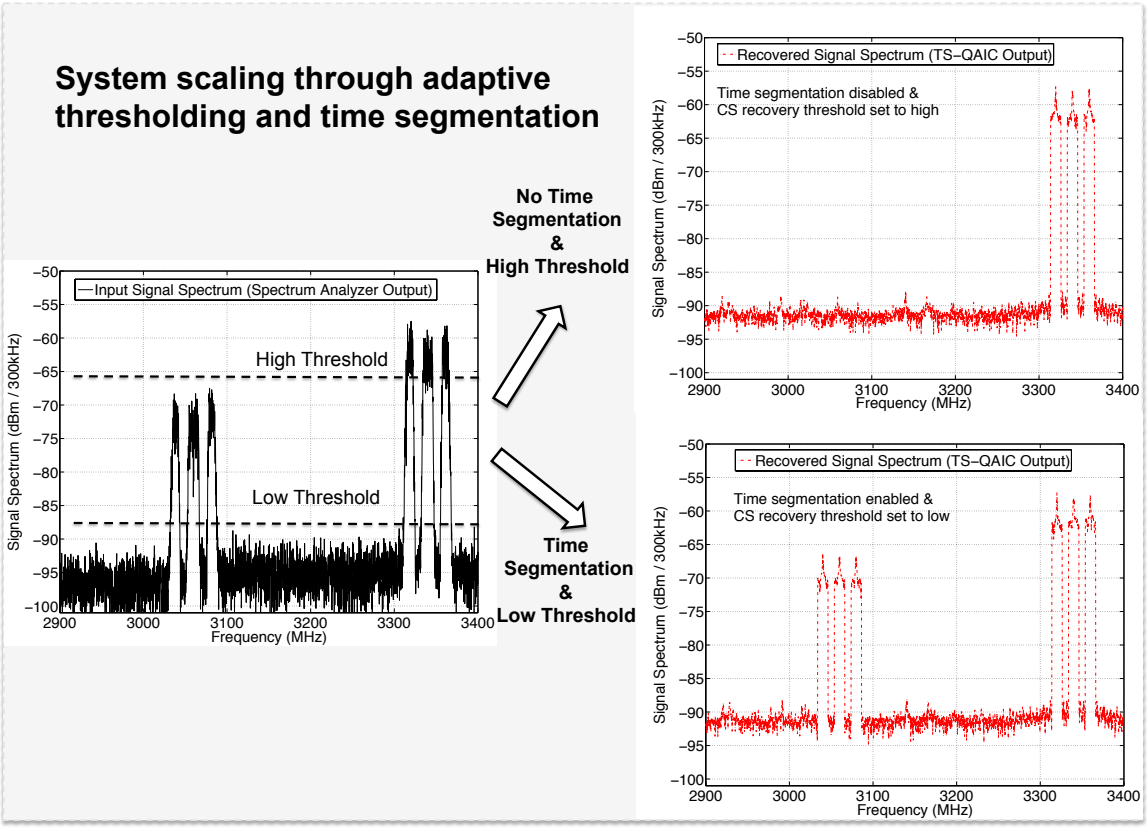

Figure 5.13: *TS-QAIC adaptive system scaling demonstration through the adaptive thresholding when the time segmentation is disabled and through the extension of the physical hardware when the time segmentation is enabled.*

into the TS-QAIC to demonstrate adaptive system scaling. For illustrative purposes, simple signal reconstruction was done in addition to the support recovery.

During the first sense period, the time segmentation is disabled (**TS OFF**) and the threshold is set to the high setting (-66dBm/300kHz) that makes the TS-QAIC blind to the interferers below the threshold, such that the TS-QAIC can successfully detect only the 3 strongest interferers in $4.4\mu s$ with only 8 physical I/Q branches without needing to extend the hardware through time segmentation. Adaptive thresholding adjusts the threshold for the second sense period based on the feedback from the CS information recovery engine that monitors the OMP residual. During the second sense period, the threshold is lowered (-88dBm/300kHz) through adaptive thresholding and TS-QAIC branches are extended to 16 virtual I/Q branches through time segmentation (**TS ON**). Then, all 6 weak and strong interferers are detected successfully in $10.4\mu s$.

5.4.6 TS-QAIC Instantaneous Bandwidth and Hardware Scalability Demonstration

For illustrative purposes, simple signal reconstruction was also done for the results presented here in addition to the support recovery. Fig. 5.14 demonstrates the TS-QAIC wide sensing capability with a 1GHz instantaneous bandwidth. The 1GHz instantaneous bandwidth capability is demonstrated in Fig. 5.14 by reconstructing 4 interferers located at 2.7GHz, 2.72GHz, 2.74GHz, and 3.68GHz. Shown in Fig. 5.15 is an example of the successful detection of 5 interferers located at 2.96GHz, 3GHz, 3.32GHz, 3.34GHz, and 3.36GHz with a 6dB power difference between each of

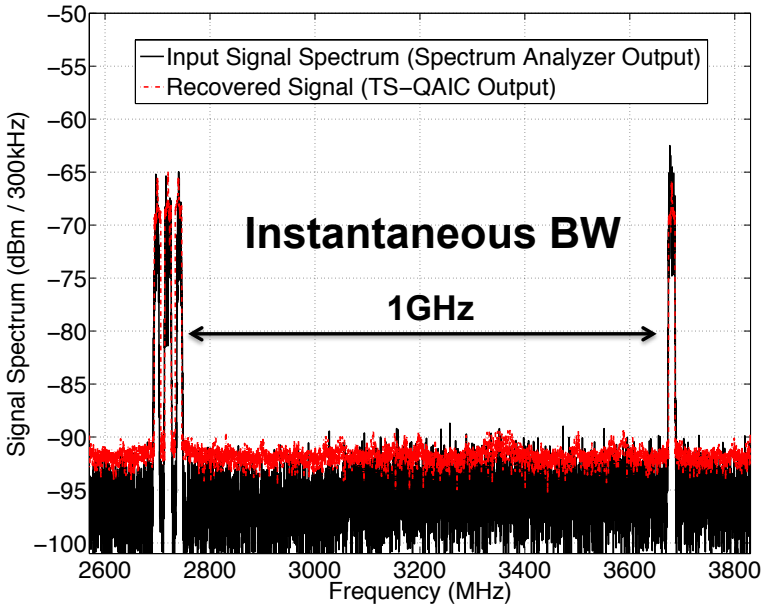

Figure 5.14: *TS-QAIC 1GHz instantaneous bandwidth demonstration with 12 virtual I/Q branches enabled through time segmentation.*

the strong and weak interferers (a 10.5dB difference in the power of weak interferer with respect to the total power of the interferers) enabled by time segmentation.

These measurements also demonstrate TS-QAIC hardware scalability. For the signal reconstruction shown in Fig. 5.14, the 8 physical I/Q branches are extended to 12 virtual through time segmentation and only 80 samples are used to detect 4 interferers over a 1GHz span in 6.4μs, while for the signal reconstruction shown in Fig. 5.15, the 8 physical I/Q branches are extended to 16 virtual through time segmentation and 100 samples are used to detect 5 interferers in 10.4μs.

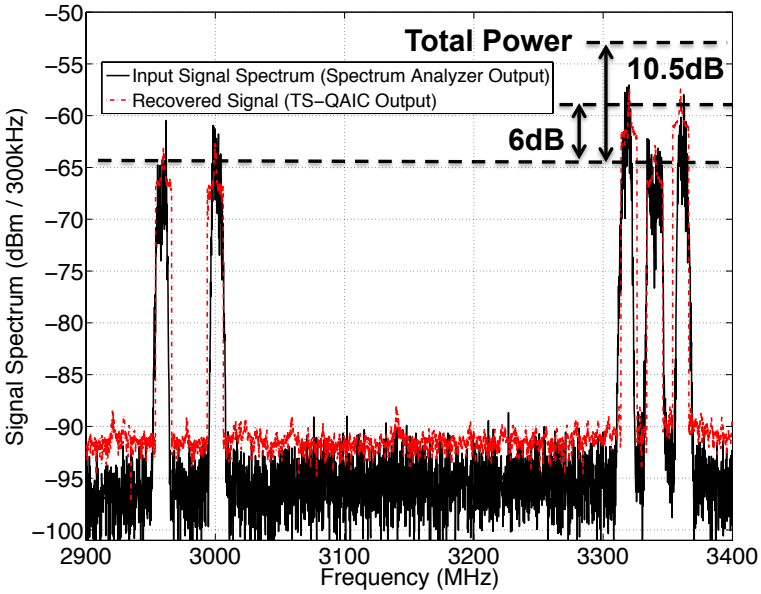

Figure 5.15: *Successful detection of 5 interferers with a 6dB power difference between each of the strong and weak interferers (a 10.5dB difference in the power of weak interferer with respect to the total power of the interferers) with 16 virtual I/Q branches enabled through time segmentation.*

5.5 Performance Summary and Discussion

Shown in Table 5.1 is the measured performance summary of the TS-QAIC [8] compared to that of the QAIC reported in [3,5]. TS-QAIC can rapidly detect 6 interferers in 10.4μs by extending the 8 physical to 16 virtual (effective) I/Q branches through time segmentation, while maintaining the advantages in power consumption and sensitivity that is offered by band-pass CS approaches [3] compared to existing low-pass CS approaches [26, 28].

Currently proposed sub-Nyquist interferer detectors, like the QAIC [3, 5] do not report detecting 6 interferers and it is not possible to detect more interferers by simply increasing the number of samples (i.e. scan time). The QAIC [3] with 8 physical I/Q branches is not able to detect 6

Table 5.1: *TS-QAIC performance summary and comparison*

		[3, 5]	This Work [8]	
CMOS Tech.	[nm]	65	65	
Active Area	[mm^2]	0.428	0.517	
Supply Voltage	[V]	1.1	1.2	
Frequency Range	[GHz]	2.7-3.7	2.7-3.7	
RBW Options	[MHz]	10, 20	10, 20	
PN Seq. Clock Rate	[GHz]	1.26	1.26	
Sensitivity	[dBm]	-68[1]	-70[2]	
Adaptive Thresholding Demonstration		No	Yes	
Time Segmentation Demonstration		No	TS OFF	TS ON
Max Number of Detectable Interferers		3	3	6
Number of Physical Branches		8 I/Q	8 I/Q	8 I/Q
Number of Effective Branches		8 I/Q	8 I/Q	16 I/Q
Measured Power Consumption	[mW]	81[3]	81.2[3]	81.2[3]
Power Est. (w/ PLL & ADC)	[mW]	115	115	115
Scan Time	[µs]	4.4	4.4	10.4
Energy per Scan	[µJ/scan]	0.5	0.5	1.2
Energy per Active Bin	[µJ/active bin]	0.168	0.168	0.2
Rel. Energy per Active Bin		1x	1x	1.2x

[1] Power per active frequency bin for 3 band detection;

[2] Power per active frequency bin for 6 band detection; [3] ADC off-chip

interferers with a target $P_D \geq 90$ and $P_{FA} < 15\%$, while the TS-QAIC can successfully detect 6 interferers with only 8 physical I/Q branches through time segmentation.

The presented system architecture in this chapter, CS TS-QAIC [8], introduces system scalability by using adaptive thresholding and extension of physical hardware through time segmentation. This enables the rapid detection of 6 interferers in a 1GHz span in 10.4μs, while limiting silicon cost and complexity. These features of the TS-QAIC make it an enabling technology for emerging cognitive radio terminals.

5.6 Performance Summary of the Band-pass Compressed Sampling Interferer Detectors and Comparison

Shown in Table. 5.2 is the detailed comparison of the measured performance of the CS QAIC [3,5] and the CS TS-QAIC [8] to the state of the art in integrated compressed sampling spectrum sensors reported in [26, 28]. Shown in Table. 5.3 is the measured performance comparison of the QAIC [3] and the TS-QAIC to the estimated performance of the state-of-the-art compressed sampling spectrum sensors [26, 28], that are scaled to sense a 1GHz span from 2.7 to 3.7GHz with 20MHz RBW with the same assumptions discussed in Section 4.6. The performance comparison shows that band-pass compressed sampling architectures like the QAIC [3, 5] and the TS-QAIC [8] offer energy-efficient spectrum sensing over a wide instantaneous bandwidth compared to the existing low-pass CS spectrum sensors.

Table 5.2: *Comparison of the measured performance of the CS QAIC and the CS TS-QAIC interferer detectors to the state of the art in integrated compressed sampling spectrum sensors*

		[26]	[28]	[3, 5]	*This Work [8]*	
Application		Sub-Nyquist CS Receiver	Sub-Nyquist CS Receiver	Sub-Nyquist CS Interferer Detector	***Time-Segmented Sub-Nyquist CS Rapid Interferer Detector***	
Architecture		Random-Modulation Pre-Integrator CS	Parallel Segmented CS	CS with Quadrature Analog-to-Information Converter	***Time-Segmented (TS) CS with a TS-QAIC***	
System Config.		Low-pass CS	Low-pass CS	Band-pass CS	***Time-Segmented Band-pass CS***	
Signal Type		Multi tone	Multi tone	Multi band	***Multi band***	
CMOS Tech.	**[nm]**	90	90	65	***65***	
Die Area	**[mm^2]**	8.85	0.93	1.96	***0.517 (active area)***	
Supply Voltage	**[V]**	1.5 (A), 1.2 (D)	N/R	1.1	***1.2***	
Frequency Range		100MHz-2GHz	5-500MHz	2.7-3.7GHz	***2.7-3.7GHz***	
Instantaneous BW		1.9GHz	495MHz	1GHz	***1GHz***	
Adaptive Thresholding Demonstration		No	No	No	***Yes***	
Number of Physical Branches		8	8	16 = 8 x I/Q	***16 = 8 x I/Q***	
Number of Effective Branches (m)		8	8	8I/Q	***TS OFF - 8I/Q***	***TS ON - 16I/Q***
RBW Options	**[MHz]**	N/R	5	10, 20	***10, 20***	
PN Seq. Clock Rate	**[GHz]**	4	1.25	1.26	***1.26***	
Sensitivity	**[dBm]**	-64[1]	N/R	-68[2]	***-70[3]***	
Power	**[mW]**	506.4[4,5]	55[4,6]	81[4]	***81.2[4]***	

N/R: Not Reported;
[1] For a single tone detection; [2] Power per active frequency bin for 3 band detection; [3] Power per active frequency bin for 6 band detection;
[4] ADC off-chip; [5] Without output buffers; [6] Estimated ADC power is less than1mW and estimated PLL power is 1mW.

Table 5.3: *Compressed sampling spectrum sensor performances normalized for a 1GHz span from 2.7 to 3.7GHz with a RBW of 20MHz*

		[26]	[28]	[3, 5]	*This Work [8]*			
	Normalized for 2.7-3.7GHz operation with 20MHz RBW							
Scaled PN Seq. Clock for LFSR	**[GHz]**	*10.22*	*10.22*	*1.26*	***1.26***	***1.26***	***1.26***	***1.26***
Max Number of Detectable Signals		*3*	*3*	*3*	***3***	***4***	***5***	***6***
# of CS Measurements		*29*	*29*	*8 complex*	***8 complex***	***12 complex***	***16 complex***	***16 complex***
Branch Sampling Rate	**[MSps]**	*20*	*180*	*20*	***20***	***20***	***20***	***20***
Power Est. (w/ PLL & ADC)	**[mW]**	*607*	*1,056*	*115*	***115***	***115***	***115***	***115***
Scan Time	**[µs]**	*4.4*	*4.4[1]*	*4.4*	***4.4***	***6.4***	***10.4***	***10.4***
Energy per Scan	**[µJ/scan]**	*2.7*	*4.6*	*0.5*	***0.5***	***0.74***	***1.2***	***1.2***
Energy per Active Bin	**[µJ/active bin]**	*0.9*	*1.54*	*0.168*	***0.168***	***0.185***	***0.24***	***0.2***
Rel. Energy per Active Bin		*5.4x*	*9.2x*	*1x*	***1x***	***1.1x***	***1.43x***	***1.2x***

[1] Parallel segmented CS architecture is used and 9 samples collected from each path.

Chapter 6

Challenges and Trade-offs Associated with the Design of Compressed Sampling Rapid Interferer Detectors

In this chapter, the challenges and trade-offs associated with the design of compressed sampling architectures are discussed. The pseudorandom noise (PN) mixer, which is the key circuit block of the interferer detector for rapidly capturing the wide instantaneous BW, is analyzed in terms of the design choices and effects of its operation on the instantaneous dynamic range of analog-to-information converters.

6.1 Instantaneous Bandwidth versus Instantaneous Dynamic Range Trade-off of Analog-to-Information Converters

Analog-to-information converters consisting of low-pass and band-pass compressed sampling architectures, shown in Fig. 6.1 and discussed in greater detail in Chapter 3 and Chapter 4 respectively, are well-suited for capturing a wide instantaneous bandwidth by ADCs operating at a sub-

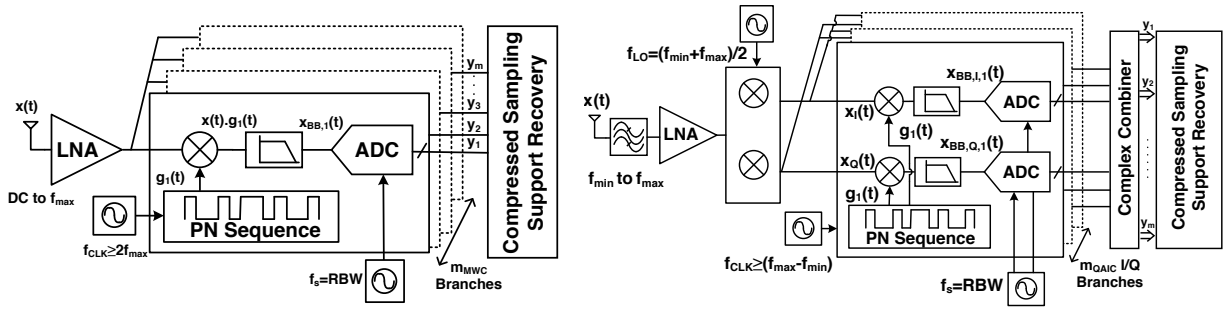

(a) (b)

Figure 6.1: *Compressed sampling analog-to-information converter architectures; (a) Low-pass [23, 42, 43], (b) Band-pass [3–5].*

Nyquist aggregate sampling rate. The sub-Nyquist aggregate sampling rate is proportional to the information bandwidth (a.k.a. signal bandwidth) by breaking the main limitation of the traditional Nyquist-rate sampling approaches. As discussed in Chapter 3, the information bandwidth, $K_0 \cdot RBW$, is much smaller than the instantaneous signal bandwidth, $N_0 \cdot RBW$.

Compressed sampling rapid interferer detectors employing analog-to-information converters (AICs) have an intrinsic trade-off between instantaneous dynamic range and instantaneous bandwidth. The instantaneous bandwidth of an AIC is defined its *Span*, over which few signals (K_0 signals) can be successfully and rapidly detected, while meeting the target detection and false alarm probabilities (e.g. $P_D \geq 90\%$ and $P_{FA} < 15\%$ for a QAIC [3, 5] and a TS-QAIC [8]). The instantaneous dynamic range of an AIC is defined as the ability to detect a weak signal in the presence of a strong signal or strong signals over a wide instantaneous bandwidth (a.k.a. *Span*), while meeting the target P_D and P_{FA}. While CS AICs offer short scan times on the order of 10s of μs with low energy-consumption over a wide instantaneous bandwidth equal to the *Span*, their instantaneous dynamic range is limited compared to traditional spectrum scanning or sensing solutions.

Traditional sweeping spectrum scanners offer a large dynamic range over a small instantaneous bandwidth as shown in Fig. 1.5, where the instantaneous bandwidth for sweeping spectrum scanners is equal to the RBW.

The instantaneous dynamic range of an AIC is limited mainly by noise, nonlinear distortion, and linear impairments. On the high end, it is limited by the strongest signal that can be detected without degrading the performance due to intermodulation distortion (IMD) products or compression. On the low end, it is limited by the sensitivity which is set by noise folding due to the PN mixing to instantaneously capture a wide 1GHz bandwidth.

For band-pass compressed sampling architectures, like a QAIC [3, 4] and a TS-QAIC [8], the instantaneous dynamic range might also be limited by linear circuit impairments such as I/Q phase and gain imbalance. The linear impairments are modeled and discussed for compressed sampling QAIC complex-domain support recovery in Chapter 4 [4]. The instantaneous dynamic range of a QAIC is evaluated with the detection and the false alarm probabilities of a weak signal in the presence of two strong signals. The QAIC system without impairment compensation delivers an 11dB instantaneous dynamic range, while it is able to deliver an 18dB instantaneous dynamic range with linear impairment compensation as demonstrated by Fig. 4.17 in Chapter 4 [3].

In the presence of a weak and a strong signal, the instantaneous dynamic range calculation of a TS-QAIC operating over a 1GHz span with an NF of 18dB mapped to an 8-bit A/D range is shown as an example in Fig. 6.2.

The effect of PN mixing on the instantaneous dynamic range of AICs is investigated and dis-

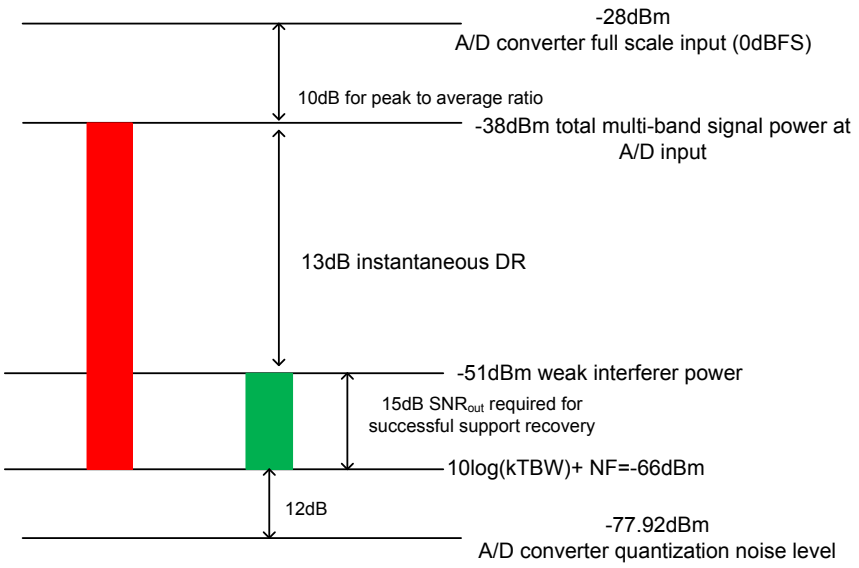

Figure 6.2: *The instantaneous dynamic range calculation of a TS-QAIC operating over a 1GHz span with an NF of 18dB mapped to an 8-bit A/D range.*

cussed in this chapter. We mainly focus on the following first order factors after defining the design parameters of PN mixers:

- Noise analysis of PN mixers including the impact of noise folding and the number of samples on the sensitivity level of AICs
- Linearity analysis of PN mixers including intra-bin and inter-bin spectrum test cases

We note that there are also the following second order factors that have an impact on the instantaneous dynamic range of AICs:

- Effect of automatic gain control (AGC)
- Unique spectral properties of the PN sequences that change from bin-to-bin and/or from branch-to-branch

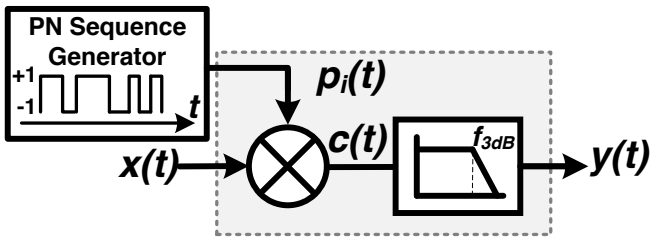

Figure 6.3: *Block diagram of a PN mixer followed by a low-pass filter in AICs.*

6.2 Analysis of Pseudorandom Noise Mixers in Analog-to-Information Converters

A PN mixer followed by a low-pass filter employed in AICs is shown in Fig. 6.3. Even though the low-pass filter is used as an anti-aliasing filter before the sampling, it is considered as a part of the PN mixer for the analysis in this chapter. We note that PN mixing analysis is mainly presented in contrast to mixing with a square LO as a benchmark.

6.2.1 PN Mixer Design Parameters for Analog-to-Information Converters

Design parameters of the PN mixers such as chip duration and sequence period are defined in this chapter in relation to compressed sampling spectrum sensor parameters like RBW and instantaneous bandwidth. A PN sequence consists of a deterministic sequence of pulses that repeats itself after its period. The period of a PN sequence T_p is the repetition window of the sequence bits. The relation between the AIC sensing parameter RBW and the period of a PN sequence T_p is given by (6.1), where f_{CLK} is the PN sequence generator clock frequency and L is the length of a PN sequence [47]. The chip duration T_c of a PN sequence $p_i(t)$ shown in Fig. 6.4(a) is the smallest pulse width of the sequence that represents only one bit in the repetition window. The chip duration T_c

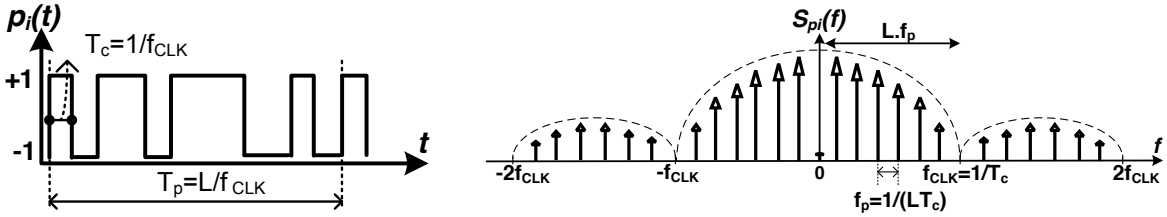

(a) (b)

Figure 6.4: *A PN sequence driving the mixer with its design parameters; (a) PN sequence time-domain waveform, (b) PN sequence spectrum.*

is defined in terms of the PN sequence generator clock frequency as $1/f_{CLK}$.

$$T_p = L \cdot T_c = L/f_{CLK} = 1/RBW \tag{6.1}$$

Each path of the AIC is driven by a unique PN sequence $p_i(t)$ for incoherent measurements. The Fourier expansion of a T_p-periodic real $p_i(t)$ is given in (6.2), where f_p is equal to $1/T_p$ and also the RBW for CS spectrum sensors.

$$p_i(t) = \sum_{n=-\infty}^{\infty} b_{i,n}\, e^{j2\pi n f_p t} \tag{6.2}$$

With the assumption of an maximal-length sequence (m-sequence) as the PN sequence driving the mixer, the coefficients $b_{i,n}$ are calculated by evaluating the integral in (6.3) [4, 42, 47].

$$\begin{aligned} b_{i,n} &= \frac{1}{T_p}\int_0^{T_p} p_i(t)\cdot e^{-j\frac{2\pi}{T_p}nt}\cdot dt \\ b_{i,-n} &= \frac{1}{T_p}\int_0^{T_p} p_i(t)\cdot e^{j\frac{2\pi}{T_p}nt}\cdot dt = b_{i,n}^{*} \end{aligned} \tag{6.3}$$

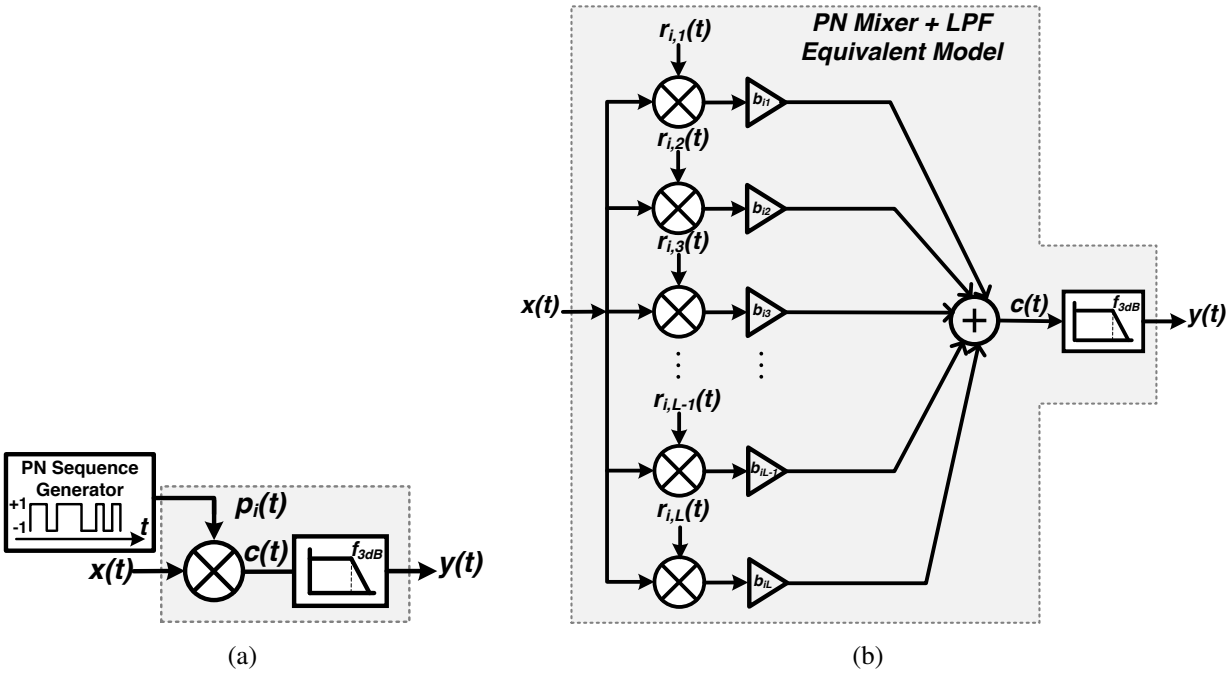

Figure 6.5: *(a) Block diagram of a PN mixer followed by a low-pass filter in AICs. (b) The equivalent multi-path mixers model of a PN mixer derived from its Fourier series followed by a low-pass filter. The multi-path mixers model also illustrates the wide instantaneous bandwidth capturing capability of the AICs.*

Based on its Fourier series, the equivalent multi-path mixers model of a PN mixer followed by a low-pass filter is shown in Fig. 6.5(b). The PN mixer block shown in Fig. 6.5(a) of the analog-to-information converters's i^{th} branch is represented as the summation of the outputs of the L individual I/Q mixers driven by L harmonically related complex sinusoids $r_{i,n}(t)$ where n runs from 0 to L-1, followed by weighted gain stages ($b_{i,n}$). The output sum of the multi-path mixers ($c(t)$) is filtered by a low-pass filter with an impulse response of $h(t)$. For the signal path analysis, the complex-domain LO signal driving each mixer path is $r_{i,n}(t) = e^{j2\pi\left(\frac{n}{L \cdot T_c}\right)t}$. The equivalent multi-path mixers model further illustrates the wide instantaneous bandwidth capturing capability of compressed sampling spectrum sensors. Weighted gain stages $b_{i,n}$ represent the weights of an m-

sequence with a spectrum $S_{pi}(f)$ with a length L and $f_p = f_{CLK}/L$ which is equal to the RBW [47] given in (6.4).

$$S_{pi}(f) = \left[\sum_{\substack{k=-\infty \\ r\neq 0}}^{\infty} \delta(f - kf_p)\right] \frac{L+1}{L^2}\left(\frac{\sin \pi f/f_{CLK}}{\pi f/f_{CLK}}\right)^2 + \frac{1}{L^2}\delta(f); \tag{6.4}$$

Output $y(t)$ and its Fourier transform $Y(f)$ is given in (6.5). Mixing the input $x(t)$ with each of the harmonically related complex sinusoids followed by weighted gain stages and then summing the outputs of the multi-path mixers represents the PN mixing that generates a linear combination of copies of the input spectrum $X(f)$ shifted by multiples of $f_p = RBW$. The signal power in each copy of the input spectrum is reduced by a factor proportional to $(L+1)/L^2$, while the total signal power which is integrated over the entire spread spectrum stays the same. To demonstrate the PN mixing effect on the input spectrum, spectra of the key signals is shown for an AIC in Fig. 6.6. The multi-path mixing operation spreads the spectrum and captures the wideband spectrum instantaneously by folding into each bin the signal information from all bins.

$$\begin{aligned} y(t) &= \left(\sum_{n=0}^{L-1} b_{i,n}\left[x(t)\cdot r_{i,n}(t)\right]\right) * h(t) \\ y(t) \xrightarrow{\mathscr{F}} Y(f) &= \left(\sum_{n=0}^{L-1} b_{i,n}\left[X(f) * R_{i,n}(f)\right]\right)\cdot H(f) \end{aligned} \tag{6.5}$$

A low-pass filter with a 3-dB cut-off frequency of $f_{3dB} = 1/2\,(L\cdot T_c)$ following the PN mixer in AICs is used to limit the bandwidth to the $RBW/2$ before sampling. After low pass filtering, the

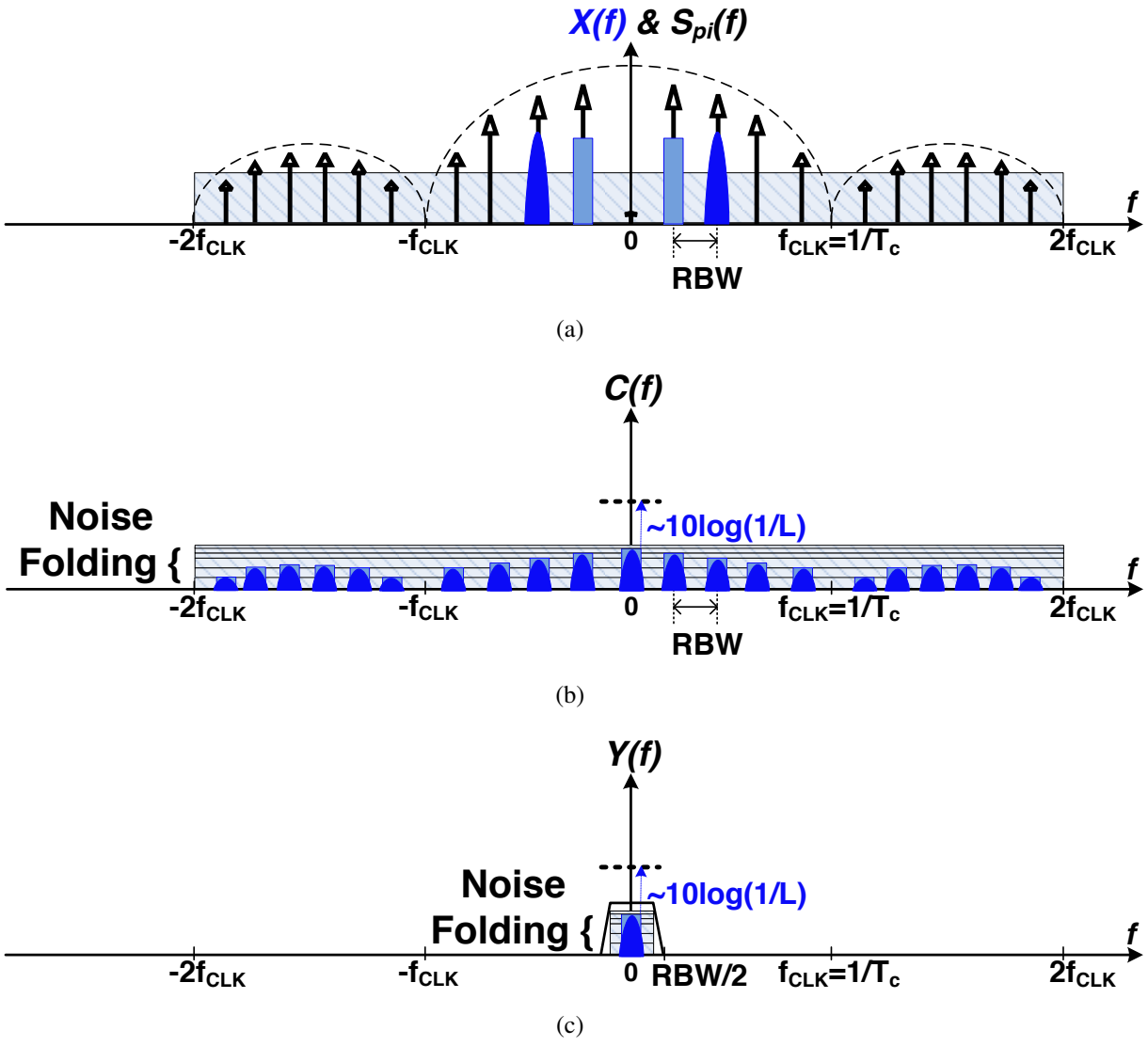

Figure 6.6: *Spectra of the key signals in the compressed sampling spectrum sensor employing an AIC; (a) The input signal spectrum, $X(f)$, and the PN sequence spectrum, $S_{pi}(f)$, (b) The output of the PN mixer, $C(f)$, (c) The output of the low pass filter following the PN mixer, $Y(f)$.*

baseband signal is obtained that contains one replica of the folded spectrum which is then sampled and converted into the digital domain for CS support recovery [3, 42].

6.2.2 PN Mixer Noise Analysis for Analog-to-Information Converters

Noise folding: The effect of noise folding in PN mixers [67] on the effective sensitivity level is discussed in this section. *SNR* degradation with respect to mixing with a square LO is illustrated in Fig. 6.7. At the output of the low pass filter following the PN mixer, the total signal power is reduced by an amount that is proportional to the length of the PN sequence due to spreading the spectrum, while the noise power stays the same due to the noise folding factor proportional to the length of the PN sequence.

The effective sensitivity level, ESL, is given in (6.6), where NBW_{CS} is the effective noise bandwidth of compressed sampling AICs that takes into account the noise folding effect, NF_{sq} is the noise figure of the AIC if the LO port of the PN mixer is driven by a square wave at a rate of $f_{CLKsq} = k_i.RBW$, and SNR_{out} is the required signal to noise ratio at the output for successful support recovery that satisfies a target P_D and P_{FA} based on the deployment scenario requirements.

$$ESL = 10\log\left(NBW_{CS}\right) + NF_{sq} + SNR_{out} \tag{6.6}$$

The effective noise bandwidth to account for the noise folding, NBW_{CS}, tracks the instantaneous bandwidth of the AICs and is defined by $L \cdot RBW$ which scales with the span. For a given span, if the RBW is halved, L needs to be doubled. Therefore, the NBW_{CS} remains the same. In essence, the impact of noise folding will not reduce when reducing RBW but will reduce only when reducing

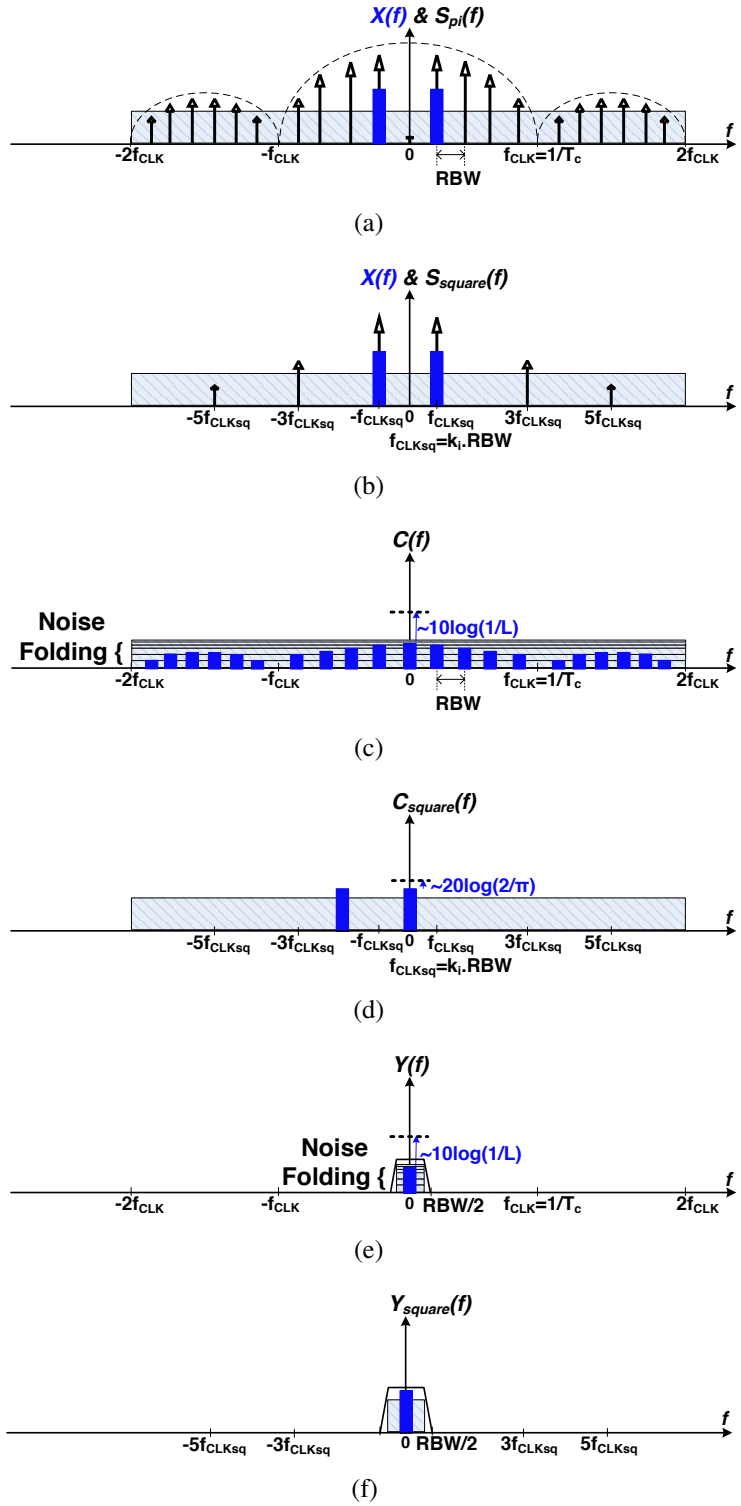

Figure 6.7: *Conceptual illustration of the noise folding and SNR degradation due to PN mixing in AICs compared to mixing with a square LO. Spectra of the key signals; (a) The input signal spectrum, $X(f)$, and the PN sequence spectrum, $S_{pi}(f)$, (b) The input signal spectrum, $X(f)$, and the square LO spectrum, $S_{square}(f)$, (c) The output of the PN mixer, $C(f)$, (c) The output of the square LO mixer, $C_{square}(f)$, (d) The output of the low pass filter following the PN mixer, $Y(f)$, (c) The output of the low pass filter following the square LO mixer, $Y_{square}(f)$.*

the span. The band-pass CS architectures have a smaller signal bandwidth after downconversion that results in reduced noise folding. Limiting the signal bandwidth with downconversion thus allows improved sensitivity and better instantaneous dynamic range performance compared to low-pass CS architectures.

Effect of the number of samples on the sensitivity: Doubling the number of samples should improve the sensitivity level of an AIC by 3dB. There is a fixed trade-off between the number of samples used for support recovery and the scan time. The effect of the number of samples on the sensitivity can be demonstrated with the P_D and P_{FA} measurements for varying power levels per band for K_0 interferers by doubling the number of samples n_s to be used in the support recovery.

With the assumption of at least $2K_0$ samples needed to satisfy the target P_D and P_{FA} at the effective sensitivity level, the number of samples required to improve the sensitivity level by the noise folding factor at the expense of increased scan time is $n_s = 2K_0 \cdot 2^k$, where $k \geq (10\log L)/3$ for $k \in \mathbb{Z}^+$.

As an example scenario, the calculated number of samples n_s for $K_0 = 1$ required to improve the effective sensitivity level by an amount sufficient to offset the m-sequence noise folding factor of 17.99dB is 128. Shown in Fig. 6.2, the calculated effective sensitivity level is -51dBm/10MHz, and if 128 samples are used for support recovery then the expected sensitivity level is around -69dBm/10MHz for a target P_D and P_{FA}.

Table 6.1: *System parameters of a PN mixer linearity characterization in a TS-QAIC*

Linearity Test System Parameters			
Tone Spacing	Intra-bin	Inter-bin	
# of Tones	2	2	
Bin Locations	Same bin	Adjacent bins	Nonadjacent bins
Tone Locations	$k_i RBW+\delta_1$, $k_i RBW+\delta_2$	$k_i RBW+\delta_1$, $k_{i+1} RBW+\delta_2$	$k_i RBW+\delta_1$, $k_r RBW+\delta_2$
Sequence Type	Maximal-length/Gold sequence	Maximal-length/Gold sequence	
Number of Effective Branches	TS ON - 16 I/Q	TS ON - 16 I/Q	

6.2.3 PN Mixer Linearity Analysis for Analog-to-Information Converters

We analyze the linearity of a PN mixer with two kinds of two-tone test cases for AICs called *intra-bin* and *inter-bin spectrum* test cases. Table 6.1 shows an example of the system parameters to characterize the linearity of a PN mixer in a TS-QAIC.

Intra-bin spectrum test: The *intra-bin spectrum* test shown in Fig. 6.8 characterizes the narrowband linearity of the AIC that offers a wide instantaneous bandwidth. Two equal-power tones are located at $k_i \cdot RBW + \delta_1$ and $k_i \cdot RBW + \delta_2$ respectively, where $1 \leq k_i \leq N_0$, in the same spectrum bin out of N_0 bins in the span. Two tones are mixed with the specific PN sequence spectrum component located at the $k_i \cdot RBW$ and downconverted to baseband locations of δ_1 and δ_2. These two tones are also spread into all the N_0 spectrum bins by mixing with all the L PN sequence spectrum components. The low-pass filter following the mixing stage has a 3-dB equal to the $RBW/2$, which filters out the copies of the two tones in the other bins of the interest spectrum range. The two tones are located at the input of the PN mixer in one of the narrowband RBW-wide bins out of all possible bins in a span of $N_0 \cdot RBW$. After mixing with the PN sequence and low pass filtering, the two tones and their IMD products, at the output, are also located in the baseband narrowband

RBW-wide bin. The intra-bin spectrum linearity test case demonstrates the narrowband input to narrowband output mapping of the PN mixing that is similar to a traditional square LO mixing.

Inter-bin spectrum test: The *inter-bin spectrum* test shown in Fig. 6.9 and Fig. 6.10 characterizes the wideband linearity of the AIC with a wide instantaneous bandwidth. Two equal-power tones are located in any of the two bins out of N_0 locations over the span. Two tones located in two different spectrum bins over the wide span are mixed with their specific PN sequence spectrum components and downconverted to baseband. The two tones are also spread over into all the N_0 spectrum bins by mixing with all the L PN sequence spectrum components. The low-pass filter following the mixing stage has a 3-dB equal to the $RBW/2$, which filters out the copies of the two tones in the other bins of the spectrum range of interest.

The inter-bin spectrum linearity test has two possible scenarios. One of the possible scenarios is that the two tones at the input can be placed in adjacent bins (Fig. 6.9) and the tone locations will be $k_i \cdot RBW + \delta_1$ and $k_{i+1} \cdot RBW + \delta_2$ respectively. Another possible scenario is that they can be placed in nonadjacent bins (Fig. 6.10) with N_0 possible locations and their locations will be $k_i \cdot RBW + \delta_1$ and $k_r \cdot RBW + \delta_2$ respectively. These two tones are located at the input of the PN mixer in a wideband configuration in any of the two *RBW*-wide bins, and at the baseband output, after mixing with the PN sequence followed by low-pass filtering, the two tones and their IMD products are folded into the same narrow-band *RBW*-wide bin. The two fundamental tones are located at baseband locations, δ_1 and δ_2, while the two IM3 products are located at baseband locations, $(2\delta_1 - \delta_2)$ and $(2\delta_2 - \delta_1)$.

The inter-bin spectrum linearity test demonstrates the wideband input to narrowband output

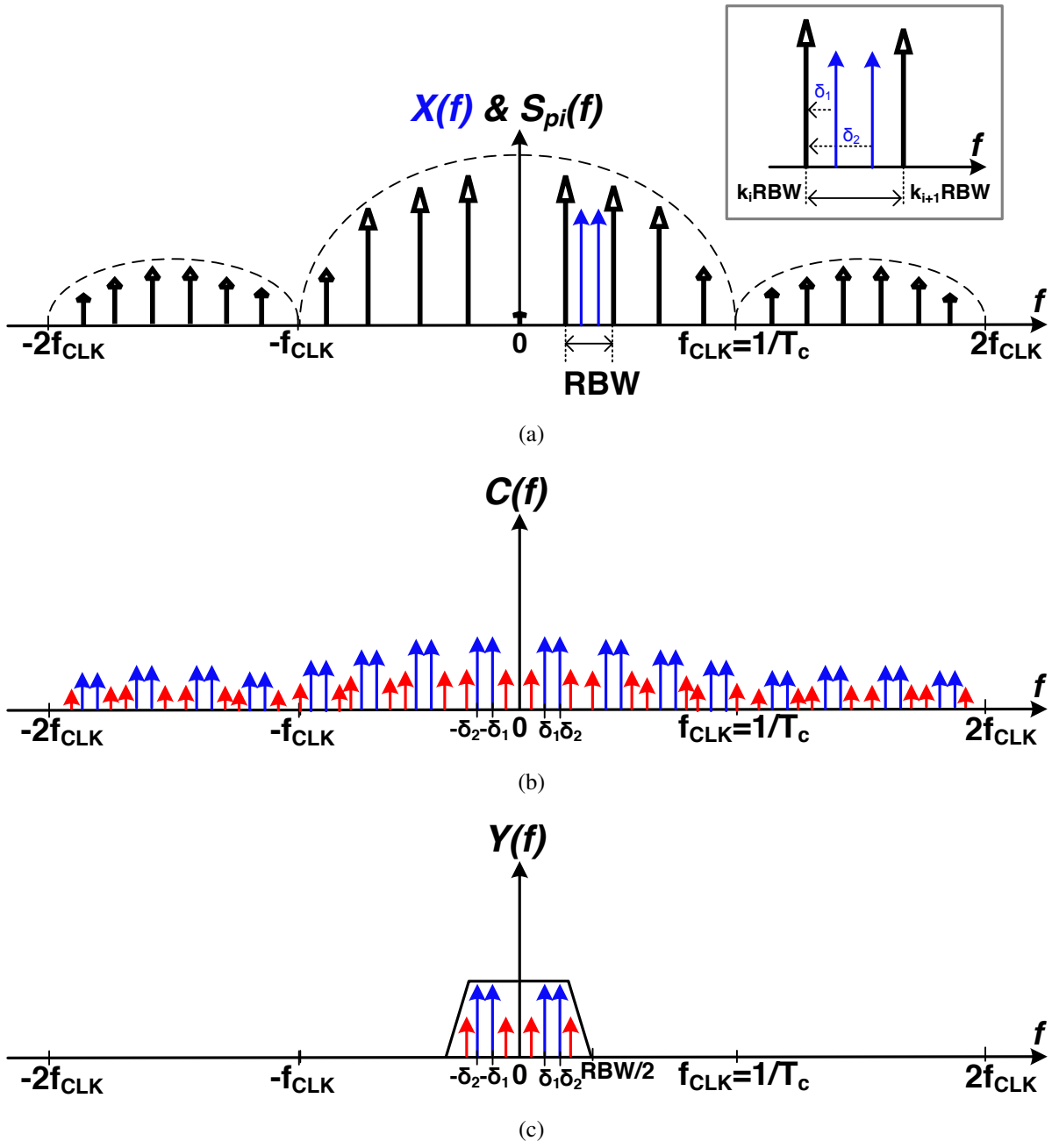

Figure 6.8: *Spectra of the key signals for the **intra-bin** spectrum linearity test of a PN mixer in an AIC (Fig. 6.3); (a) The input signal spectrum, $X(f)$, and the PN sequence spectrum, $S_{pi}(f)$, (b) The output of the PN mixer, $C(f)$, (c) The output of the low pass filter following the PN mixer, $Y(f)$.*

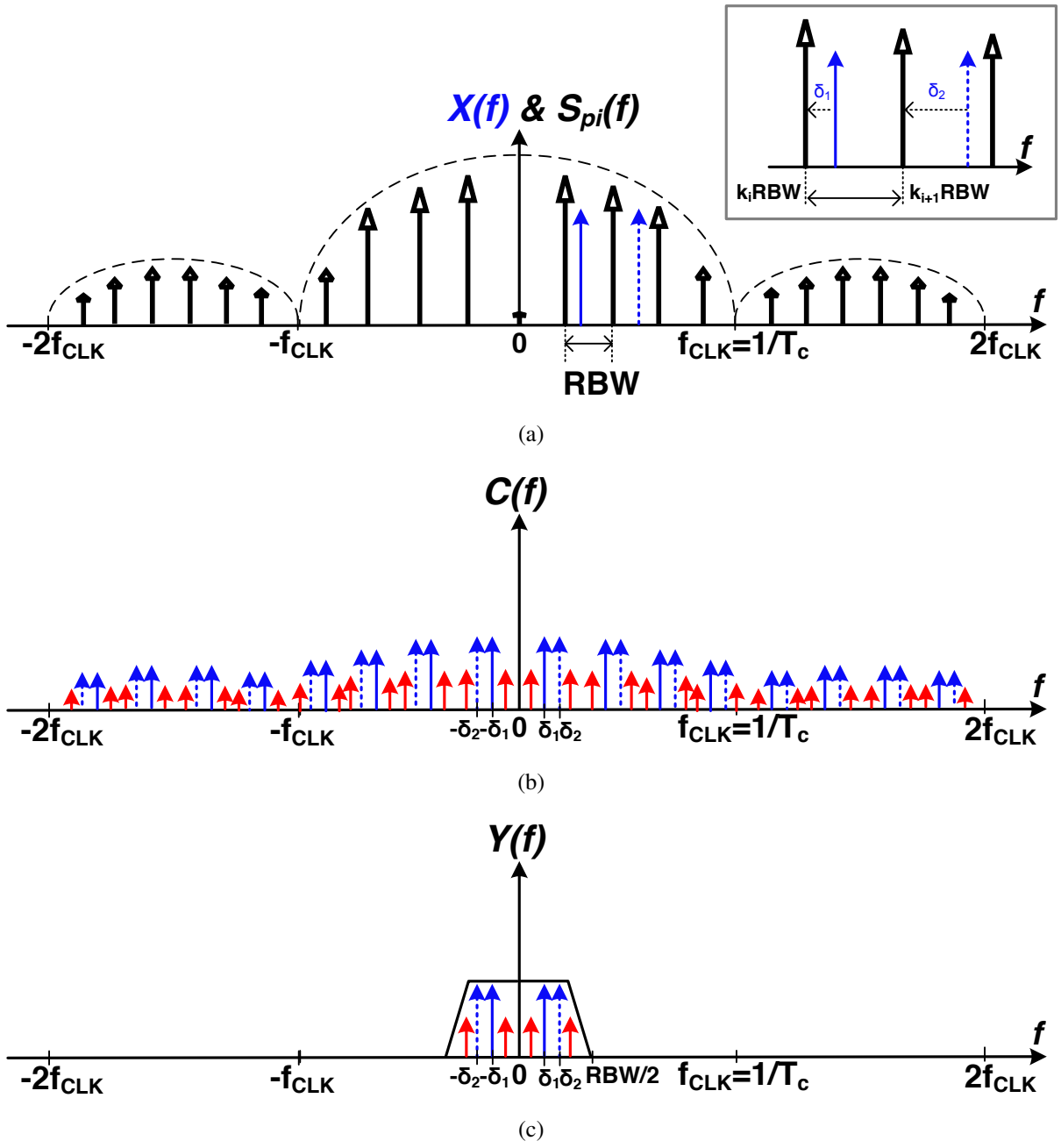

Figure 6.9: *Spectra of the key signals for the **inter-bin** spectrum linearity test of a PN mixer in an AIC (Fig. 6.3), two input tones are located in **adjacent bins**; (a) The input signal spectrum, $X(f)$, and the PN sequence spectrum, $S_{pi}(f)$, (b) The output of the PN mixer, $C(f)$, (c) The output of the low pass filter following the PN mixer, $Y(f)$.*

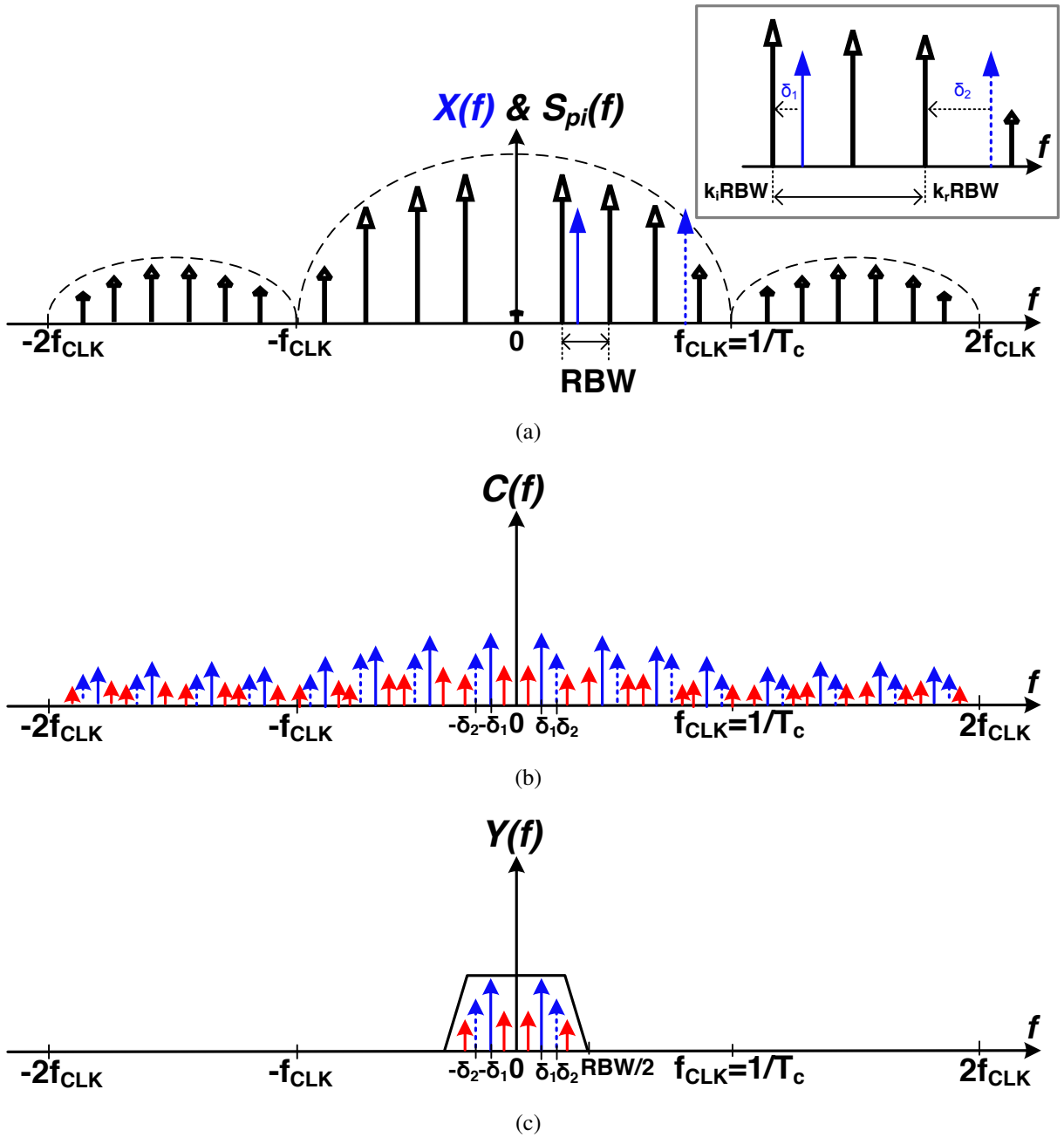

Figure 6.10: *Spectra of the key signals for the **inter-bin** spectrum linearity test of a PN mixer in an AIC (Fig. 6.3), two input tones are located in **nonadjacent bins**; (a) The input signal spectrum, $X(f)$, and the PN sequence spectrum, $S_{pi}(f)$, (b) The output of the PN mixer, $C(f)$, (c) The output of the low pass filter following the PN mixer, $Y(f)$.*

mapping of the PN mixing that comes from the multi-LO type spectral properties of the PN sequences. This unique feature of the PN mixer makes it a key feature of AICs, enabling them to rapidly capture a wide instantaneous bandwidth.

6.3 Measurement Results

To demonstrate some of the challenges and trade-offs associated with CS rapid interferer detectors including the impact of PN mixing on the instantaneous dynamic range performance of AICs, the TS-QAIC chip is used as an example benchmark for the measurements. For the sake of comparison, the TS-QAIC branches are characterized for RF performance with square LOs driving the PN mixers.

6.3.1 TS-QAIC Instantaneous Dynamic Range versus Instantaneous Bandwidth Trade-Off

The intrinsic trade-off of compressed sampling spectrum sensors between the instantaneous dynamic range and instantaneous bandwidth is discussed in Section 6.1. In Chapter 5, the TS-QAIC measurement shown in Fig 5.14 demonstrates the 1GHz-wide instantaneous bandwidth capability of the CS interferer detector.

The instantaneous dynamic range of a TS-QAIC system is defined as the ability to detect a weaker interferer in the presence of a stronger interferer over a 1GHz-wide instantaneous bandwidth. The instantaneous dynamic range calculation of the TS-QAIC mapped to an 8-bit A/D

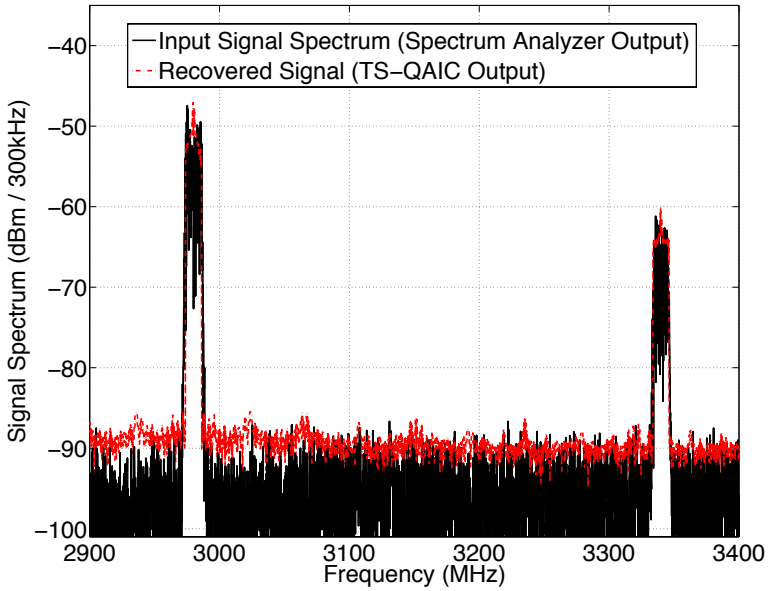

Figure 6.11: *Measured 2-band instantaneous dynamic range of the TS-QAIC with the 8-bit A/D sampling system.*

range used for measurements is shown in Fig. 6.2. The measured 2-band signal reconstruction with a 13dB instantaneous dynamic range is demonstrated in Fig. 6.11 and this measurement confirms the calculation shown in Fig. 6.2 [3].

6.3.2 Effect of Number of Samples on the TS-QAIC Sensitivity Level

Fig. 6.12 demonstrates the effect of the number of samples n_s on the TS-QAIC sensitivity level. Shown in Fig. 6.12 when time segmentation is disabled (**TS OFF**), each of the measured P_D and P_{FA} curves for varying power levels per band for $K_0 = 1$ interferer are obtained by doubling the number of samples for n_s=64, 128, 256, and 512. To report the measured P_D and P_{FA}, 80 experiments are performed for each power level per band for a different number of samples. The effective

[3] We note that if the measurement system is migrated to an 11-bit A/D sampling system, it would be possible to demonstrate a 25dB instantaneous dynamic range of TS-QAIC over a 1GHz instantaneous bandwidth as calculated based on the sensitivity and the strongest signal that can be detected by the CS TS-QAIC prototype.

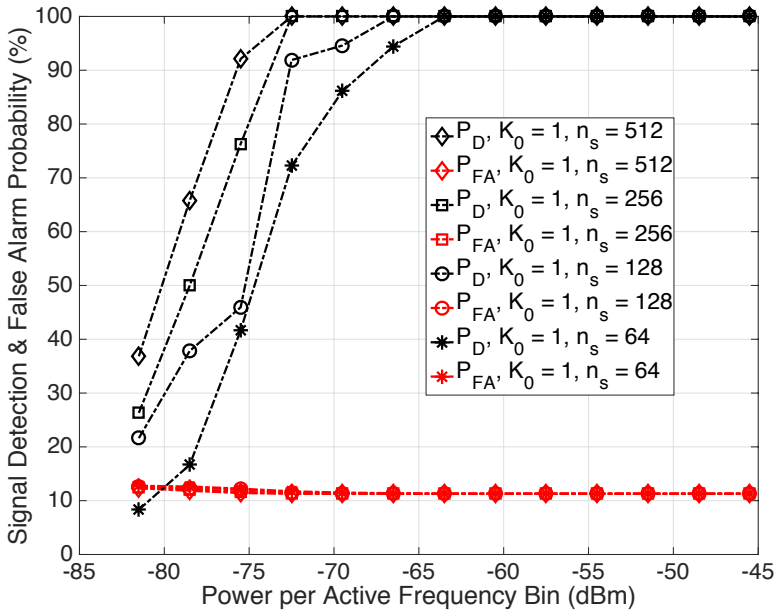

Figure 6.12: *The effect of number of samples on the TS-QAIC sensitivity level is demonstrated with the measured P_D and P_{FA}.*

sensitivity level (*ESL*) calculated in Section 6.2.2 and shown in Fig. 6.2 is -51dBm/10MHz for the PN sequence noise folding factor of 17.99dB and the required SNR_{out} of 15dB for successful support recovery. As shown in Fig. 6.12, when 128 samples are used for complex-domain support recovery, the sensitivity level is -69dBm/10MHz with an improvement of 18dB compared to the effective sensitivity level for a P_D of 95%.

Measured sensitivity levels that correspond to the measured detection probability P_D with 2σ ($\approx 95\%$) and 3σ ($\approx 99.7\%$) as well as the number of samples required to obtain those measured sensitivity levels at the expense of the scan time are reported in Table. 6.2.

Table 6.2: *The measured sensitivity levels and scan times reported for n_s=64, 128, 256, and 512 for the measured P_D with 2σ (≈ 95%) and 3σ (≈ 99.7%)*

	P_D with 2σ (P_D of 95%)	P_D with 3σ (P_D of 99.7%)	TS OFF
Number of Samples	Sensitivity Level (dBm/10MHz)	Sensitivity Level (dBm/10MHz)	Scan Time (μs)
64	-66	-63	3.6
128	-69	-66	6.8
256	-73	-72	13.2
512	-74	-72	26

6.3.3 TS-QAIC PN Mixing Noise Measurements

The noise folding impact of PN mixing on the TS-QAIC performance is demonstrated in terms of the SNR degradation compared to a traditional square LO mixing. Each measurement is performed for I1, I6, and I7 branches of the TS-QAIC to illustrate the effect of the spectral properties of an m-sequence and two unique gold sequences compared to a square LO.

TS-QAIC conversion gain for a square LO, an m-sequence and two unique gold sequences: The TS-QAIC conversion gain is measured and shown as referred to the input frequency range of 2.7-3.7GHz in Fig. 6.13 for the three different branches I1, I6, and I7. Measurement results shown in Fig. 6.13(a) and Fig. 6.13(b) are for the two sets of unique PN sequences, $g_j(t)$ and $g_k(t)$ respectively, that form the optimal sensing matrix ϕ_1. The PN mixer of the I1 branch is driven by a square LO as the comparison reference point and then switched to an m-sequence, while the PN mixers of the I6 and I7 branches are driven by two unique gold sequences with different spectral properties. For the m-sequence and the two unique gold sequences operating at a 1.26GHz rate with a length of 63 for a 20MHz RBW, the conversion gain is measured with an RF tone sweeping the 2.7 to 3.7GHz range with 20MHz steps, while the f_{LO} and f_{CLK} are set to 3.2GHz and 1.26GHz respectively. To illustrate the same 20MHz RBW effect for the PN mixer driven by a square LO,

the conversion gain is measured with an RF tone sweeping the 2.7 to 3.7GHz range with 20MHz steps, while the f_{LO} is set to 3.2GHz and f_{CLK} is swept from $\pm$20MHz to $\pm$500MHz with 20MHz steps to cover the 1GHz spectrum range of interest.

As shown in Fig. 6.13, the measured typical gain of a TS-QAIC I1 branch driven by a square LO is 32dB with an 18.3dB NF, whereas the measured typical gain of a TS-QAIC I1 branch driven by an m-sequence is 18.2dB with a 13.8dB degradation in SNR due to the noise folding (13.8dB conversion loss due to the spectrum spreading). For I6 and I7 branches that are driven by two unique gold sequences, the conversion gain from bin-to-bin differs significantly due to the spectral properties of the gold sequences. On the other hand, for the I1 branch that is driven by an m-sequence, there are not any significant fluctuations in the conversion gain from bin-to-bin since m-sequences typically have uniform spectrum.

TS-QAIC SNR degradation due to PN mixing The SNR degradation is demonstrated with a measurement that shows the output spectrum of the I1, I6, and I7 branches with a baseband tone at 2.5MHz. For this measurement, the RF input tone at 3.3425GHz is mixed with a square LO and then with an m-sequence at the PN mixer of the I1 branch and two unique gold sequences at PN mixers of I6 and I7 branches. The RF input tone is downconverted to baseband with a square LO and a spectral component of the m-sequence or gold sequences that corresponds to 140MHz following a 3.2GHz I/Q downconversion stage. The measured baseband output spectrum is shown for this single tone RF input for a square LO and all three of the mixing sequences with a length of 63 from the time-segmented PN sequence set *k* respectively in Fig. 6.14. The output SNR of the I1 branch is degraded by 13.8dB for the m-sequence, showing a close correspondence with

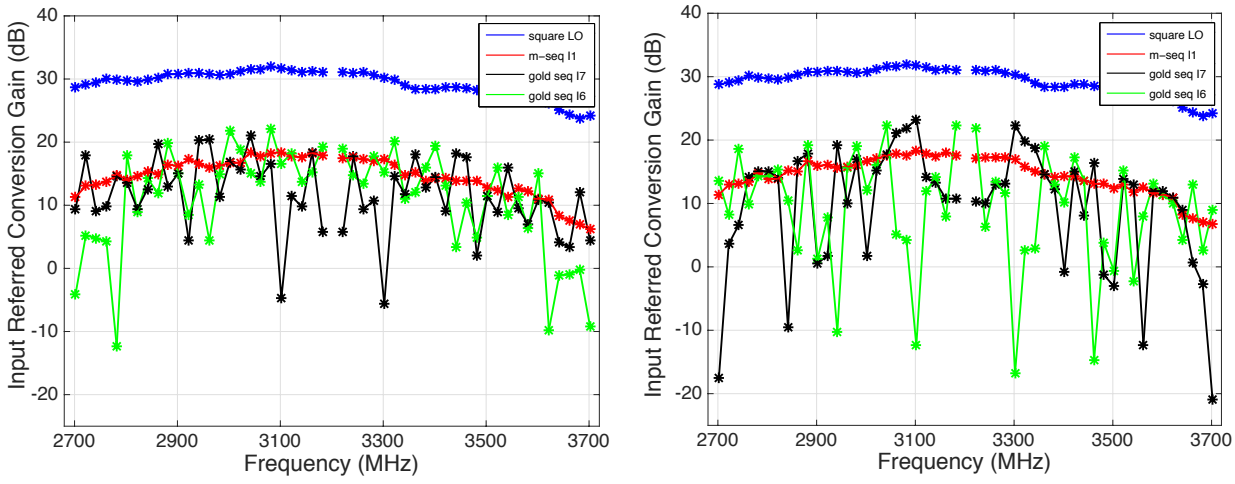

Figure 6.13: *Input referred TS-QAIC conversion gain for I1, I6, and I7 branches. The PN mixer of the I1 branch is driven by a square LO or an m-sequence, while PN mixers of the I6 and I7 branches are driven by two unique gold sequences. Results are reported for the two sets of unique PN sequences ($g_{j/k}(t)$) that form the optimal sensing matrix ϕ_1; (a) Time-segmented PN sequence set j, $g_j(t)$, (b) Time-segmented PN sequence set k, $g_k(t)$.*

the theoretical analysis in Section 6.2.2, 10.2dB for the I7 gold sequence, and 26dB for the I6 gold sequence compared to mixing with a 140MHz square LO. The measurement result shown in Fig. 6.14 further demonstrates the concept of noise folding in PN mixers illustrated in Fig. 6.7. The signal power is reduced by an amount that is proportional to the length of the PN sequence due to spreading the spectrum, while the noise power stays the same due to the noise folding factor proportional to the length of the PN sequence.

The measured SNR degradation at the baseband output of the I1 branch driven by an m-sequence and of the I6 and I7 branches driven by two unique gold sequences compared to mixing with a square LO corresponding to that specific bin is shown in Fig. 6.15 for the 2.7-3.7GHz input frequency range. The I1 branch driven by the m-sequence demonstrates a uniform SNR degradation that corresponds closely with its spectral properties as given in (6.4) (shown in Fig. 6.15 with

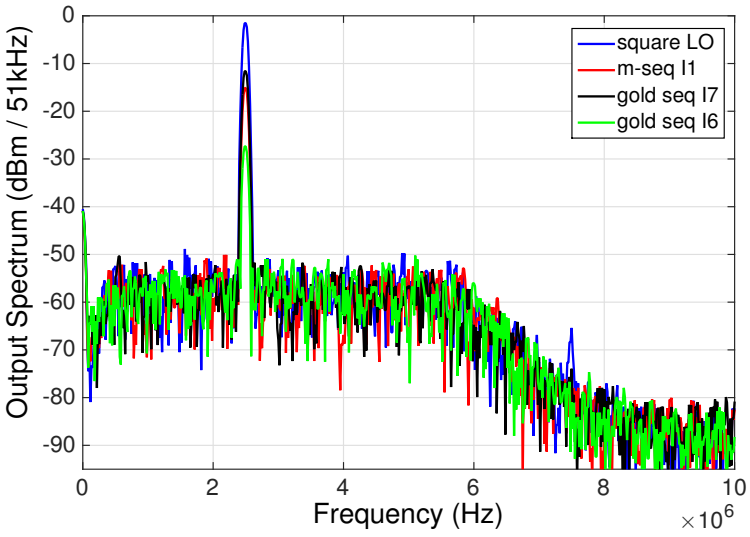

Figure 6.14: *The output SNR degradation is demonstrated with the measured output spectrum; an RF input tone at 3342.5MHz mixed with a square LO (I1 branch), an m-sequence (I1 branch) and two unique gold sequences (I6 and I7 branches) from the time-segmented PN sequence set k is observed in the baseband.*

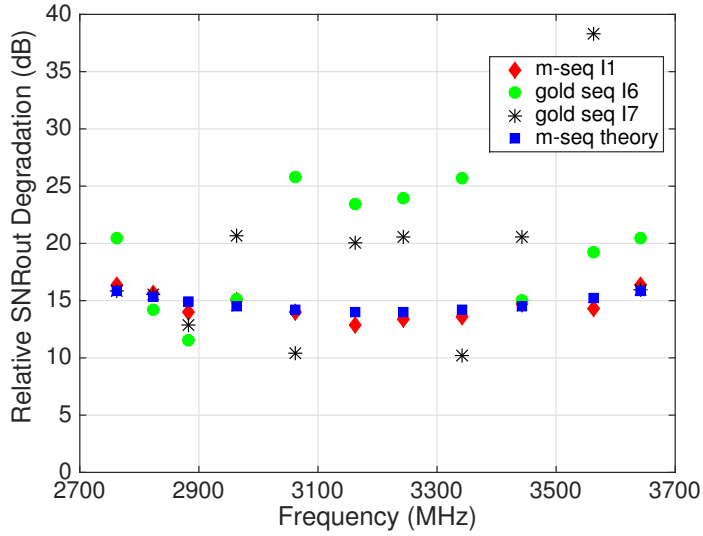

Figure 6.15: *Measured SNR degradation of the TS-QAIC with respect to mixing with a square LO for an m-sequence (I1 branch) and two unique gold sequences (I6 and I7 branches) that demonstrates the noise folding impact of PN mixing.*

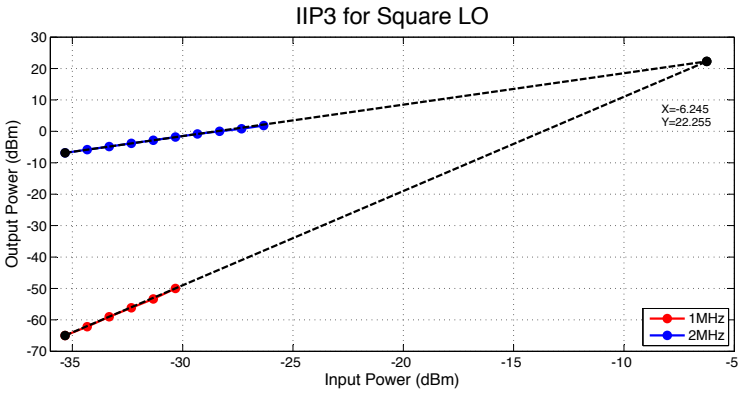

(a)

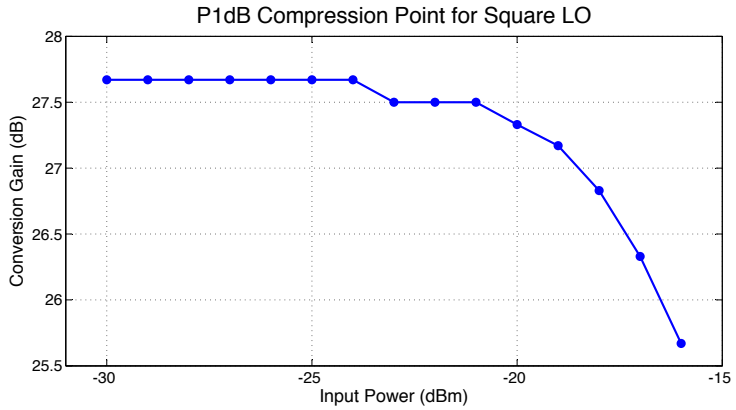

(b)

Figure 6.16: *(a) TS-QAIC I1 branch in-band IIP3 for a square LO, (b) TS-QAIC I1 branch P1dB for a square LO.*

blue square data points) compared to the I6 and I7 branches driven by two unique gold sequences due to their nonuniform spectral properties.

6.3.4 TS-QAIC Linearity Characterization with a Square LO

TS-QAIC branches are characterized in terms of the RF performance by driving the second stage mixer with a square LO as the comparative reference point in addition their characterization by driving the same mixer with a PN sequence. The measured in-band IIP3 of a TS-QAIC branch

driven by a square LO is -6.24dBm, as shown in Fig. 6.16(a) tested with two RF tones located at 3.342GHz and 3.343GHz. The measured P1dB of a TS-QAIC branch driven by a square LO is -18dBm, as shown in Fig. 6.16(b) tested with an RF tone located at 3.342GHz.

6.4 Discussion

In this chapter, the noise analysis of a PN mixer and the effect of number of samples on the sensitivity of an AIC are discussed. The TS-QAIC SNR degradation and sensitivity measurement results conform well to the predicted performance based on the analysis. Furthermore, the linearity analysis of a PN mixer with intra-bin and inter-bin spectrum test cases is discussed. As a first step towards the future directions of this research, the TS-QAIC linearity measurements for the following spectrum scenarios; intra-bin and inter-bin with adjacent and nonadjacent bin locations, will be collected and analyzed to demonstrate which building blocks of an AIC are contributing to the nonlinearities for these test cases.

Chapter 7

Conclusions

7.1 Band-pass Compressive Sampling as an Enabling Solution for Energy-Efficient and Rapid Wideband RF Spectrum Sensing in Future Cognitive Radio Systems

The 'landscape' of spectrum scanners and sensors is shown in Fig. 7.1, which classifies them based on their applications and shows where the band-pass CS interferer detectors presented in this dissertation, the QAIC and the TS-QAIC, fit into this 'landscape.' Key performance metrics for comparison are energy consumption per scan, where E is the energy consumption of a QAIC, scan time, instantaneous dynamic range, and instantaneous bandwidth. The number of detectable interferers is another key performance metric for compressed sampling detectors. The 'landscape' of Fig. 7.1 is derived from the estimated performance of state-of-the-art traditional and compressed

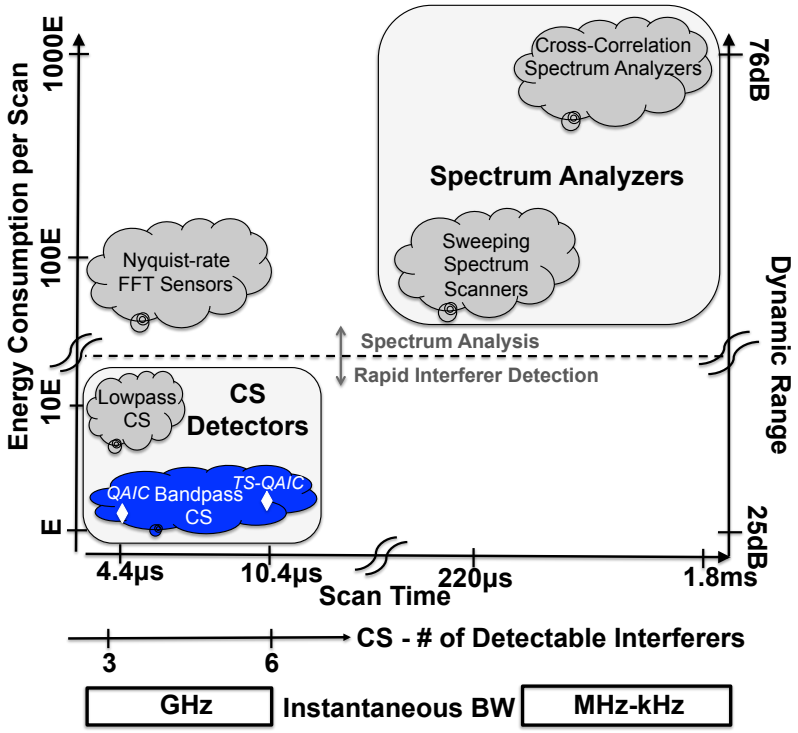

Figure 7.1: *Spectrum scanners and sensors "landscape".*

sampling based spectrum scanners and sensors that are scaled to sense a 1GHz span from 2.7 to 3.7GHz with a 20MHz RBW [3].

Traditional sweeping spectrum scanners [13, 14, 16, 18] and cross-correlation spectrum analyzers [9, 11, 12] are located at the corner where the scan time is the longest and the energy consumption is the highest. They offer a high dynamic range but at the expense of long scan time and a small instantaneous bandwidth equal to their RBW. For this example spectrum scenario, sweeping spectrum scanners require 220μs scan time with a 20MHz instantaneous bandwidth in a 1GHz span that results in high energy consumption and the risk of missing the changes in a dynamic spectrum. Cross-correlation spectrum analyzers are preferred to increase the dynamic range by improving the sensitivity at the expense of increased scan time. It is demonstrated in [9] that re-

ducing the NF by 1.5dB doubles measurement time. Both of these architectures are specialized for spectrum analyzers.

Nyquist-rate FFT spectrum sensors offer 50 times faster sensing compared to traditional sweeping spectrum scanners. However, the energy consumption stays the same to first order, as it is a power-hungry approach owing to the high Nyquist-rate ADCs (e.g. 2GSps).

Interferer detectors that offer simultaneously fast detection over a wide instantaneous bandwidth with fine frequency resolutions and low power, while requiring only modest hardware resources, are the key enabling components of future cognitive radio systems. We exploited compressive sampling in the presented works to take a 'snapshot' of the spectrum with low energy consumption and high frequency resolutions. Compressive sampling (CS), an evolutionary sensing/sampling paradigm that changes the perception of sampling, can break the traditional trade-off between span, RBW, and scan time by sampling at sub-Nyquist rates. CS detectors shown in Fig. 7.1 are specialized for rapid detection of signals in a wide instantaneous bandwidth with moderate dynamic range. Low-pass CS architectures, like [26, 28] sense the spectrum from DC to f_{max} and are more suitable for baseband applications. There is, however, a need to mix with high Nyquist-rate pseudorandom noise sequences, thereby diminishing the energy savings offered by low-pass CS especially at RF frequencies.

Band-pass CS architectures are a technology proposed to enable energy-efficient and rapid RF spectrum sensing over a wide instantaneous bandwidth in emerging cognitive radio terminals. Band-pass CS architectures offer very short scan time compared to traditional spectrum analyzers and lower power consumption for RF frequencies compared to low-pass CS architectures.

A quadrature analog-to-information converter (QAIC) [3–5] that uniquely exploits band-pass compressed sampling is presented for the rapid sensing of large spectral bandwidths with high frequency resolutions. The QAIC senses a frequency span of 1GHz ranging from 2.7 to 3.7GHz with a resolution bandwidth of 20MHz in 4.4μs, an interferer detection 50 times faster than that of traditional spectrum scanner architectures. The QAIC front end consumes 81mW from a 1.1V supply. The QAIC is estimated to be two orders of magnitude more energy efficient than traditional spectrum scanner/sensors and one order of magnitude more energy efficient than existing low-pass CS spectrum sensors. The aggregate sampling rate in the QAIC is compressed by 6.3 times compared to traditional Nyquist-rate approaches.

Increasing the number of interferers that can be detected with the QAIC requires a proportional increase in the number of physical I/Q branches. However, increasing the hardware complexity and silicon cost of the QAIC to accommodate 6 interferers would be overkill given that the QAIC can detect 3 interferers in 4.4μs and spectrum is typically stationary for 10s of μs. A time-segmented quadrature analog-to-information converter (TS-QAIC) [8] that introduces system scalability in multiple dimensions by adaptive thresholding in the information recovery engine and by virtually extending physical hardware through time segmentation is presented in order to meet different performance goals like the number of detectable interferers, energy consumption, and scan time, while limiting silicon cost and complexity. Enabling time segmentation thus allows the detection of twice the number of interferers without doubling the amount of hardware, while taking advantage of spectrum stationary for 10s of μs. The TS-QAIC rapidly detects 6 interferers in the PCAST

spectrum between 2.7 and 3.7GHz with a 10.4μs sensing time for a 20MHz RBW with only 8 physical I/Q branches, while consuming 81.2mW from a 1.2V supply.

7.2 Future Research Directions: 'What to Explore Next?'

Band-pass CS architectures enable low energy consumption and rapid spectrum sensing by breaking the fixed trade-off in scan time versus RBW of traditional sweeping spectrum scanners, but have a trade-off in instantaneous bandwidth versus instantaneous dynamic range. Some of the challenges associated with the design of compressed sampling analog-to-information converters including noise folding and the effect of spectral properties of PN sequences are discussed in Chapter 6. These challenges lead to open questions for the field. One of these might be the new type of sequences that would be optimal for capturing the wide instantaneous bandwidth, while maintaining 'good' sensing matrix properties like RIP and low mutual coherence for successful CS support recovery, and at the same time improving the instantaneous dynamic range that could be offered by analog-to-information converters (AICs).

The presented interdisciplinary research project offers novel solutions for multi-tiered, shared spectrum access terminals. One of the cross-layer questions that is a promising avenue for future interdisciplinary research directions is the co-optimization of circuits and signal processing algorithms to address circuit impairments such as nonlinearities and noise. We further note that a first step towards co-optimization of circuits and signal processing algorithms is investigating and modeling the nonlinearities of band-pass CS architectures, like the QAIC [3] and the TS-QAIC [8]. A specific example, mentioned briefly in Chapter 6, is analyzing the effect of unique spectral prop-

erties of PN sequences on the nonlinearity of a band-pass CS QAIC or TS-QAIC and integrating the model of the nonlinearities derived from the contributions of AIC building blocks into the CS support recovery problem.

Compressive sampling is an emerging research area that has been exploited in variety of interdisciplinary research fields like neuroscience [68, 69], machine learning [70], astronomy [71, 72], optics [73, 74], sensing [3, 21, 26, 28, 42], communications [75, 76], and also extensively in medical imaging [77–79]. The research work presented here is only one example of how to leverage new evolutions in sampling for RF spectrum sensing. Using compressive sampling in novel interferer detector architectures like the band-pass CS QAIC [3] and TS-QAIC [8] thus enables energy-efficient and rapid sensing over a wide span.

Bibliography

[1] J. Mitola, "Cognitive radio for flexible mobile multimedia communications," in *IEEE International Workshop on Mobile Multimedia Communications*, 1999, pp. 3–10.

[2] A. Ghaffari, E. A. M. Klumperink, and B. Nauta, "Tunable N-path notch filters for blocker suppression: Modeling and verification," *IEEE J. Solid-State Circuits*, vol. 48, no. 6, pp. 1370–1382, June 2013.

[3] R. T. Yazicigil, T. Haque, M. R. Whalen, J. Yuan, J. Wright, and P. Kinget, "Wideband rapid interferer detector exploiting compressed sampling with a quadrature analog-to-information converter," *IEEE J. Solid-State Circuits*, vol. 50, no. 12, pp. 3047–3064, Dec. 2015.

[4] T. Haque, R. T. Yazicigil, K. J.-L. Pan, J. Wright, and P. R. Kinget, "Theory and design of a quadrature analog-to-information converter for energy-efficient wideband spectrum sensing," *IEEE Transactions on Circuits and Systems I*, vol. 62, no. 2, pp. 527–535, Feb. 2015.

[5] R. T. Yazicigil, T. Haque, M. R. Whalen, J. Yuan, J. Wright, and P. R. Kinget, "19.4 A 2.7-to-3.7GHz rapid interferer detector exploiting compressed sampling with a quadrature analog-to-information converter," in *IEEE International Solid-State Circuits Conference*, Feb. 2015, pp. 1–3.

[6] D. L. Donoho, "Compressed sensing," *IEEE Transactions on Information Theory*, vol. 52, no. 4, pp. 1289–1306, April 2006.

[7] E. J. Candés, J. Romberg, and T. Tao, "Robust uncertainty principles: Signal reconstruction from highly incomplete frequency information," *IEEE Transactions on Information Theory*, vol. 52, no. 2, pp. 489–509, Feb. 2006.

[8] R. T. Yazicigil, T. Haque, M. Kumar, J. Yuan, J. Wright, and P. Kinget, "A compressed-sampling time-segmented quadrature analog-to-information converter for wideband rapid detection of up to 6 interferers with adaptive thresholding," in *IEEE Radio Frequency Integrated Circuits Symposium (accepted for presentation)*, May 2016.

[9] M. S. Oude Alink, E. A. M. Klumperink, M. C. M. Soer, A. B. J. Kokkeler, and B. Nauta, "A 50Mhz-to-1.5Ghz cross-correlation CMOS spectrum analyzer for cognitive radio with 89dB SFDR in 1Mhz RBW," in *IEEE Symposium on New Frontiers in Dynamic Spectrum*, April 2010, pp. 1–6.

[10] M. S. Oude Alink, E. A. M. Klumperink, A. B. J. Kokkeler, M. C. M. Soer, G. J. M. Smit, and B. Nauta, "A CMOS-compatible spectrum analyzer for cognitive radio exploiting cross-correlation to improve linearity and noise performance," *IEEE Transactions on Circuits and Systems I*, vol. 59, no. 3, pp. 479–492, March 2012.

[11] M. S. Oude Alink, E. A. M. Klumperink, A. B. J. Kokkeler, Z. Ru, W. Cheng, and B. Nauta, "Using crosscorrelation to mitigate analog/RF impairments for integrated spectrum analyzers," *IEEE Transactions on Microwave Theory and Techniques*, vol. 61, no. 3, pp. 1327–1337, March 2013.

[12] M. S. Oude Alink, A. B. J. Kokkeler, E. A. M. Klumperink, G. J. M. Smit, and B. Nauta, "Spectrum sensing with high sensitivity and interferer robustness using cross-correlation energy detection," *IEEE J. Emerging and Selected Topics in Circuits and Systems*, vol. 3, no. 4, pp. 566–575, Dec. 2013.

[13] A. Goel, B. Analui, and H. Hashemi, "A 130-nm CMOS 100-Hz–6-GHz reconfigurable vector signal analyzer and software-defined receiver," *IEEE Transactions on Microwave Theory and Techniques*, vol. 60, no. 5, pp. 1375–1389, May 2012.

[14] J. Park, T. Song, J. Hur, S. M. Lee, J. Choi, K. Kim, K. Lim, C. H. Lee, H. Kim, and J. Laskar, "A fully integrated UHF-band CMOS receiver with multi-resolution spectrum sensing (MRSS) functionality for IEEE 802.22 cognitive radio applications," *IEEE J. Solid-State Circuits*, vol. 44, no. 1, pp. 258–268, Jan. 2009.

[15] M. Kitsunezuka, H. Kodama, N. Oshima, K. Kunihiro, T. Maeda, and M. Fukaishi, "A 30-MHz-2.4-GHz CMOS receiver with integrated RF filter and dynamic-range-scalable energy detector for cognitive radio systems," *IEEE J. Solid-State Circuits*, vol. 47, no. 5, pp. 1084–1093, May 2012.

[16] M. Kitsunezuka and K. Kunihiro, "A 5-9-mw, 0.2-2.5-GHz CMOS low-IF receiver for spectrum-sensing cognitive radio sensor networks," in *IEEE Radio Frequency Integrated Circuits Symposium*, June 2013, pp. 319–322.

[17] "Spectrum analysis basics," *Agilent Technologies Application Note 150*.

[18] S. Pollin, E. Lopez, A. Antoun, P. Van Wesemael, L. Hollevoet, A. Bourdoux, A. Dejonghe, and L. Van der Perre, "Digital and analog solution for low-power multi-band sensing," in *IEEE Symposium on New Frontiers in Dynamic Spectrum*, April 2010, pp. 1–2.

[19] B. Murmann, "ADC performance survey 1997-2015, available: http://web.stanford.edu/ murmann/adcsurvey.html."

[20] S. Kirolos, J. Laska, M. Wakin, M. Duarte, D. Baron, T. Ragheb, Y. Massoud, and R. Baraniuk, "Analog-to-information conversion via random demodulation," in *IEEE Dallas/CAS Workshop on Design, Applications, Integration and Software*, Oct. 2006, pp. 71–74.

[21] J. N. Laska, S. Kirolos, M. F. Duarte, T. S. Ragheb, R. G. Baraniuk, and Y. Massoud, "Theory and implementation of an analog-to-information converter using random demodulation," in *IEEE International Symposium on Circuits and Systems*, May 2007, pp. 1959–1962.

[22] Z. Tian and G. B. Giannakis, "Compressed sensing for wideband cognitive radios," in *International Conference on Acoustics, Speech, and Signal Processing*, vol. 4, April 2007, pp. IV–1357–IV–1360.

[23] M. Mishali and Y. C. Eldar, "Blind multiband signal reconstruction: Compressed sensing for analog signals," *IEEE Transactions on Signal Processing*, vol. 57, no. 3, pp. 993–1009, March 2009.

[24] J. Yoo, S. Becker, M. Monge, M. Loh, E. Candès, and A. Emami-Neyestanak, "Design and implementation of a fully integrated compressed-sensing signal acquisition system," in *IEEE International Conference on Acoustics, Speech and Signal Processing*, March 2012, pp. 5325–5328.

[25] J. Yoo, C. Turnes, E. Nakamura, C. Le, S. Becker, E. Sovero, M. Wakin, M. Grant, J. Romberg, A. Emami-Neyestanak, and E. Candès, "A compressed sensing parameter extraction platform for radar pulse signal acquisition," *IEEE J. Emerging and Selected Topics in Circuits and Systems*, vol. 2, no. 3, pp. 626–638, Sept. 2012.

[26] J. Yoo, S. Becker, M. Loh, M. Monge, E. Candès, and A. Emami-Neyestanak, "A 100MHz–2GHz 12.5x sub-Nyquist rate receiver in 90nm CMOS," in *IEEE Radio Frequency Integrated Circuits Symposium*, June 2012, pp. 31–34.

[27] M. Wakin, S. Becker, E. Nakamura, M. Grant, E. Sovero, D. Ching, J. Yoo, J. Romberg, A. Emami-Neyestanak, and E. Candès, "A nonuniform sampler for wideband spectrally-sparse environments," *IEEE J. Emerging and Selected Topics in Circuits and Systems*, vol. 2, no. 3, pp. 516–529, Sept. 2012.

[28] X. Chen, E. A. Sobhy, Z. Yu, S. Hoyos, J. Silva-Martinez, S. Palermo, and B. M. Sadler, "A sub-Nyquist rate compressive sensing data acquisition front-end," *IEEE J. Emerging and Selected Topics in Circuits and Systems*, vol. 2, no. 3, pp. 542–551, Sept. 2012.

[29] Z. Yu, S. Hoyos, and B. M. Sadler, "Mixed-signal parallel compressed sensing and reception for cognitive radio," in *IEEE International Conference on Acoustics, Speech and Signal Processing*, March 2008, pp. 3861–3864.

[30] Y. Wang, Z. Tian, and C. Feng, "A two-step compressed spectrum sensing scheme for wideband cognitive radios," in *IEEE Global Telecommunications Conference*, Dec. 2010, pp. 1–5.

[31] J. Selva, "Regularized sampling of multiband signals," *IEEE Transactions on Signal Processing*, vol. 58, no. 11, pp. 5624–5638, Nov. 2010.

[32] M. Fleyer, A. Linden, M. Horowitz, and A. Rosenthal, "Multirate synchronous sampling of sparse multiband signals," *IEEE Transactions on Signal Processing*, vol. 58, no. 3, pp. 1144–1156, March 2010.

[33] M. E. Domínguez-Jiménez and N. González-Prelcic, "Analysis and design of multirate synchronous sampling schemes for sparse multiband signals," in *Proceedings of the 20th European Signal Processing Conference*, Aug. 2012, pp. 1184–1188.

[34] O. Viitala, M. Kaltiokallio, M. Kosunen, K. Stadius, and J. Ryynanen, "A wideband undersampling blocker detector with a 0.7-2.7 GHz mixer-first receiver," in *IEEE Radio Frequency Integrated Circuits Symposium*, May 2015, pp. 335–338.

[35] C. E. Shannon, "Communication in the presence of noise," *Proceedings of the IRE*, vol. 37, no. 1, pp. 10–21, Jan. 1949.

[36] E. J. Candès and T. Tao, "Decoding by linear programming," *IEEE Transactions on Information Theory*, vol. 51, no. 12, pp. 4203–4215, Dec. 2005.

[37] D. L. Donoho, "For most large underdetermined systems of equations, the minimal ℓ^1 norm near solution approximates the sparsest solution," *Communications on Pure and Applied Mathematics*, vol. 59, no. 7, pp. 907–934, 2006.

[38] J. A. Tropp, J. N. Laska, M. F. Duarte, J. K. Romberg, and R. G. Baraniuk, "Beyond nyquist: Efficient sampling of sparse bandlimited signals," *IEEE Transactions on Information Theory*, vol. 56, no. 1, pp. 520–544, Jan. 2010.

[39] E. J. Candès and T. Tao, "Near-optimal signal recovery from random projections: Universal encoding strategies?" *IEEE Transactions on Information Theory,*, vol. 52, no. 12, pp. 5406–5425, Dec. 2006.

[40] M. F. Duarte, M. A. Davenport, D. Takhar, J. N. Laska, T. Sun, K. F. Kelly, and R. G. Baraniuk, "Single-pixel imaging via compressive sampling," *IEEE Signal Processing Magazine*, vol. 25, no. 2, pp. 83–91, March 2008.

[41] M. B. Wakin, J. N. Laska, M. F. Duarte, D. Baron, S. Sarvotham, D. Takhar, K. F. Kelly, and R. G. Baraniuk, "An architecture for compressive imaging," in *IEEE International Conference on Image Processing*, Oct. 2006, pp. 1273–1276.

[42] M. Mishali and Y. C. Eldar, "From theory to practice: Sub-Nyquist sampling of sparse wideband analog signals," *IEEE J. Selected Topics in Signal Processing*, vol. 4, no. 2, pp. 375–391, April 2010.

[43] M. Mishali and Y. C. Eldar, "Wideband spectrum sensing at sub-Nyquist rates [applications corner]," *IEEE Signal Processing Magazine*, vol. 28, no. 4, pp. 102–135, July 2011.

[44] M. F. Duarte, M. A. Davenport, M. B. Wakin, and R. G. Baraniuk, "Sparse signal detection from incoherent projections," in *IEEE International Conference on Acoustics, Speech and Signal Processing*, vol. 3, May 2006, pp. III–III.

[45] M. A. Davenport, P. T. Boufounos, M. B. Wakin, and R. G. Baraniuk, "Signal processing with compressive measurements," *IEEE J. Selected Topics in Signal Processing*, vol. 4, no. 2, pp. 445–460, April 2010.

[46] J. Haupt and R. Nowak, "Compressive sampling for signal detection," in *IEEE International Conference on Acoustics, Speech and Signal Processing*, vol. 3, April 2007, pp. III–1509–III–1512.

[47] R. Pickholtz, D. Schilling, and L. Milstein, "Theory of spread-spectrum communications–A tutorial," *IEEE Transactions on Communications*, vol. 30, no. 5, pp. 855–884, May 1982.

[48] B. Razavi, "Design considerations for direct-conversion receivers," *IEEE Transactions on Circuits and Systems II*, vol. 44, no. 6, pp. 428–435, June 1997.

[49] L. Anttila, M. Valkama, and M. Renfors, "Circularity-based I/Q imbalance compensation in wideband direct-conversion receivers," *IEEE Transactions on Vehicular Technology*, vol. 57, no. 4, pp. 2099–2113, July 2008.

[50] F. Bruccoleri, E. A. M. Klumperink, and B. Nauta, "Wide-band CMOS low-noise amplifier exploiting thermal noise canceling," *IEEE J. Solid-State Circuits*, vol. 39, no. 2, pp. 275–282, Feb. 2004.

[51] S. C. Blaakmeer, E. A. M. Klumperink, D. M. W. Leenaerts, and B. Nauta, "Wideband balun-LNA with simultaneous output balancing, noise-canceling and distortion-canceling," *IEEE J. Solid-State Circuits*, vol. 43, no. 6, pp. 1341–1350, June 2008.

[52] A. Mirzaei, H. Darabi, J. C. Leete, X. Chen, K. Juan, and A. Yazdi, "Analysis and optimization of current-driven passive mixers in narrowband direct-conversion receivers," *IEEE J. Solid-State Circuits*, vol. 44, no. 10, pp. 2678–2688, Oct. 2009.

[53] R. Bagheri, A. Mirzaei, S. Chehrazi, M. E. Heidari, M. Lee, M. Mikhemar, W. Tang, and A. A. Abidi, "An 800-MHz-6-GHz software-defined wireless receiver in 90-nm CMOS," *IEEE J. Solid-State Circuits*, vol. 41, no. 12, pp. 2860–2876, Dec. 2006.

[54] B. Razavi, *RF Microelectronics*. Prentice Hall, 1998.

[55] B. Razavi, *Design of Analog CMOS Integrated Circuits*. Mc-Graw Hill, 2001.

[56] R. Gold, "Optimal binary sequences for spread spectrum multiplexing (corresp.)," *IEEE Transactions on Information Theory*, vol. 13, no. 4, pp. 619–621, Oct. 1967.

[57] J. K. Holmes, *Spread Spectrum Systems for GNSS and Wireless Communications*. Artech House, 2007.

[58] J. A. Tropp and A. C. Gilbert, "Signal recovery from random measurements via orthogonal matching pursuit," *IEEE Transactions on Information Theory*, vol. 53, no. 12, pp. 4655–4666, Dec. 2007.

[59] T. Zhang, "Sparse recovery with orthogonal matching pursuit under RIP," *IEEE Transactions on Information Theory*, vol. 57, no. 9, pp. 6215–6221, Sept. 2011.

[60] S. Goel, A. Kumar, and M. Bayoumi, "Design of robust, energy-efficient full adders for deep-submicrometer design using Hybrid-CMOS logic style," *IEEE Transactions on Very Large Scale Integration Systems*, vol. 14, no. 12, pp. 1309–1321, Dec. 2006.

[61] N. Rajput, M. Sethi, P. Dobriyal, K. Sharma, and G. Sharma, "A novel, high performance and power efficient implementation of 8x8 multiplier unit using MT-CMOS technique," in *Sixth International Conference on Contemporary Computing*, Aug 2013, pp. 186–191.

[62] M. C. M. Soer, E. A. M. Klumperink, Z. Ru, F. E. van Vliet, and B. Nauta, "A 0.2-to-2.0GHz 65nm CMOS receiver without LNA achieving $\gg$11dBm IIP3 and $\ll$6.5 dB NF," in *IEEE International Solid-State Circuits Conference*, Feb. 2009, pp. 222–223,223a.

[63] M. Ingels, V. Giannini, J. Borremans, G. Mandal, B. Debaillie, P. van Wesemael, T. Sano, T. Yamamoto, D. Hauspie, J. Van Driessche, and J. Craninckx, "A 5mm^2 40nm LP CMOS 0.1-to-3GHz multistandard transceiver," in *IEEE International Solid-State Circuits Conference*, Feb. 2010, pp. 458–459.

[64] C.-W. Hsu, K. Tripurari, S.-A. Yu, and P. R. Kinget, "A sub-sampling-assisted phase-frequency detector for low-noise PLLs with robust operation under supply interference," *IEEE Transactions on Circuits and Systems I*, vol. 62, no. 1, pp. 90–99, Jan. 2015.

[65] S.-A. Yu and P. Kinget, "A 0.042-mm^2 fully integrated analog PLL with stacked capacitor-inductor in 45nm CMOS," in *34th European Solid-State Circuits Conference*, Sept. 2008, pp. 94–97.

[66] J. Zhu, H. Krishnaswamy, and P. R. Kinget, "Field-programmable LNAs with interferer-reflecting loop for input linearity enhancement," *IEEE J. Solid-State Circuits*, vol. 50, no. 2, pp. 556–572, Feb. 2015.

[67] M. A. Davenport, J. N. Laska, J. R. Treichler, and R. G. Baraniuk, "The pros and cons of compressive sensing for wideband signal acquisition: Noise folding versus dynamic range," *IEEE Transactions on Signal Processing*, vol. 60, no. 9, pp. 4628–4642, Sept. 2012.

[68] Y. Mishchenko and L. Paninski, "A bayesian compressed-sensing approach for reconstructing neural connectivity from subsampled anatomical data," *Journal of Computational Neuroscience*, vol. 33, no. 2, pp. 371–388, Oct. 2012.

[69] T. Hu and D. B. Chklovskii, "Reconstruction of sparse circuits using multi-neuronal excitation (RESCUME)," in *Advances in Neural Information Processing Systems 22*, 2009, pp. 790–798.

[70] J. Wright, A. Y. Yang, A. Ganesh, S. S. Sastry, and Y. Ma, "Robust face recognition via sparse representation," *IEEE Transactions on Pattern Analysis and Machine Intelligence*, vol. 31, no. 2, pp. 210–227, Feb. 2009.

[71] J. McEwen and Y. Wiaux, "Compressed sensing for radio interferometric imaging: Review and future direction," in *18th IEEE International Conference on Image Processing*, Sept. 2011, pp. 1313–1316.

[72] J. Bobin, J.-L. Starck, and R. Ottensamer, "Compressed sensing in astronomy," *IEEE J. Selected Topics in Signal Processing*, vol. 2, no. 5, pp. 718–726, Oct. 2008.

[73] Y. Shechtman, S. Gazit, A. Szameit, E. C. Yonina, and M. Segev, "Super-resolution and reconstruction of sparse images carried by incoherent light," *Optics Letters*, vol. 35, no. 8, pp. 1148–1150, 2010.

[74] D. J. Brady, K. Choi, D. L. Marks, R. Horisaki, and S. Lim, "Compressive holography," *Optics Express*, vol. 17, no. 15, pp. 13 040–13 049, 2009.

[75] W. U. Bajwa, J. Haupt, A. M. Sayeed, and R. Nowak, "Compressed channel sensing: A new approach to estimating sparse multipath channels," *Proceedings of the IEEE*, vol. 98, no. 6, pp. 1058–1076, June 2010.

[76] C. R. Berger, Z. Wang, J. Huang, and S. Zhou, "Application of compressive sensing to sparse channel estimation," *IEEE Communications Magazine*, vol. 48, no. 11, pp. 164–174, Nov. 2010.

[77] M. Lustig, D. Donoho, and J. M. Pauly, "Sparse MRI: The application of compressed sensing for rapid MR imaging," *Magnetic Resonance in Medicine*, vol. 58, no. 6, pp. 1182–1195, Dec. 2007.

[78] U. Gamper, P. Boesiger, and S. Kozerke, "Compressed sensing in dynamic MRI," *Magnetic Resonance in Medicine*, vol. 59, no. 2, pp. 365–373, Feb. 2008.

[79] H. Jung, K. Sung, K. S. Nayak, E. Y. Kim, and J. C. Ye, "k-t FOCUSS: a general compressed sensing framework for high resolution dynamic MRI," *Magnetic Resonance in Medicine*, vol. 61, no. 1, pp. 103–116, Jan. 2009.